POROUS SILICON OPTICAL BIOSENSORS TOWARDS POINT-OF-CARE APPLICATIONS

By

Tengfei Cao

Dissertation

Submitted to the Faculty of the

Graduate School of Vanderbilt University

in partial fulfillment of the requirements

for the degree of

DOCTOR OF PHILOSOPHY

in

Interdisciplinary Materials Science

May 31, 2021

Nashville, Tennessee

Approved:

Prof. Sharon M. Weiss, Ph.D.

Prof. Paul E. Laibinis, Ph.D.

Prof. Yaqiong Xu, Ph.D.

Prof. Craig L. Duvall, Ph.D.

Prof. Catherine Chang, Ph.D.

To my beloved family and wonderful friends,

ACKNOWLEDGMENTS

First and foremost, I would like to express my gratitude to Prof. Sharon Weiss, for her excellent guidance and mentoring. I am deeply thankful to her for letting me join her research group and instilling confidence in me. Her guidance, patience and encouragement has been helping me to overcome most of the challenges encountered during my Ph.D. study.

I would like to acknowledge my Ph.D. committee, whose advice and critiques have been extremely helpful in discovering brilliant ideas. I am especially grateful to Prof. Paul Laibinis who provided significant guidance to my research work. I would like to thank Prof. Catie Chang for her kindly help and valuable advices on machine learning project. I would like to thank Prof. Craig L. Duvall for his suggestions on the possible application of machine learning assisted biosensing system. I am thankful to Prof. Yaqiong Xu for her support and valuable suggestions on smartphone biosensor and other projects.

I am truly honored to have been a part of the Weiss group. I would like to thank all the past and present members of the Weiss group for maintaining an innovative research atmosphere in FGH 331/335 and a dynamic work environment in FGH 323. Thanks to Dr. Yiliang Zhao for introducing me to porous silicon research and teaching me the numerous tools and techniques fundamentals for my work. Thanks to Rabeb Layouni and Simon Ward for great work in our collaboration. Thanks for Dr. Gilbert Rodriguez, Dr. Josh Fain, Dr. Kelsey Mayo, Dr. Jeremy Mares, Kun Qin for the help on porous silicon research. Thanks for Dr. Kevin Miller, Sami Halimi, Dr. Francis Afzal, Dr. Zhongyuan Fu, Landen Ryder, Dr. Shuren Hu, Josh Allen and Kellen Arnold for the help on the optics and beyond. Thanks to Crystal Natto and all the undergraduate researchers who made contributions to this research.

I would like to thank my wonderful collaborators outside the Weiss group. First, I would like acknowledge significant help from Bradley Baker. His hard work and dedication to chemistry made the peptide project possible. I would like to thank Matthew B. Coppock for the help on the peptide project and providing us with all the materials necessary for the experiment. I would like to thank Zhaobo Zheng and Harison Yan for the help with 3D printing. I would like to thank Dr. Vijay Koju for the help of aperiodic photonic structures, Dr. Tengyu Ma for helpful discussion on Machine learning and deep learning. I would like to thank Tianjiao Wang, Yuchen zhang for the help with the measurements, You Zhou, Chuchuan Hong, Sen Yang, Yuxi Jiang, Mingze He, Zhiliang Pan for useful technical discussions.

I would like to thank all the staff at the Vanderbilt Institute for Nanoscale Science and Engineering (VINSE) for teaching me the instruments and techniques related to fabrication and analysis.

Finally, I would like to thank my family to whom I am grateful for their encouragement

and support.

The research presented in this thesis was funded in part by the Army Research Office (W911NF-15-1-0176).

TABLE OF CONTENTS

LIST OF TABLES

LIST OF FIGURES

CHAPTER 1

Introduction

1.1 Optical Biosensors

Biosensors are devices used to detect the presence or concentration of a biological analyte, or to monitor continuous biochemical reactions. A biosensor combines a biorecognition element with a physicochemical transducer, sometimes a data analyzer and a reader. Biosensors, along with the bioassays and biochemical assays, provide the information crucial to medical diagnostics, infectious disease screening, food safety inspection, security checks and environmental monitoring, and play an increasingly important role in the modern society. The overall biosensors market is projected to grow from 21.2 billion USD in 2019 to 31.5 billion by 2024 at a compound annual growth rate of 8.3%.[1]

Based on the signal transduction methods, biosensors can be categorized as optical, electrical, electrochemical, thermometric, piezoelectric, magnetic and micromechanical.[2] Optical biosensors represent one of the most common type of biosensors and promise to be the most widely used biosensor in the future. Compared to other sensing technologies, optical sensing is more direct, non-invasive, and very robust against environmental interference.

Optical sensing is performed by monitoring the interaction of light with the analyte and biorecognition element. Based on whether or not labels are used, optical sensing could be further classified into label-based and label-free sensing. Common label-based sensing protocols include (1) colorimetric labeling, (2) fluorescent labeling, (3) chemiluminescent labeling, and (4) nanoparticle labeling.[3] Labeling helps biosensors transform a non-directly readable signal into a directly observable signal and signal magnification is

also commonly associated with the transformation. Label-based sensing could detect trace amounts of analyte with the help of highly sensitive photon detectors. The systems can have high signal to noise ratios even with inexpensive instrumentation. One of the classic examples of label-based sensing protocols is Enzyme Linked Immunosorbent Assay (ELISA), a plate-based assay technique which is widely used by hospitals and biomedical industries and is designed for detecting and quantifying biomolecular species such as peptides, proteins, antibodies, and hormones [4]. In ELISAs, antigens are immobilized to a solid support, and then a combination of target antibodies and enzymes are introduced to the system.In this mixture, target antibodies bind with the enzymes and both retain their individual functionalities. After the specific binding of the labeled antibodies with the immobilized antigens and the removal of unbound antibody-enzyme pairs, the remaining bound antibody-enzyme pairs are detected by the formation of a colored compound generated by an enzyme catalyzed reaction.[5] The enzymes used for the assay are referred to as enzyme probes. Horseradish peroxidase (HRP) and alkaline phosphatase (AP) are the most common enzyme probes in ELISAs. There are several formats used for ELISAs, and they can be classified into four categories, shown in Figure 1.1, which include direct ELISA, indirect ELISA, sandwich ELISA and competitive ELISA. Detailed procedures and working principles of ELISAs can be found in ref [6].

Though widely used in test centers, label-based biosensing suffers major limitations. Firstly, the preparation steps, including labeling, rinsing and washing, are time-consuming and low-yield; they may take hours or even days based on specific tests. Secondly, labeling introduces non-native signals which interfere with the antibody- antigen or other protein interactions. Thirdly, it is generally unsuitable for in-situ observation given the need to introduce enzymes and substrate into the testing system. Instead of relying on labels for signal transduction, label-free sensing utilizes molecular biophysical properties, such as refractive index, to monitor molecular presence or activity. The elimination of the labeling process significantly eases the burden of sample preparation and reduces the signal

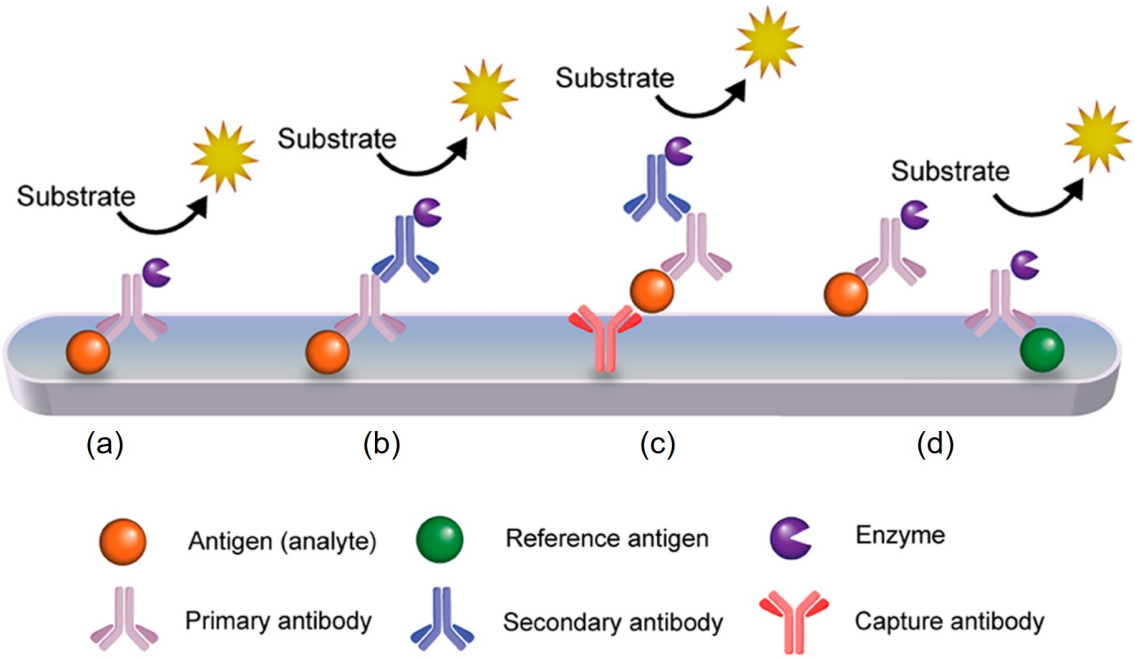

Figure 1.1: Overview of four basic ELISA methods: (a) direct ELISA, (b) indirect ELISA, (c) sandwiched ELISA and (d) competitive ELISA. Adapted with permission from Ref [7], Copyright (2020) American Chemical Society.

interference. Label-free methods feature short testing times, easy or no preparation, direct information regarding the bioanalyte, and have been used to track molecular events in real-time.

Among label-free sensing methods, surface plasmon resonance (SPR) is one of the most widely used. Since the first application of SPR phenomenon for sensing in the 1980s, this method has made great strides both in terms of instrumentation development and applications. The first commercial SPR-based biosensor instrument was launched by Pharmacia Biosensor AB, which was later renamed Biacore. Nowadays, multiple manufacturers make their own SPR instruments, and the SPR systems have become a central tool for characterizing and quantifying biomolecular interactions.[2, 8]

SPR sensors work by monitoring properties of a surface plasmon resonance when the

sensor is exposed to target molecules. A surface plasmon resonance is a charge-density oscillation that exists at the interface of two media with dielectric constants (ε) of opposite signs, for instance, a metal ($\varepsilon < 0$) and a dielectric ($\varepsilon > 0$), as shown in Figure 1.2a. The charge density wave is associated with an electromagnetic wave, the electric field of which reaches its maxima at the interface and decays evanescently into both media. The SPR is commonly excited by TM polarized light in an attenuated total reflection (ATR) configuration with the help of prism couplers in the Kretschmann geometry. When the propagation constant of the evanescent field matches that of the surface plasmon wave (Eq 1.1), the energy of the light will be coupled into the SPR mode.

$$\frac{2\pi}{\lambda}\ n_p\ sin(\theta)\ =\ \beta_{sp} \qquad \text{(Eq 1.1)}$$

where λ is the incident wavelength, n_p is the prism refractive index, θ is the incident angle and β_{sp} is the propagation constant of the surface plasmon wave. When target molecules bind to the SPR sensor, the propagation constant of the surface plasmon wave changes.

As Eq 1.1 shows, both incident wavelength and incident angle can be tuned to match the resonance condition, and the most commonly used SPR set-up is the one that measures angles, known as angular SPR.[10] A schematic illustration of the typical angular SPR sensor is shown in Figure 1.2 b, and typical spectra of the angular SPR are plotted in Figure 1.2 c.

Owing to the resonant photon-surface plasmon polariton coupling condition (Eq 1.1) and the multimode nature of the surface plasmon polariton excitation[11], SPR sensors provide a low detection limit (DL), generally lower than 10^{-5} refractive index unit (RIU) or down to nanomole per litre concentration (nM), which can be further reduced by measuring the phase shift of the SPR with a more sophisticated configuration.[12] However, SPR sensors suffer from low sensitivity for small molecules (<500Da) and do not satisfy

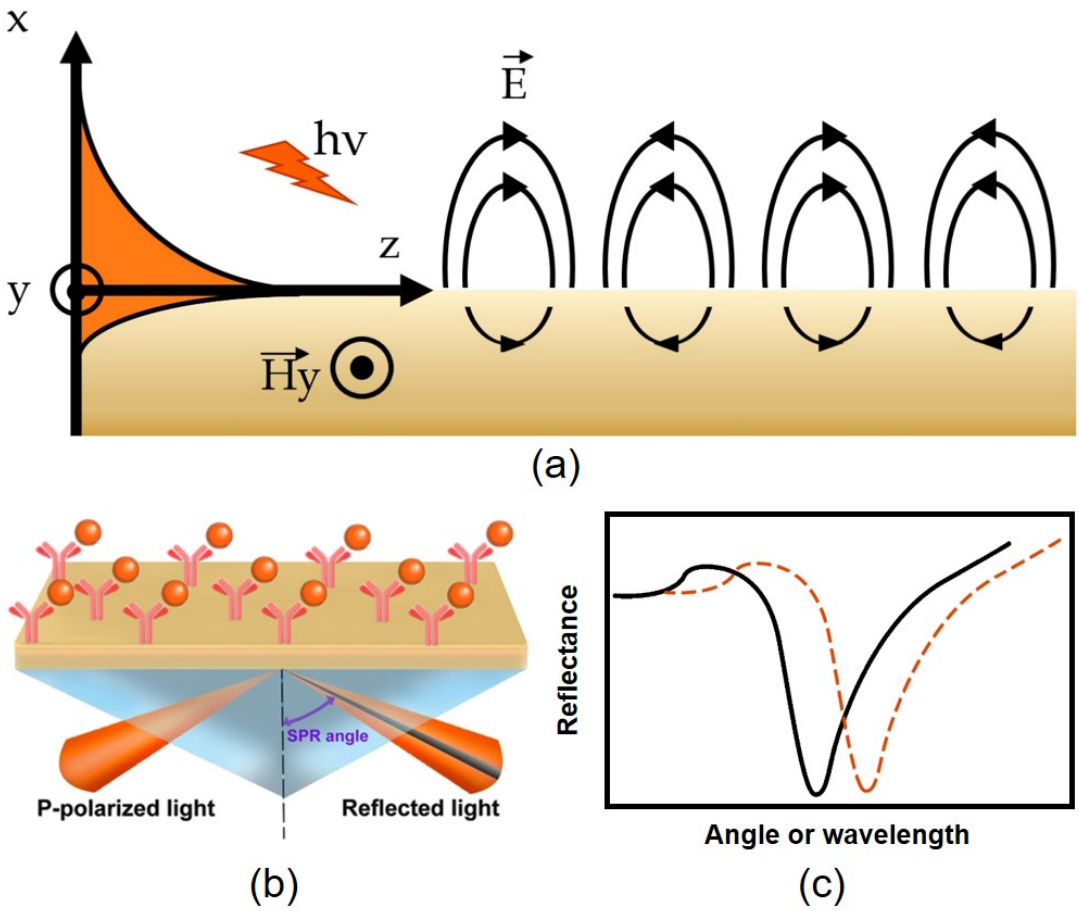

Figure 1.2: The illustration of surface plasmon resonance working principle. (a) Light coupled into surface plasmon wave. (b) The Kretschmann geometry for coupling light into SPR sensor. (c) The reflectance spectra of an angular SPR sensor before (black) and after (orange) target molecule capture. Figure (b) is adapted from Ref [9] under a Creative Commons Attribution 4.0 International License, Copyright 2016 Qingling Ouyang et al.

the current trends of biotechnology moving towards small sizes, striving for the manipulation on the nanoscale level, size-based selectivity and selective chemical and biochemical nano-architectures. [13, 14] Moreover, SPR instruments are generally expensive, requiring trained personnel and stable laboratory conditions, which limit the environments where SPR sensors can be deployed.

To achieve high sensitivity, fast testing speed and accurate results, while maintaining relatively low cost, nanomaterial based optical biosensors are recently drawing increased

attention. Nanomaterials have the intrinsic advantage of large specific surface area and great tunability in physical and chemical properties. These features could be utilized to enhance the analyte-sensor interaction, aid signal transduction and filter out interference from the environment. In order of increasing dimension, these materials include nanoparticles, nanowires and thin films. Gold nanoparticles (GNP) are one of the most important 0D nanomaterials for biosensing. Depending on their size, shape, degree of aggregation and nature of the protecting organic shells on their surface, GNPs support localized surface plasmon resonances throughout the visible and near-infrared regions, which give rise to distinct absorption and scattering profiles. Because of this unique optical property, AuNPs have been extensively explored as sensing probes for a wide range of analytes/targets, such as heavy metallic cations, nucleic acids and proteins.[15] For 1D nanomaterials, a significant number of studies have used nanowires, for example silicon or metal oxide nanowires, as field effect transistors for sensing. [16–18]. There are also examples of nanowires being used as waveguides or resonators, which show enhanced performance.[13, 19, 20] However, most of the nanowires are used for electronic based biosensors, not in the scope of optical biosensors. Similarly, many applications of two-dimensional material-based sensors, including graphene and MoS2, are employed for electrical or electrochemical sensing.[21] In the thin film realm, porous nanomaterials have shown great promise for optical sensing applications. Among porous nanomaterials, porous silicon (PSi) thin films have been studied extensively for biosensing.[22] PSi advantages include: extremely high internal surface area (> 500 m^2g^{-1}), offering a tremendous number of binding sites for hosting biological molecules and interactions; unique and tunable photonic properties, allowing for sensitive and reliable signal transduction; well-established surface chemistries; and relatively simple and cost-effective fabrication. These make PSi a superior alternative to other planar photonic biosensors for many applications. Various PSi structures have been demonstrated for biosensing, including PSi interferometers, double layers, Bragg stacks, microcavites, rugate filters, waveguides and ring resonators. The detection limits for PSi biosensors are

typically in the nM to μM range, although lower detection limits have been reported in a few cases.[23, 24]

1.2 Point of care biosensing

In the early days of diagnosis , doctors diagnosed patients based on observation and experience, as very few test assays were available, and even those were of prohibitively high cost at the time. With the emergence of automated technology and large hospitals, centralized clinical test labs started to run large quantity of tests at low unit cost.[25] However, sending samples to central labs to test might take days or weeks to get results, which may delay treatment or even lead to the spread of infections.

Over the past few decades, medical testing has seen significant changes. Not only has the centralized lab of a hospital developed the capability to deliver the results faster and with greater accuracy than ever before, but a new kind of test has emerged, which could be performed in a wide variety of locations: in your home, in the healthcare practitioner's office, in the emergency department, in an infectious disease containment unit, in ambulances etc. Such tests are referred to as point-of-care (POC) tests, "home tests" or "self-tests".

The implementation of POC testing has led to a substantial saving in cost and increased efficiency in various settings. POC tests implemented in a hospital setting can significantly reduce the length of stay of a patient in the emergency department. For example, one study reported a more than 25% reduction in the duration patients presenting chest pains stayed in the emergency department when POC testing was used instead of central laboratory testing.[26] POC tests also enable real time health monitoring.

The most widely used point-of-care tests are blood glucose monitoring and home pregnancy tests. Common POC tests used in clinics include hemoglobin A1c, electrolytes or basic metabolic panels, HIV and influenza tests.[27] Except for glucose monitoring, most

of these test are paper based, designed only for qualitative diagnosis. Also, the sensitivities and specificities of some platforms are not high enough, therefore, central lab tests are still needed following the initial point of care tests. Moreover, the number of tests available are limited.

For the above reasons, POC testing and POC sensors have become a hot research area in recent years. Many research groups have continued the usage of paper as a sensing platform, because it is a readily accessible and inexpensive material and it has natural "filters" and "pipelines" that could help solution handling.[28] Augmented with the color readers, paper based lateral flow assay nowadays can give both qualitative and quantitative information.[29] Apart from paper-based POC sensors, nanomaterial based biosensors also show promise for POC applications, for example, porous silicon (PSi) based biosensors. Owing to its tunable optical properties, PSi could be used to make label-free biosensors with relatively high sensitivity. Because of the easy fabrication and lift-off technology, PSi membranes could be made as cheap as paper. Another emerging technology which has started to be incorporated into POC sensor systems is the smartphone. The high-quality camera, the controllable and bright LED flash light, the superb computing power, convenient applications (APPs, programs running on smartphones) and internet connectivity make smartphones a very attractive platform to integrate with biosensing systems. Smartphone based microscopes,[30, 31] spectrometers,[32, 33] fluorimeters,[34] SPR sensors[35, 36] and ELISA readers[37] have been reported. These close to lab-grade tools could very beneficial for POC testing.

1.3 Porous silicon

1.3.1 PSi Formation and Fabrication

Porous silicon (PSi) was first discovered in Bell Laboratories in the mid-1950s, while researchers were electrochemically etching silicon wafers for use in the microelectronics industry.[38] 40 years later, the interest in PSi was reignited after its visible photoluminescence was discovered.[39] More recently, over the past two decades, PSi gained renewed attention to biosensing and drug delivery applications due to its large specific surface area, controllable pore size and morphology, versatile surface chemistry, and biocompatibilty.

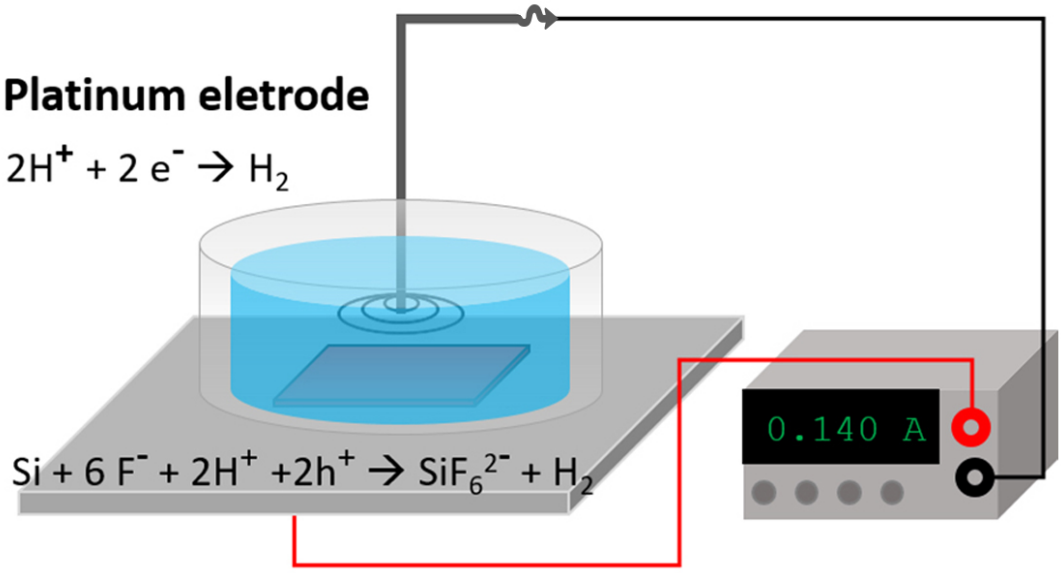

Figure 1.3: Schematic of a two - electrode electrochemical cell used to make porous silicon. The etching cell is filled with HF based solution. Silicon is the anode, also known as the working electrode. The platinum spiral immersed in HF is the cathode/ counter-electrode.

One of the major advantages of PSi over other materials is its ease of fabrication; the most common way to fabricate PSi films is electrochemical etching. Figure 1.3 shows a typical small etching cell in a two-electrode configuration. The etching cell was filled with hydrofluoric acid (HF) based solution. A small piece of crystalline silicon (<100> direction) was diced, attached to aluminum plate, and fixed to the bottom of the cell as the working electrode (Anode). A platinum wire was spiraled and immersed in the HF

solution, serving as the counter electrode (cathode). A current source controlled by the computerized etching program was connected to the corresponding electrodes. Anodization is often carried out in the dark to avoid photocurrent-induced variability in the etching process.

When current passes through the anode, silicon is oxidized to +4 state, forming SiF_6^{2-} ions, and is removed from the substrate. In the cathode, protons (H^+) gained the electrons and are reduced to H_2 (g): as a result, gas bubbles surrounding the platinum spiral can be clearly seen.

The pore formation can be controlled by multiple chemical and electronic parameters. On the wafer side, the factors include doping type and impurity level (concentration). Generally, n-type silicon can form larger pores, whereas p-type wafers can form pores with better uniformity. On the electrolyte side, low concentration of HF induces larger pores even at lower current density, while high concentration of HF generates smaller pores at low current density; wafers in high HF concentration can also withstand higher current densities.[40] When HF concentration is lower than 10%, direct electropolishing is observed without porous silicon formation. In this thesis, we use a 15% of ethanolic HF concentration (actual concentration varies between 14.4% - 15.3%) to do the electrochemical etching. Under this condition, larger current density results in a larger pore size, higher porosity and faster etching rate. For given etching rate (fixed current density), the layer thickness of PSi is determined solely by the etching time.

1.3.2 PSi vertical photonic structures

a) Thin film interferometer

The most common PSi sensing structure is a single layer of PSi, also referred to as PSi thin film interferometer. Figure 1.4(a) exhibits an scanning electron microscope (SEM) im-

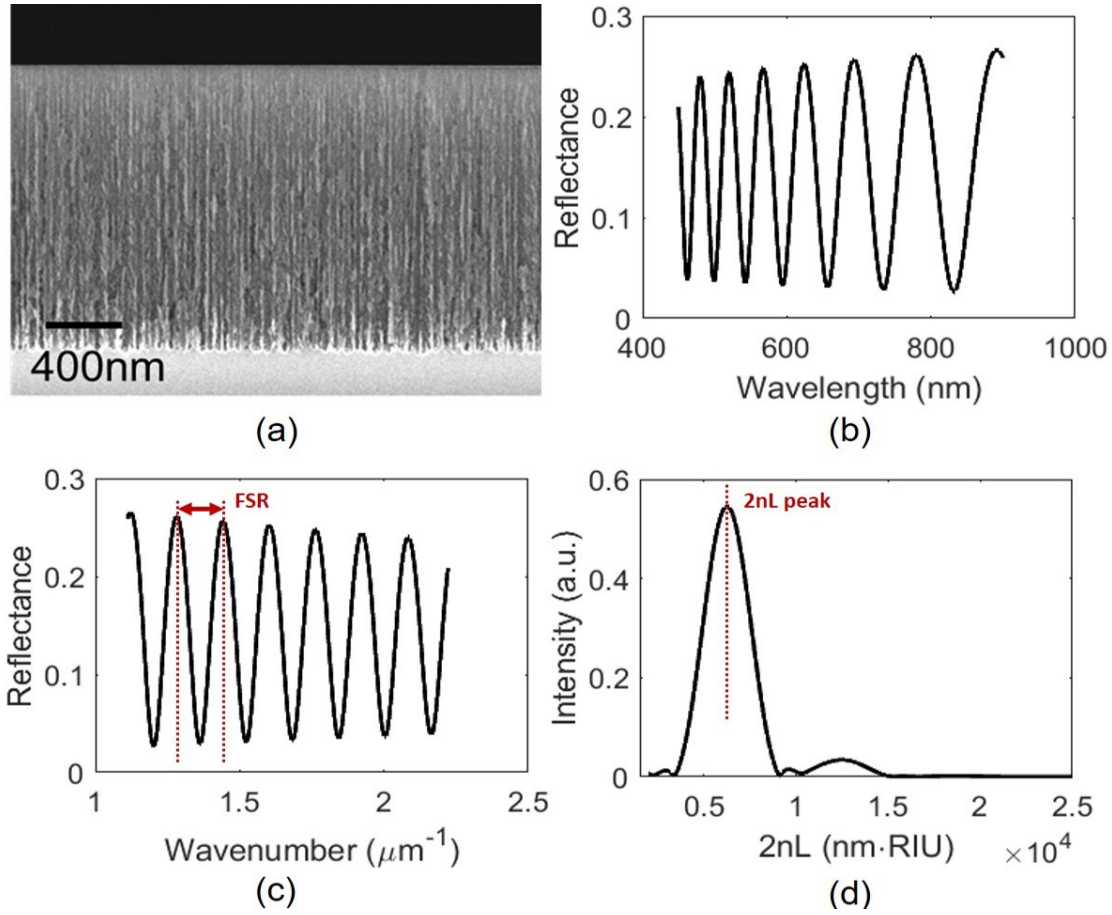

Figure 1.4: (a) The cross-sectional SEM image of a PSi thin film interferometer, and (b) its simulated reflectance spectrum in wavelength space ranging from 450 nm to 900 nm. (c) The reflectance spectrum in inverse wavelength space with the two dashed lines indicating the free spectral range (FSR), and (d) the FFT of the fringes in spectrum (c) giving the 2nL peak.

age of a PSi single layer. Under normal incident light, the reflectance spectrum (reflection vs wavenumber) of the single layer features a sinusoid shaped signal, exhibiting Fabry-Perot fringes, which are formed due to the interference of the light reflected from the top and the bottom surface of the PSi film. The phase difference of the two waves is $\frac{2\pi}{\lambda} \cdot 2nL$. Maxima are observed when

$$\frac{2\pi}{\lambda} \cdot 2nL = m\,(2\pi), \quad or \quad \lambda = \frac{2nL}{m} \qquad \text{(Eq 1.2)}$$

where λ is the wavelength of incident light, n is the effective refractive index (RI) of the

thin film, L is the film thickness, m is an integer, and the product nL, is referred to as effective optical thickness (EOT).

In the sensing process, biomolecules will infiltrate into the PSi pores. A change of RI of the single layer will cause an apparent spectral shift of the Fabry-Perot fringes. This shift could be determined by monitoring the position of a certain reflectance fringe peak, and the shift could be then used to quantify molecular infiltration and binding. However, if the shift is comparable to the distance between two peaks (free spectral range, shown in Figure 1.4(c)), the direct peak shift method will cause confusion. The fast Fourier transform (FFT) is the classic way to measure spectral shifts. Taking an FFT of the reflectance data as a function of the wavenumber produces a peak centered at 2nL (shown in Figure 1.4 (d)). By comparing the EOT before and after molecule infiltration, a blueshift (spectrum shift to shorter wavelength direction) or redshift (spectrum shift to longer wavelength direction) can be immediately resolved. Recently, Barillaro et al. reported a data processing method for PSi single layers, termed interferogram average over wavelength (IAW), and demonstrated orders of magnitude improvement in biosensing detection limit.[24] This paper gathered lots of attention from the PSi community, but few people have successfully transferred the methods to other biosensing schemes, despite using the same interferometer structure. Also, since the contribution of every wavelength was taken into consideration by the algorithm, and integrated as an absolute value to achieve the final result, both the blueshift and redshift of a spectrum will give positive results, so a stable surface chemistry is required to avoid confusing blueshifts with redshifts.

b) PSi double-layer structures

As shown in Figure 1.5(a), another common type of PSi structure is double-layer. It can be etched by switching the current density in the middle of electrochemical etching. Intuitively, double-layer structures are vertical cascades of two PSi single layers of different refractive indices. The PSi double layer reflectance spectrum (shown in figure 1.5(b)) can

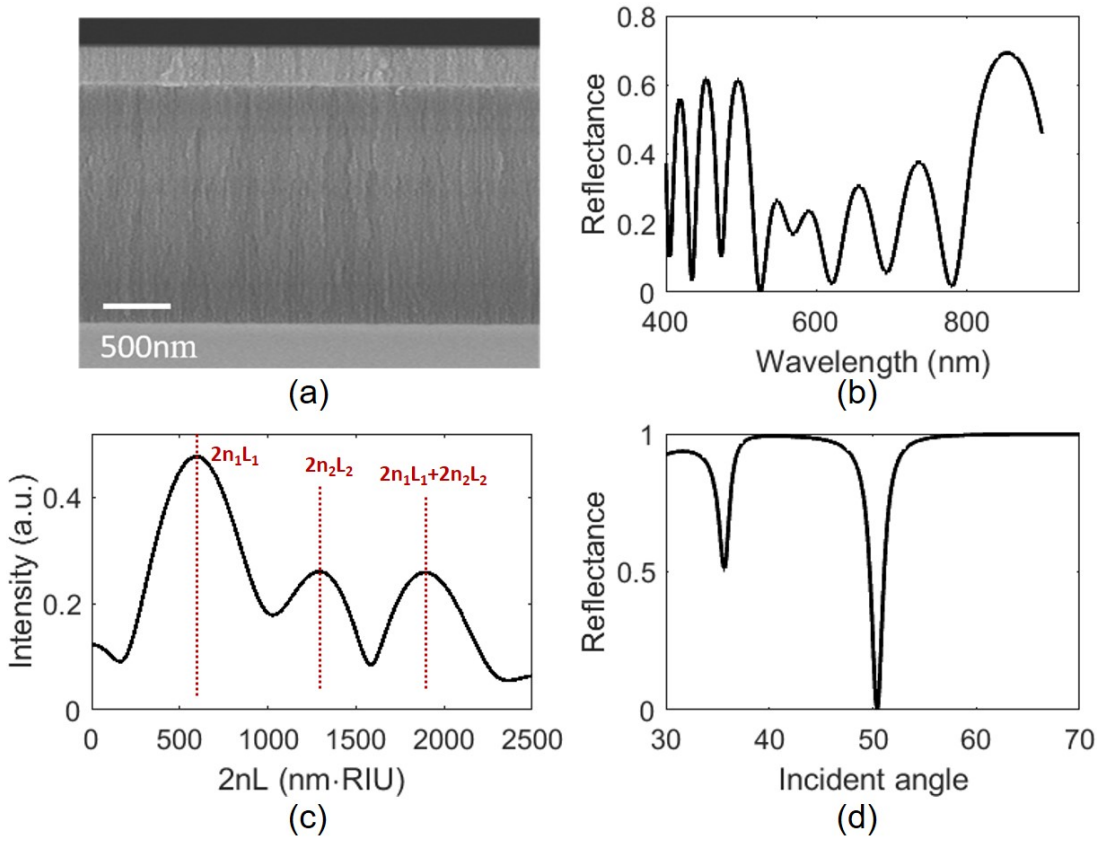

Figure 1.5: (a) The cross-sectional SEM image of a PSi double-layer thin film and (b) its simulated reflectance spectrum in wavelength space ranging from 450 nm to 900 nm. (c) FFT of a reflectance spectrum. (d) The angular reflectance spectrum of a double-layer thin film acting as a waveguide.

reveal the refractive index change of both of the porous silicon layers after biomolecule infiltration. From this information, the number of biomolecules in the pores of each of the two layers can be separately estimated. By taking the FFT of the normal incidence reflectance spectrum of the PSi double-layer structure, three peaks can be revealed (shown in Figure 1.5(c)). The first two correspond to the EOT of the two individual PSi layers, and the third peak is the sum of the EOT of the first two layers. Such structures have been demonstrated to separate biomolecules based on size,[41] and have the potential to serve as the building blocks for the machine learning based sensor arrays discussed in Chapter 5.

If the top layer has a higher refractive index than the bottom layer, the double-layer PSi

can function as a simple waveguide. With the assistance of a prism or integrated grating, when the wave vector of the incident light matches the coupling condition of the waveguide, most of the light is confined inside the high index waveguide layer due to the total internal reflection occurring at the interfaces of air/ waveguide and waveguide/ cladding layer (low index PSi layer). A resulting sharp dip can be seen in the reflectance spectrum as shown in Figure 1.5(d).[42, 43]

c) PSi Bragg stack

If two layers of PSi with high and low porosity, respectively, are repeated to form an alternating stack, a Bragg stack can be formed when the two layers have the same EOT. Despite its wide use for many optical applications, such as a component of filters, there are few examples of Bragg stacks being used as biosensors. PSi Bragg stacks may potentially be used as filters for POC applications however, particularly if the index difference (Δn) of the two layers is small, which decreases the bandwidth of the Bragg stack central peak. When (Δn) is small, the Bragg stack becomes a narrow band Bragg stack (NBBS), and the reflectance spectrum resembles the Rugate filter, a photonic structure of sinusoidally varying RI. Both NBBS and rugate filters have been used for biosensing. [44, 45]

d) PSi Microcavity

Another photonic structure closely related to the Bragg stack is the microcavity. Microcavities can be seen either as two Bragg stacks sandwiching a cavity, or an imperfection inside the perfect periodic Bragg stack structure. The reflectance spectrum of the microcavity features a sharp resonance dip in the center of a broadband high reflectance region, which corresponds to the defect mode inside the photonic bandgap. In the structure, light is strongly confined in the central cavity and the resonance position is extremely sensitive to the EOT of the center layer. The reflectance spectrum shows the resonance change when there is a RI variation in the cavity or in other layers. This characteristic makes the micro-

cavity a natural antifouling biosensor. Any binding on top of the PSi layer will have little effect on the position of the resonance dip. One major challenge with using microcavities for sensing is restricted mass transportation. High-quality PSi microcavities require many periods of alternating high and low porosity films. Both the thickness and small pores layers will have a major impact on diffusion. Therefore, microcavity-based PSi biosensors are commonly used for small biomolecule sensing.[46, 47]

1.4 Overview of the Dissertation

This work focuses on three aspects of utilizing PSi biosensors for point of care applications –building cost-effective portable platforms, incorporating environmentally stable bioreceptors and designing new-concept biosensing systems.

Chapter 2 details the working principles and operating procedures of the systems (tools) used for PSi materials characterization and PSi devices measurement (signal acquisition).

Chapter 3 presents a smartphone based PSi biosensor that uses a smartphone camera as the detector and smartphone LED as the light source. The sensor detects the biomolecule attachment through monitoring PSi structural color changes.

Chapter 4 examines the ways to include a more robust bioreceptor, peptides, to the PSi matrix in order to achieve biosensing in harsh conditions.

Chapter 5 uses machine learning techniques to explore the possibility of differentiating biomolecules through their interactions with PSi films.

Chapter 6 provides a concluding summary and future research opportunities that will further improve the PSi-based sensing technologies demonstrated in this work. Overall, the development of cost-effective portable platforms, robust bioreceptors and new-concept

biosensing systems is significant progress towards cost-effective, long shelf-time, and reliable POC sensing technologies based on PSi.

CHAPTER 2

Characterization and measurement

2.1 Introduction

Refractive index and layer thickness are key optical properties of layered photonic structures, while pore size and pore morphology dictate how biomolecules interact with the physical PSi matrix. To quantify these properties, scanning electron microscope (SEM), atomic Force Microscopy (AFM), reflectance spectrometry and ellipsometry can be used. The working principles of SEM and operating procedures for PSi chip characterization are detailed in the first part of the chapter. After device fabrication and characterization, spectrometry methods are performed to measure the optical properties of the devices. A grating based spectrometer, prism coupling system and fiber coupling system can be used for experimental measurements. The working principles of reflectance spectrometer and operating procedures for PSi device measurements are detailed in the second part of this chapter.

2.2 Scanning electron microscopy

Due to diffraction, the smallest feature resolvable by a typical optical microscope is approximately equal to half the wavelength of incident light. As the pore diameters of the PSi used in this thesis are between 10-100 nm, optical microscopes are not suitable for resolving the pores and thus SEM imaging is used. SEM is a microscope that produces images of a sample surface based on the information obtained by scanning the surface with a focused beam of electrons. As high energy electrons have an extremely short wavelength (for example, 30 keV electron beam has a wavelength of 7 pm), the Abbe limit is no longer the

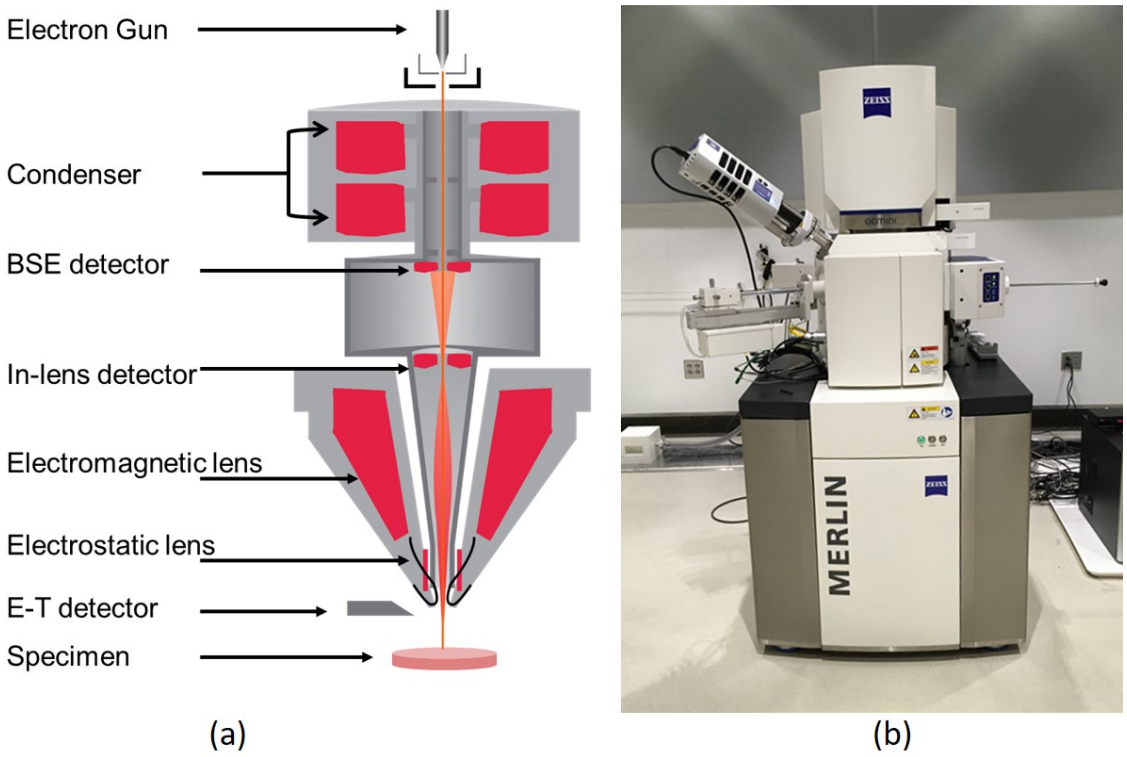

Figure 2.1: (a) The cut-away view of a SEM. (b)Photo of a Zeiss merlin SEM used to characterize the nanomaterials and devices.

ultimate restriction. The general architecture of an SEM consists of an electron gun, several electromagnetic lenses (condenser lens, objective lens), electron detectors (secondary electron detector, in-lens detector and back scattering electron detector), a sample chamber, a control system and a software interface for interaction. Figure 2.1 presents (a) the cut-away view of the internal structure of an SEM and (b) a photo of Zeiss Merlin SEM used in this thesis.

In a typical SEM, an electron beam is emitted from an electron gun either thermally or through the repulsion of a strong electric field (or a combination of both). After going through multi-stage acceleration and deflection by the electromagnetic lenses, the beam is finally focused on the sample surface. When the primary electron beam of high energy hits the sample, the electrons undergo repeated random scattering and absorption, and sec-

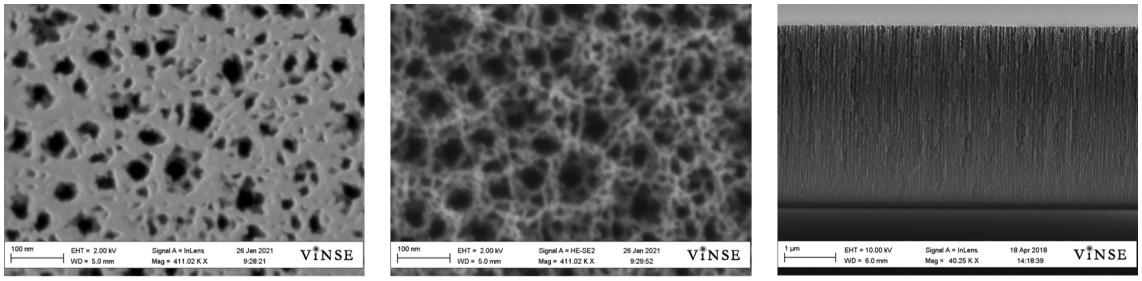

(a) (b) (c)

Figure 2.2: The top view of PSi fabricated using a current density of 70 mA·cm^{-2} in 15% HF for 100 sec, using (a) in-lens mode and (b) HE-SE2 mode. (c) The cross-sectional view of sample fabricated in the same condition.

ondary electrons are generated within a teardrop-shaped volume of the specimen known as the interaction volume. Higher energy electrons have a shorter wavelength, but a deeper penetration depth and a larger interaction volume, while lower energy electrons have a longer wavelength, but a smaller interaction volume. Therefore, voltage selection is crucial for producing images of the desired resolution. For the Zeiss Merlin SEM in Fig 2.1 (b), the best resolution at 200V is 2 nm; this reduces to 0.6 nm at 30 kV according to the manufacturer's specifications. [48] Among all information generated from the electron-sample interaction, signals from the secondary electrons are the most important for imaging. Based on the generation mechanism, secondary electrons (SE) can be further classified as SE1-SE4. The SE1 are generated by the primary electron beam interaction with the sample; SE2 are generated by interaction between the sample and the high energy back-scattering electrons (BSE); SE3 are the result of BSE colliding with the chamber and column components of the SEM; and SE4 are generated by primary electrons interaction with apertures and other SEM column components, which are independent of the sample characteristics. [49]

Different detectors are used to capture electrons of different types. The Everhart-Thornley (E-T) detector is the most frequently used device for the detection of SE. The electrons it collects include SE1-SE4.The wide range of SE has been recognized as a limit-

ing factor in SEM resolution because the dominant SE2 and SE3 are delocalized electrons that were generated from the region far from the primary electron beam. In contrast, in-lens (or through the lens) collects mostly SE1 electrons, which makes it more sensitive to the surface and higher resolution. Figure 2.2 (a) and (b) are images collected in in-lens and HE-SE2 (E-T detector) modes respectively. Figure 2.2(c) shows a cross-sectional SEM image of a PSi film, which can be used to estimate the film thickness. The PSi sample must be cleaved with a diamond scribe to enable imaging of the cross-section.

2.3 Reflectance spectrometry

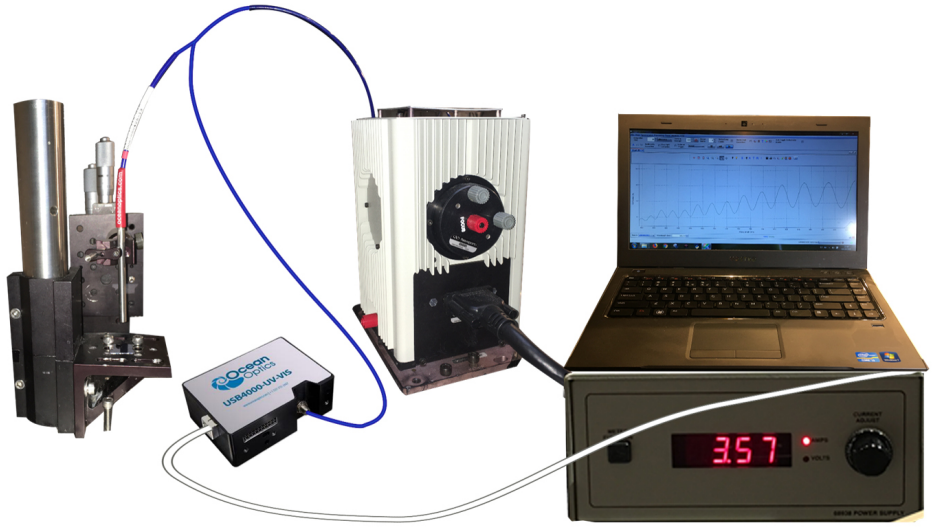

Figure 2.3: An optical reflectance spectrometric measurement system, consists of a light source, an optical stage, a spectrometer, a power supply and a software interface.

A fiber optic spectrometric system was used for reflectance measurements. The system consists of a light source, an optical stage, a spectrometer connected by an optical fiber, a power supply for light source and a laptop for collecting the digital signal. The light beam generated by the light source transmits through the fiber and illuminates the sample on the stage. The light reflected back is collected by the fiber and transmitted to the spectrometer. Inside the spectrometer, the light is diffracted by a grating, projected onto a CCD array

and transformed to a digital signal. Finally, the signal is sent to the computer and the spectrum is displayed. The spectrometer used in this thesis is Ocean Optics USB4000, which features a dynamic range of 200 to 1100 nm and an optical resolution of 0.1 to 10 nm. The spectrometer can be used for both single spectrum measurement and real time spectral monitoring. A simple method to measure the refractive index is to use SEM to measure the thickness of a single layer and use the FFT of the reflectance spectrum to obtain the optical path length.

CHAPTER 3

Smartphone biosensors

Notes to readers : Much of the chapter was adapted with permission from two of my previous publications:

1. Tengfei Cao, Yiliang Zhao, Sharon M. Weiss, "*A smartphone compatible colorimetric biosensing system based on porous silicon,*" Proc. SPIE 10077, Nanoscale Imaging, Sensing, and Actuation for Biomedical Applications XIV, 1007713 (22 February 2017); https://doi.org/10.1117/12.2250659 [50]

2. Tengfei Cao, Yiliang Zhao, Crystal A Nattoo, Rabeb Layouni, and Sharon M Weiss. *A smartphone biosensor based on analysing structural colour of porous silicon*. Analyst, 144 (13): 3942–3948, 2019. https://doi.org/10.1039/C9AN00022D[51]

3.1 Introduction

Low-cost point of care (POC) diagnostic biosensors have drawn great attention from the research community, for their broad impact on diagnostics in low-resource regions and the convenience of at home health monitoring.[52] It is also reported that POC biosensor deployment is beneficial to clinics and reduces the processing time and financial cost to patients. Most types of current POC biosensors are paper-based, the results of which are displayed by the presence of certain lines or colors comparing to the control sample (or standard chart). Relative to other platform, paper-based biosensors are generally simple, affordable and easy to use. These factors are largely attribute to the fact 1) that paper is a readily accessible and low-cost material; 2) paper has been widely used in analytical chemistry as the carrier for the chemical assays, and many surface functionalization have been developed; 3) paper is inherently good at handling fluids, and it could be used both

as a filter and a pipeline (forms of channels).[28] However, most paper-based systems are of low precision, and they are designed to be qualitative or semi-quantitative. Even though some paper-based biosensors, augmented with digital readers, could give both qualitative and quantitative information, the rough surface and large non-uniform pores of the low-cost paper platform are the ultimate limiting factors for the precision of the biosensor. Another widely applied POC biosensor is electrochemical glucose sensor, which works by monitoring the enzyme-catalysed glucose oxidation.[53] Because of the importance of blood glucose monitoring, the glucose sensor is and one of the most popular and established POC systems. However, as the system is designed for glucose monitoring, it's of single functionality and hard to transfer to other analytes.

Recently, the low-cost, easy-to-fabricate and versatile material PSi has shown promise for POC applications. However, whilst PSi mainly serves as a transducer, the light source, spectrometer and data processing units are needed for the entire sensing process. Nowadays, the spectrometer can be very small in size, but it is very costly to obtain precision high enough for sensing. Moreover, a relatively stable light source is heavy and bulky. An emerging technology that has the potential to transform the field is smartphone.[54] Smartphone features high resolution cameras, superb computational power, a bright LED light and high speed internet connection, which could all be repurposed for biosensing. More importantly, smartphones are widely available. It's reported that there are areas where people do not have access to clean water, but have access to smartphones.[55]

Even before the term "smartphone" gained its prevailing popularity, camera-enabled mobile phones had already been demonstrated capable of capturing images from the eyepiece of a standard microscope and wirelessly transmitting the images for subsequent analysis.[58, 59] The first fully integrated and portable mobile phone microscopy system was built by Breslauer et al.[30] As shown in Figure 3.1(a) the system attached a miniaturized microscope lens system to the cell phone and demonstrated its potential for clinical

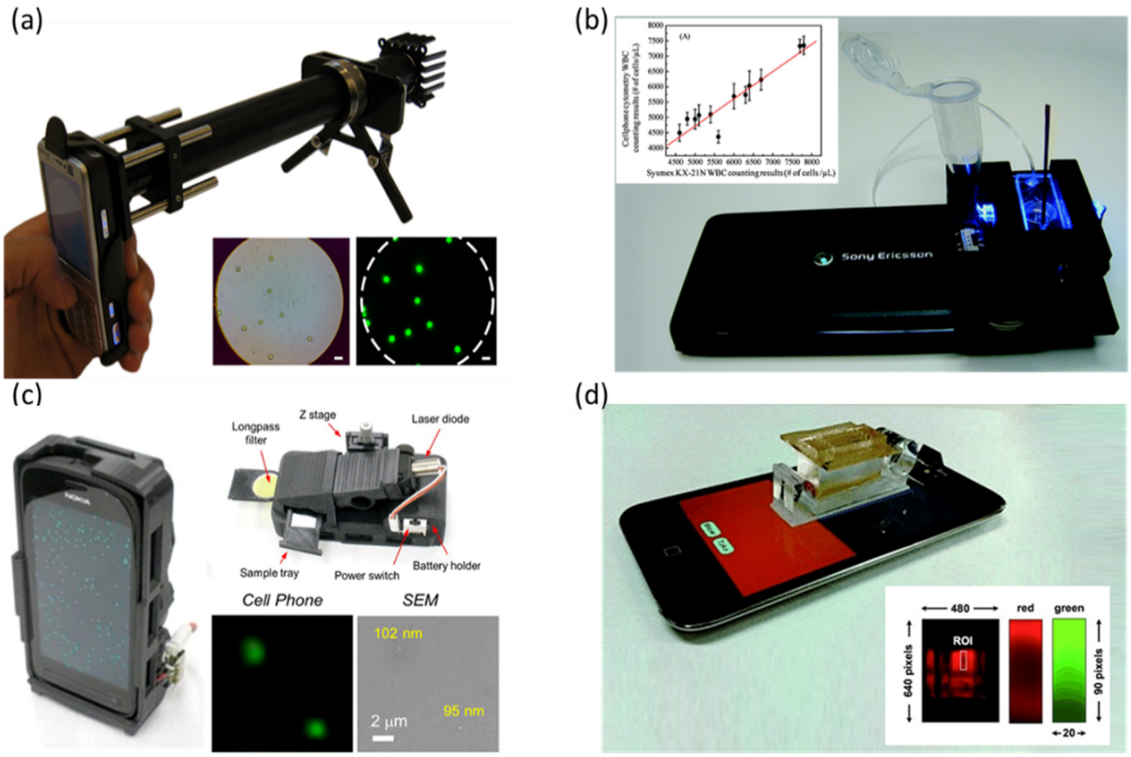

Figure 3.1: Smartphone biosensors reported in recent years. (a) A smartphone microscope equipped with lenses, filters and LEDs, capable of fluorescence imaging. Inset is fluorescent image (right) of the beads (left), with scale bar of 10 μm, adapted from Ref [30] under the terms of the Creative Commons Attribution License, Copyright 2009 Breslauer et al. (b) An optofluidic fluorescent imaging cytometer. The inset shows its performance compared to an analogous desktop system, adapted with permission from Ref [56], Copyright (2011) American Chemical Society. (c) A Smartphone-based fluorescence microscope (left), its back view (top right) and the fluorescent image captured (left) of the beads (right), adapted with permission from Ref [57], Copyright (2011) American Chemical Society. (d) A smart-phone angular SPR sensor. Inset shows image measured under red illumination (left), and a region of interest (ROI) used for evaluation, under red and green illuminations (center and right, respectively).Adapted with permission from Ref [36], Copyright 2012 WILEY-VCH Verlag GmbH & Co. KGaA, Weinheim.

use by imaging P. falciparum-infected and sickle red blood cells in bright field and M. tuberculosis-infected sputum samples in fluorescence with LED excitation, where the system resolution (estimated to be $\sim 1.2\ \mu m$) suffices to detect blood cell and microorganism morphology in all cases. Shortly after, Tseng et al. reported a lens-free microscope based on incoherent in-line holography.[31] The system successfully reconstructs the microscope images of micro-particles, blood cells and waterborne parasite from the hologram with a spatial resolution of 2.2 μm for each color pixel. Later, a cell phone based optofluidic fluorescent imaging cytometry was demonstrated (Figure 3.1(b)).[56] The cytometer measures the white blood cells in human blood samples by counting them in the cell-phone camera recorded fluorescent movies, which show decent performance compared to the commercially available hematology analyzer. The resolution for the fluorescent images is about 2 μm. In addition, a portable fluorescent microscope of subwavelength resolution is reported.[57] With the help of fluorescent nanoparticles, the system has been applied to detect the human cytomegaloviruses with a molecular size of $\sim$ 200 nm and shows the capability to resolve small nanoparticle with size down to 100nm. (Figure 3.1(c))

Alongside microscopy, the smartphone has also been extensively adopted for spectrometry, which is one of the most important technologies for bio-quantification. Based on angle-resolved surface plasma resonance (SPR), Preechaburana et al reported a smartphone SPR sensor showing comparable performance with compact SPR system, which measures a refractive index change down to 2×10^{-6} RIU (Figure 3.1(d)).[36] Gallegos et al reported a label-free biosensor, which measures the resonant wavelength value of a photonic crystal with a 12 pm accuracy.[32] The biosensor has been modified with Protein A for detecting porcine immunoglobulin G (IgG), which exhibits a detection limit of 4.25 nM. Recently, the same group has developed a multimode smartphone biosensing analyzer,[60] which combines the functionalities of transmission, reflection, and intensity spectral measurements. The analyser is capable of achieving comparable limits of detection to the result obtained by the conventional laboratory microplate reader.

Even though there are existing detectors for paper-based diagnostics, the needs for simple and easy detection tools has not been fully realized. However, paper colorimetric biosensors have also been transformed by smartphone integration By correlating the hue value of smartphone images to the tested pH value on the standard chart, Chang demonstrated the possibility of using smartphone to read pH paper.[61] With the help of additional optical accessories, Erickson Group developed: a smartphone pH reader for sweat and saliva, which could be used to monitor the body condition to prevent the risk of dehydration and to improve performance during physical activity;[62] a cholesterol sensor that could measure a cholesterol range of 140 $mg \cdot dl^{-1}$ to 400 $mg \cdot dl^{-1}$ within an accuracy of 1.8%;[63] a vitamin D sensor using gold nanoparticle based immunoassay to accurately measure physiological levels of 25-hydroxyvitamin D with accuracy better than 15 nM and a precision of 10 nM;[64] and a lateral flow assay for iron and vitamin A deficiency.[65]

Most of the reported smartphone-based systems exhibit low cost, great portability, and adequate sensitivity for POC testing, sometimes even comparable to conventional desktop devices.[34, 35, 37, 66, 67] However, an evaluation of the system compatibility with various kinds of smartphone, the cost of the entire process and reliability needs careful investigation for real application.[59]

In this chapter, we will present a smartphone based porous silicon optical biosensor, from the working principle and proof-of-concept system, to the prototype and the possible improvements.

3.2 Working principle of structural color-based biosensor

Most label-free optical biosensors operate based on detecting spectral shift induced by a refractive index change that takes place upon the capture of chemical or biological molecules onto the biorecognition elements.[50] Generally, the spectral shift is measured by spec-

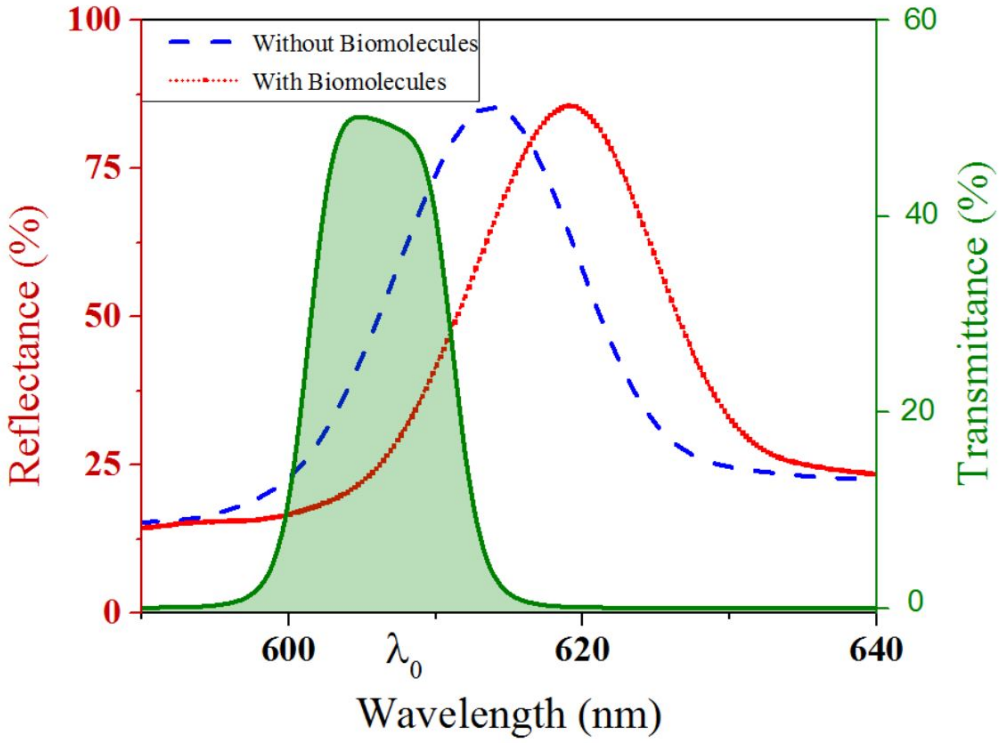

Figure 3.2: Reflectance spectra of a PSi rugate filter before (blue dashed line, SB) and after (red dotted line, SR) adding biomolecules. The reflectance spectrum redshifts after molecular binding in the pores. The transmission spectrum of a commercial bandpass filters (solid brown line corresponding to the secondary y-axis) is overlaid to indicate which portion of the reflectance spectrum reaches the detector.

trometers or spectrophotometers. Alternatively, the spectral shift could also be tracked by monitoring the change of reflectance intensity at a fixed wavelength, illustrated in Figure 3.2: the blue dashed line is the reflectance spectrum of the transducer (SB) and red dotted line is the spectrum (SR) after the biomolecule is attached. Observing at wavelength λ_0, the SR has a lower reflectivity compared to the SB, which indicates less reflected light at wavelength λ_0 would be detected after the molecular binding. To resolve the change, a narrow bandpass filter, whose transmission spectrum is shown as the brown curve in Figure 3.2, was used to extract the light intensity around λ_0. Since the reflectivity of SR is lower than SB within the high transmittance wavelength region of the filter, the filtered reflected beam from SR will have a lower intensity compared to SB. Accordingly, with the

right combination of the properties of the sample and the filter, the wavelength shift in reflectance spectra can be correlated with the change in light intensity. The discussion here is based on the assumption of uniform incoming light intensity and uniform detector spectral sensitivity across the entire spectral range. However, for narrow bandwidth filters with near zero transmission outside the designed bandpass region, the discussion is still valid even with imperfect light sources and detectors provided that the incoming light spectrum and detector spectral sensitivity curve do not undergo sharp changes within the transmission window.

3.3 Proof of concept system of structural color-based biosensor

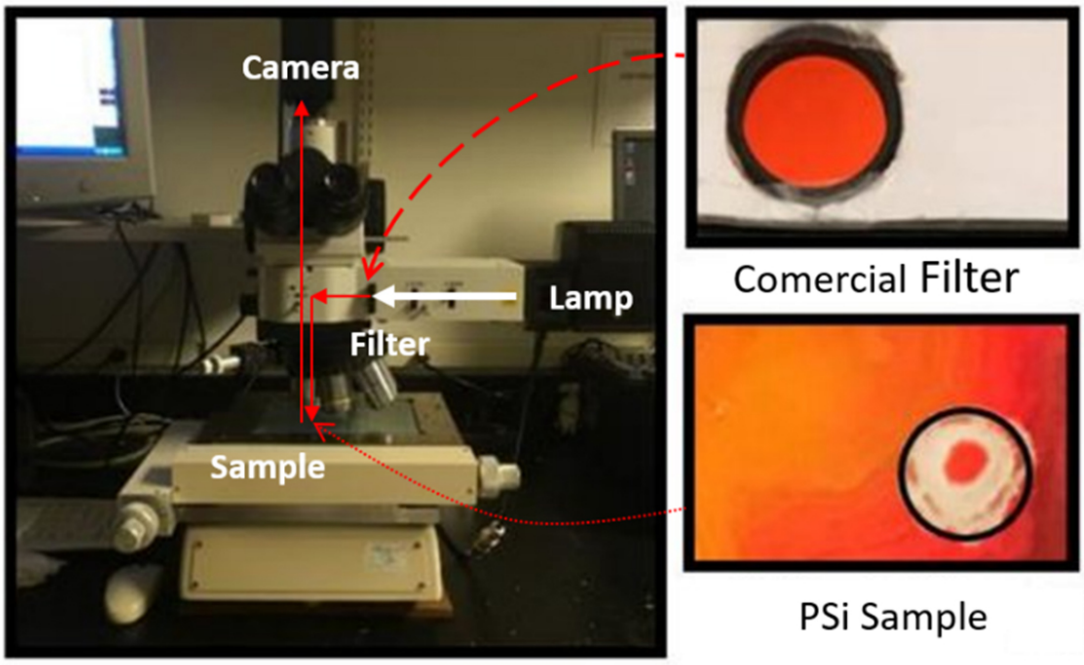

Figure 3.3: Proof-of-concept colorimetric biosensing system. Left—optical microscope with attached camera used for imaging and the schematic illustrations. Top right—commercial bandpass filter with the FWHM = 10 nm. Bottom right—PSi sample. The red circular region inside the black circle is the isolated region of the PSi NBBS filter used for detection. The surrounding white region is where PSi has been scratched away to facilitate sample positioning.

A proof of concept system of the PSi biosensor was built on an optical microscope equipped

with white light source and digital camera. (Shown in Figure 3.3) A commercial bandpass filter with a peak wavelength of 610 nm and full-width-at-half-maximum (FWHM) of 10 nm is inserted in front of the light source to limit the range of wavelengths incident on the PSi sample and facilitate the measurement of the intensity of reflected light from the PSi sample. The white light was emitted from the lamp, filtered by the red filter, reflected the PSi sample and finally received by the digital camera. The intensity of the reflected light can be extracted directly from the camera images. Digital images can be represented by an associated set of RGB values, which have monotonic correlation with the light intensity detected by the red, green, and blue sensors of the camera. Therefore, the intensity of reflected light by the sample can be obtained by analyzing the RGB values of an image. Only the R value is considered in this study because most of the light that the camera captures is in the red region due to the selected bandpass region of the commercial filter. The microstructure of the PSi sample used here is a narrow band-width Bragg stack (NBBS), which is composed of alternating quarter wavelength dielectric stacks of high and low refractive indices. The PSi NBBS were prepared by anodic electrochemical etching of p type silicon wafers in 15% hydrofluoric acid. The samples were prepared in a Teflon etch cell with a 2 cm^2 etching area. A platinum spiral was immersed in the etching solution as the counter-electrode and an aluminum sheet was attached to the back of the silicon wafer to serve as the backside contact. The PSi NBBS was fabricated by applying alternating current densities (52 $mA \cdot cm^{-2}$ and 60 $mA \cdot cm^{-2}$) to form alternating PSi layers with different refractive indices. These particular etching conditions were selected to create NBBS with peak reflectance outside the bandpass of the commercial filter such that a steep slope in the reflectance spectrum occurred within the bandpass to enable large intensity changes for small spectral shifts. After etching, the samples were rinsed with methanol and dried in a stream of nitrogen, before annealing in a furnace at 1000 $^{\circ}C$ for 20 s.

The reflectance spectra were measured by an Ocean Optics USB-4000 spectrometer with a wavelength range over 400-900 nm. The PSi samples were fixed on the glass slides

for positioning purpose. Images of PSi samples were captured by the camera on a microscope.

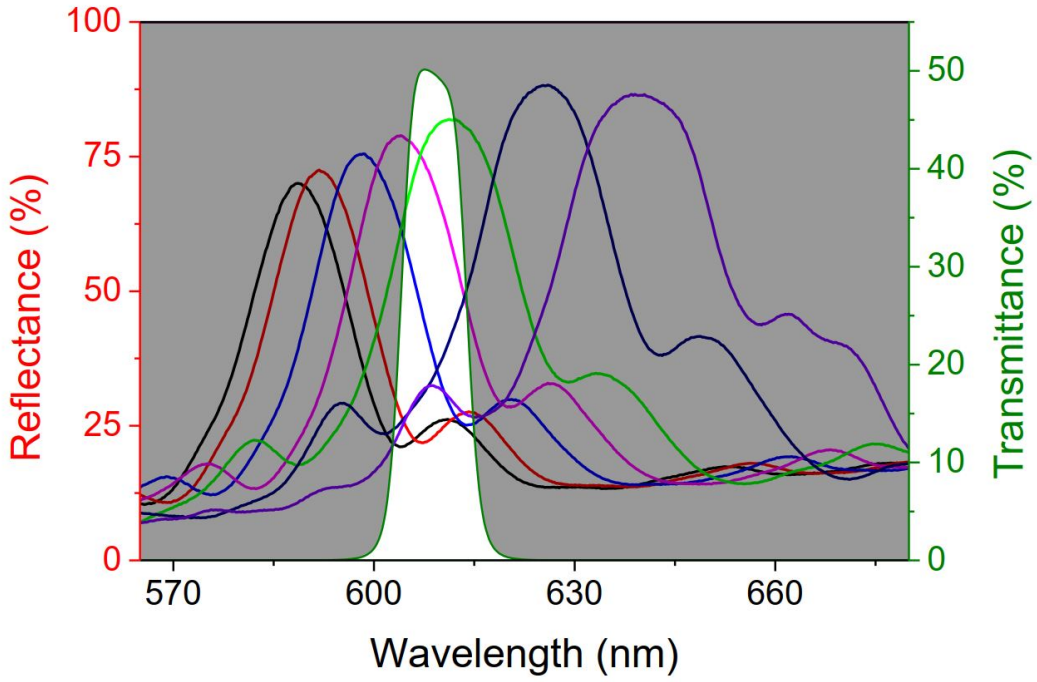

Figure 3.4: Reflectance spectra (solid lines) and corresponding camera images (insets) of PSi NBBS after infiltration with various concentrations of glucose. The reflectance spectra redshift upon exposure to increasing glucose concentrations. The transmission spectrum of the commercial filter (dashed line) is also shown to indicate which region (highlighted by the white colored region on the graph) of the reflectance spectra can be detected by the camera.

For initial demonstration of the sensing system, a PSi NBBS sample centered around $\sim$ 590 nm with a FWHM of 20nm was rinsed in a series of glucose solutions with different concentrations (concentration 1-7: 0 g $\cdot$ L^{-1}, 40 g $\cdot$ L^{-1}, 80 g $\cdot$ L^{-1}, 120 g $\cdot$ L^{-1}, 160 g $\cdot$ L^{-1}, 200 g $\cdot$ L^{-1}, 240 g $\cdot$ L^{-1}). Before measurement under the microscope, the sample was dried in nitrogen. (A single sample exposed to increasing concentration of glucose). To determine the refractive index sensitivity of the NBBS filter, PSi samples were immersed in glucose solutions with concentrations 0 g $\cdot$ L^{-1}, 20 g $\cdot$ L^{-1}, 40 g $\cdot$ L^{-1}, 60 g $\cdot$ L^{-1}, 80 g $\cdot$ L^{-1}, and 100 g $\cdot$ L^{-1}, and then measured with the Ocean Optics spectrometer. In addition, a series of dilute glucose solution (0 g $\cdot$ L^{-1}, 1 g $\cdot$ L^{-1}, 2 g $\cdot$ L^{-1}, 3 g $\cdot$ L^{-1}, 4 g $\cdot$ L^{-1}, 5

$g \cdot L^{-1}$, 6 $g \cdot L^{-1}$) was dropped onto a PSi NBBS filter centered at 616nm with a FWHM of 20 nm (a single sample exposed to increasing concentration of glucoses). After drying the sample under nitrogen gas, reflectance spectra were measured with the Ocean Optics spectrometer and images were taken using the microscope.

The results of the glucose sensing experiment are shown in Figure 3.4. Images taken with the microscope setup appear alongside the reflectance spectra measured by the spectrometer. The transmission window for the microscope setup is overlaid and appears as the brighter region. The peak positions of the spectra were determined to be 589 nm, 592 nm, 598 nm, 604 nm, 611 nm, 626 nm and 640 nm for glucose solutions with concentrations 1-7, respectively. The R values of the corresponding images are 127, 130, 171, 215, 225, 154 and 143. When the reflectance peak is at a shorter wavelength compared to the center of the transmission spectrum of the bandpass filter, a redshift of the spectrum corresponds to increasing brightness of the microscope images. At the higher concentrations when the reflectance peak is at longer wavelengths compared to the center of transmission window, further redshifts of the spectrum lead to decreasing brightness of the microscope images. Hence, while reflectance spectra clearly distinguish between PSi samples exposed to a large range of glucose concentrations, it would be more challenging to uniquely determine the concentration of analyte solution from image analysis alone over similarly large concentration ranges (Two spectra on different sides of the filter transmittance curve might have the same R values). Nevertheless, the dynamic range of analyte concentration represented by glucose concentrations 1-5 (i.e., 0—160 $g \cdot L^{-1}$) that yield distinct R values is sufficient for many practical sensing applications.

As shown in Figure 3.5 (a, b), increasing the concentration of glucose solutions over a smaller concentration range (0- 6 $g \cdot L^{-1}$) leads to a series of small redshifts of the reflectance spectrum for the PSi NBBS and almost imperceptible color changes in the camera images. To improve the accuracy of the R value determination from the images, contribu-

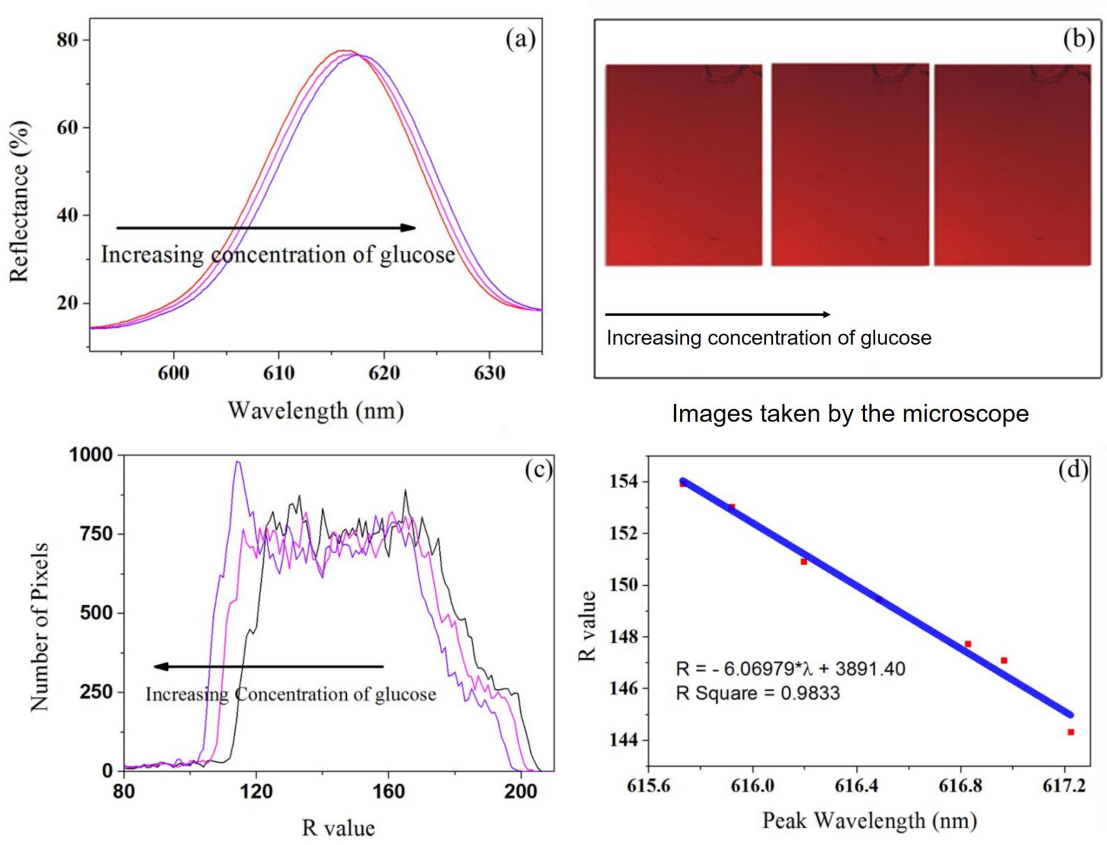

Figure 3.5: (a) Reflectance spectra of the PSi NBBS filter after infiltration with different glucose concentrations between 0- 6 g· L^{-1}. (b) Corresponding camera images for three selected PSi NBBS filters. (c) Color distribution showing the number of pixels containing a given R value for each of the PSi NBBS filters shown in (a). Extreme R-values (not shown) are filtered out during image processing, as described in the main text. (d) Correlation between R-value of camera image and peak reflectance wavelength of the PSi NBBS filter. A linear fit is shown.

tions to the R value from the unavoidable dust and bright spot on the images need to be filtered out. Accordingly, a simple image processing set was carried out on the color distribution diagram shown in Figure 3.5 (c). Only R values whose magnitudes ranging from 5% to 95% were considered as valid data. As dust generally has a low brightness (relatively small R value) and bright spots have large R values (i.e., close to 255, i.e. saturation), the color distribution method can effectively filter these factors out without affecting the integrity of the analysis. Figure 3.5(d) correlates the peaks of the reflectance spectra (in Figure 3.5a) with the R values extracted from the corresponding camera images (three of

them shown in Figure 3.5b). A linear relationship was found between the R value and peak reflectance wavelength. The smallest resolvable spectral shift determined from this fit is approximately 0.25 nm. The refractive index sensitivity of the PSi NBBS filter is 310 nm$\cdot$ RIU^{-1}, as measured with the spectrometer, which corresponds to a detection limit of 7×10^{-4} RIU for the colorimetric sensing system.

3.4 Smartphone biosensor prototype

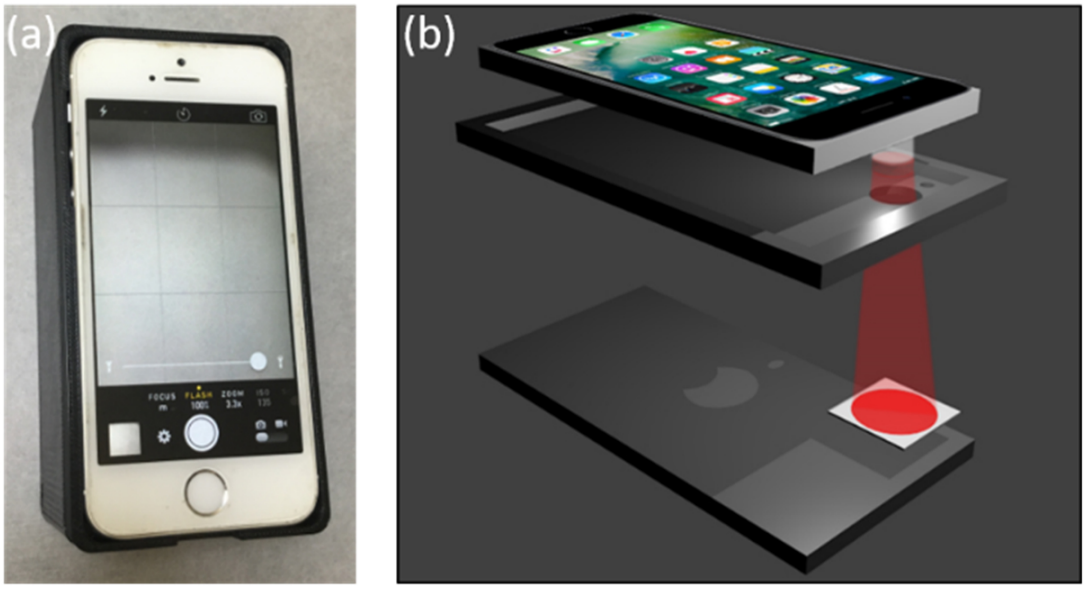

Figure 3.6: Smartphone biosensing system. (a) Photograph showing smartphone situated in 3D printed box. (b) Schematic illustration in a cut-away view showing, from top to bottom, the smartphone with red bandpass filter inserted in front of the smartphone LED flash, the top of the 3D printed box, the PSiM positioned below the smartphone camera, and the bottom of the 3D printed box.

Similar to the proof-of-concept system, we present a smartphone biosensor prototype that requires only a bandpass filter and a 3D printed box, (shown in Figure 3.6) and leverages the advantages of the high surface area sensor material, porous silicon, for the test chip. The biosensing system works by detecting the structural color change of a porous silicon microcavity (PSiM) that results when target molecules are captured in the pores of the PSiM.

This sensing approach is different from traditional colorimetric approaches that require, for example, an enzymatic reaction, fluorescent species, or nanoparticle aggregation to cause a color change. By using the built-in LED flash of a smartphone as the light source and the smartphone camera as the photon detector, a suitably designed label-free porous silicon sensor can operate without a benchtop measurement system. Moreover, a porous silicon smartphone sensor does not require external lenses or gratings. Here, we demonstrate that a label-free PSiM smartphone sensing system can operate with an equivalent accuracy of 0.33 nm and an estimated detection limit of 500 nM based on a biotin-streptavidin assay. We note that the spectrometer measurements reported in the paper are necessary only for characterizing the intrinsic properties of the system, and are not necessary for quantifying molecular detection events. Calibration between the light intensity and concentration of target molecules is the only prerequisite for quantitative detection applications.

3.4.1 Materials and methods

Materials

All chemicals were analytical grade and used without further purification. Single side polished, boron doped p-type silicon wafers ($< 100 >$, 0.01–0.02 $\Omega \cdot cm$, 500–550μm) were purchased from Pure Wafer, WRS Materials Company. N-Hydroxysuccinicmide (NHS) and 10-Undecenoic acid were purchased from Alfa Aesar. N-(3-Dimethylaminopropyl)-N'-ethylcarbodiimide hydrochloride (EDC), EZ-Link Amine-PEG2-Biotin, sulfo-NHS-biotin, streptavidin and ethanol were all purchased from Thermo Fisher Scientific. Hydrofluoric acid (HF) was purchased from Acros Organics. Deionized (DI) water ($\sim 15\ M\Omega \cdot cm$) was used as a solvent for all experiments except where noted otherwise.

Reflectance spectra measurements

Ocean Optics USB-4000 spectrometer was used for reflectance measurements over a sample area of approximately 1 mm^2 and wavelength range of 400 – 900 nm. Spectral shifts

to longer wavelengths (i.e., redshift) indicate that molecules have attached to the surface of the pores in the PSiMs while spectral shifts to shorter wavelengths (i.e., blueshift) indicate that material has been removed from the PSiMs.

Smartphone colorimetric measurements

An iPhone SE was used to carry out quantitative measurements of the colour of the PSiMs. Broadband white light was emitted from the smartphone LED and transmitted through a Thorlabs bandpass filter (centre wavelength $\lambda_0 \sim 610$ nm; full-width-at-half-maximum (FWHM) = 10 nm; see Figure 3.7c) before reflecting off the porous silicon sample. The reflected light was collected by the smartphone camera. We note that it should be possible to replace the Thorlabs bandpass filter with a free-standing porous silicon bandpass filter, if desired. To achieve a more uniform illumination, we attached a piece of white paper to the phone in front of the LED to diffuse the light, and we also added a small piece of black tape on the back side of the filter fixture to block the brightest spot of light emitted from the LED.

A custom 3D printed box was fabricated and used to hold the smartphone, filter, and PSiM in fixed positions during all measurements. A camera app was used to control the focus, flash, zoom, ISO, speed, exposure value and white balance of the smartphone camera. Videos clips of approximately 1 min were recorded instead of taking individual pictures for better accuracy and reproducibility. The videos were uploaded to a desktop computer, and a MatLab code was used to convert the videos into arrays of time sequenced intensity values. Each video was treated as a series of RGB images, and the data comprising one RGB image was exported to three matrices in MatLab that contain the intensities measured by the red (R), green (G), and blue (B) pixels, respectively, in the camera imaging sensor. In this work, we only use the R-values in our calculations because the bandpass filter restricts the incident light to red wavelengths. Detailed procedures for the smartphone measurements are provided in appendix A.1. We anticipate that the computations carried out on

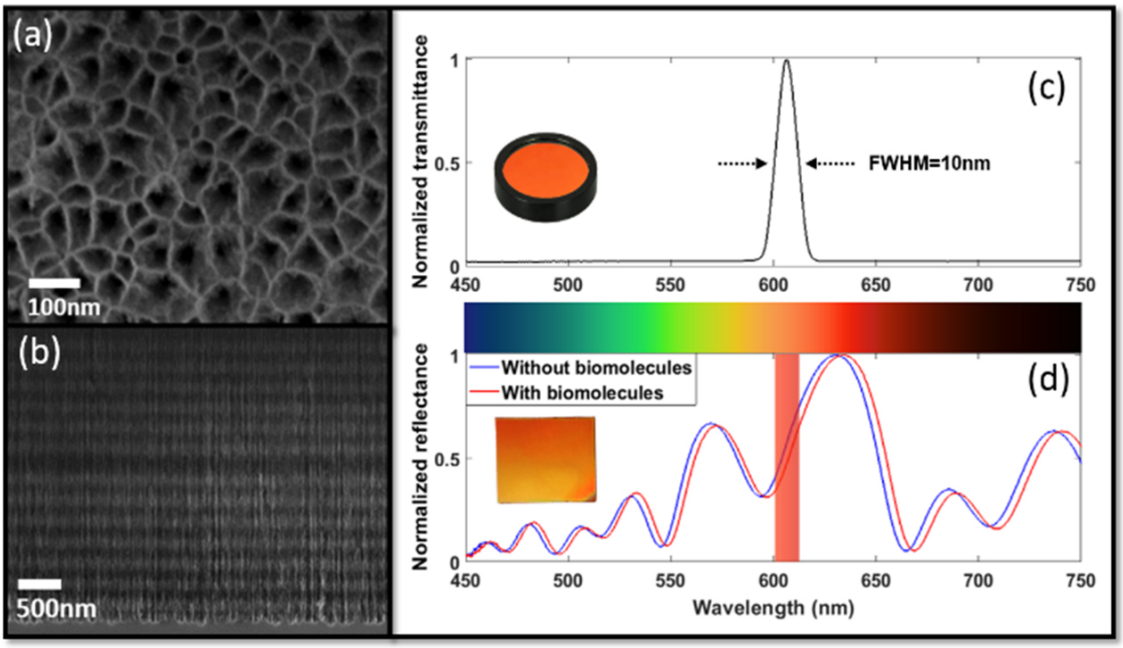

Figure 3.7: SEM images of PSiM in (a) top view and (b) cross-sectional view. (c) The normalized spectral intensity of the smartphone LED light after passing through the band-pass filter (shown in the inset), which is centered at 606.5 nm in this work. (d) Typical reflectance spectra of PSiM. The blue and red curves are the reflectance spectra before and after adding biomolecules, respectively. The red shaded region indicates the position of the filter. A photograph of a PSiM sample is shown in the inset.

the desktop computer in this work could also be carried out directly on the phone using an appropriately designed app or through a cloud computing approach.

Fabrication and surface modification of PSiMs

PSiMs were prepared by anodic etching of p-type silicon wafers in 15% HF in ethanol. Note that HF is an extremely dangerous chemical and should be handled with the utmost caution. First, a sacrificial layer was etched with a current density of 70 mA$\cdot$ cm^{-2} for 100 s and then dissolved in 1 M NaOH solution. The sample was then thoroughly cleaned with ethanol and DI water. Next, alternating current densities of 80 mA $\cdot$ cm^{-2} for 3.1 s and 60 mA$\cdot$ cm^{-2} for 3.2 s were applied in the following manner to form the optical microcavity structure: $(HL)^7(HH)(LH)^7$, where H and L designate the higher and lower current density, respectively, and the layers are designed to have an optical thickness corresponding to one

quarter of the resonance wavelength. Following anodization, freshly prepared PSiMs were modified by thermal hydrosilylation. 10-Undecenoic acid was added to a Schlenk flask and underwent three freeze-pump-thaw cycles in order to remove oxygen. Prior to the reaction, the sample was dipped into 2.5% HF solution for 90 seconds to remove the native oxide. The sample was then transferred to the Schlenk flask under a constant nitrogen flow. The flask was then immersed in an oil bath at 120°C and the reaction proceeded over 5 hours. Finally, the sample was rinsed thoroughly with tetrahydrofuran, dichloromethane and ethanol, and dried under a nitrogen stream.

APTES measurement for sensor benchmarking

To benchmark the performance of the PSiM-smartphone sensing system, we carried out an experiment to determine the relationship between spectral changes measured by an Ocean Optics spectrometer and colour changes measured by the smartphone camera (as described in the next section). A stepwise change in the refractive index of the PSiM was achieved by multiple exposures of the sample to a 0.1% (vv) solution of APTES in ethanol. For each exposure, 100 μL of the APTES solution was drop cast on the PSiM and incubated for 30 s, followed by gentle blowing with nitrogen gas to remove excess solution from the surface. The PSiM was measured with the spectrometer after each APTES exposure to quantify the spectral shift. The PSiM was then measured three times by the smartphone to quantify the colour change. APTES is a commonly used chemical for surface modification, which is known to form multilayer structures.[56] APTES attachment can therefore lead to large spectral shifts of the PSiM, which is necessary for the benchmarking of the sensor performance. We note that other molecules could have also been used and would have resulted in the same correlation between spectrometer and smartphone measurements for the given PSiM.

Biotin—streptavidin sensing

To achieve biotin functionalization, the hydrosilanized PSiM was first soaked in 1 mL 0.1

M NHS aqueous solution followed by 1 mL 0.4 M EDC. The reaction proceeded in a dark environment and gentle shaking was applied every 5 min. After 30 min, the sample was cleaned in DI water and rinsed in ethanol for 15 min. Next, the sample was soaked in 1 mg$\cdot$ mL^{-1} amine-PEG-Biotin solution for 30 min. Finally, an 80 μL aliquot of 0.5μm streptavidin mixed with 10 μL of ethanol was pipetted onto the PSiM sample and incubated for 60 min. The ethanol is added to reduce the surface tension between the water and hydrosilanized surface. The sample was then cleaned with DI water and ethanol three times, soaked in ethanol for 5 min and gently blown dry under nitrogen gas. After each step in the sensing experiment, the PSiM was measured with both the spectrometer and smartphone. The PSiM was subsequently exposed to 1 μm, 2 μm and 4 μm concentrations of streptavidin in water following the same procedures. We note that the magnitude of the change in the spectral and intensity responses of the PSiM sensor are dependent on the incubation time of the target molecule. Based on prior work,[68] we anticipate a measurable signal change could be achieved after a few minutes of exposure to the streptavidin solution; however, the magnitude of the signal change would be much less than what we report here for a 60 min exposure and would therefore also affect the limit of detection. To verify that there is no non-specific attachment of streptavidin on the PSiM, a control experiment was carried out. A 80 μL volume of 1μm sulfo-NHS-Biotin (1 mM) blocked streptavidin solution mixed with 10 μL ethanol was drop cast onto a biotinylated sample, incubated for 60 min, then rinsed with water and ethanol three times, and blown dry with nitrogen before measurement.

3.4.2 Results and discussion

Porous silicon microcavity characterization

Scanning electron microscopy (SEM) images of a PSiM are shown in Figure 3.7 (a, b). Based on image analysis, the estimated average pore size, porosity, and thickness of the

porous silicon layers fabricated with the higher current density are ∼60 nm, 82%, and 120 nm, respectively. The estimated average pore size, porosity, and thickness of the porous silicon layers fabricated with the lower current density are ∼40 nm, 75%, and 97 nm, respectively. A reflectance spectrum of the microcavity is shown in Figure 3.7(d). The resonance wavelength is near 600 nm and the peak of the high reflectance band on the long wavelength side of the resonance is near 630 nm. The refractive index sensitivity of the PSiM is determined to be near 350 nm/RIU as detailed in the appendix A.2. In this work, the most important design criterion is having a sharp spectral feature near the centre wavelength of the bandpass filter, as discussed in the next subsection.

Basic principle of smartphone biosensor

The smartphone is able to facilitate label-free optical biosensing with porous silicon by detecting the structural colour change of a PSiM upon a specific bio-recognition event. When molecules attach to the pore walls, the effective refractive index of the porous silicon increases and results in a redshift of the reflectance spectrum, as illustrated in Figure 3.7(d) for a PSiM. The rectangular shaded region represents the approximate spectral bandwidth of light that reaches the smartphone camera due to the presence of the bandpass filter. When molecules are added to the PSiM, the resulting spectral shift leads to a change in the integrated intensity of light measured by the smartphone camera. In Figure 3.7(d), with the bandpass filter designed to overlap with the long wavelength edge of the resonance of the PSiM, the addition of molecules leads to a decrease in the intensity of light measured by the smartphone since the intensity of reflected light at each wavelength within the measurement window decreases with molecular attachment. The steeper the reflectance spectrum is within the measurement window, the larger the change in light intensity measured by the smartphone camera will be for a given reflectance spectrum shift (i.e., given refractive index change of the PSiM due to molecular infiltration). Hence, other PSi thin film designs, such as edge filters, may lead to improved sensing performance compared to the PSiM. Nevertheless, in this work, the PSiM provides a convenient platform to compare smartphone and

spectrometer measurements while yielding good detection sensitivity. A comparison curve can be established that directly relates changes in spectral properties typically measured by a spectrometer with light intensity measured by the smartphone camera. This correlation is only necessary to benchmark the sensitivity of the smartphone detection platform in comparison to a traditional spectrometer. We note that the dynamic range of measurement using the smartphone detection platform, which is directly related to the maximum number or concentration of molecules that can be quantified by the smartphone detection platform, is limited by the wavelength range over which there is a monotonic change in reflectance intensity.

Engineering challenges with smartphonePSiM biosensor

There are several engineering challenges when assembling the system in the box that must be overcome to realize a robust biosensor that may be suitable for POC diagnostic applications. Although we only introduce the engineering challenges here, we believe sufficient process development would enable mitigation of the negative consequences of the current challenges.

First, the light emitted from the smartphone LED does not have uniform spatial intensity. Most of the light is concentrated in the center of the emission region, which can lead to saturation of the smartphone image sensors. As a simple approach to improve the illumination uniformity, we attached a piece of white paper to the outside of the smartphone LED to diffuse the emitted light, and we also used a piece of black scotch tape to block the region of highest intensity emitted light, as discussed in the smartphone measurements. More sophisticated light management approaches would be necessary to achieve a highly uniform intensity of incident light on the PSiM sample.

A second challenge is the nonuniformity of the porous silicon sample itself. Slight differences in the local thicknesses of the porous silicon layers comprising the PSiM lead to changes in the measured reflectance spectrum across the sample. For example, the micro-

cavity resonance wavelength, and likewise the high reflectance peak position, can vary by as much as 10 nm when different spots on the same PSiM sample are measured. Moreover, sample to sample variation in the shape and position of the reflectance band edge would introduce error into the quantification of the sensing measurements. Optimizing the electrochemical fabrication conditions, including control of the temperature and humidity conditions and electrode design, can lead to significantly improved porous silicon uniformity. Together, the nonuniform illumination and nonuniformity of the porous silicon can lead to significant changes in the measured light intensity by the smartphone camera when there is any change in the smartphone position with respect to the PSiM sample position. Figure A.3 in the appendix shows a typical smartphone camera image of the PSiM and the associated R-value contour map of the image, revealing that the R-value varies significantly across the PSiM.

Accordingly, a third engineering challenge is mechanical vibrations that cause displacement between the positions of the smartphone and PSiM sample, which lead to unwanted changes in measured light intensity that are not related to molecular binding. An improved 3D printed box design could enable the smartphone and PSiM sample to be fixed more robustly in place.

Moreover, in the current implementation of the PSiM-smartphone biosensor, the PSiM sample is removed from the 3D printed box each time a new molecule is exposed to the sample. The measured intensity variation caused by removing and reloading the sample is shown in appendix A.4. In future designs, improved methods of fluidic handling could eliminate the need to remove the sample from the box. In the present work, to mitigate error arising from smartphone-PSiM relative displacement, the area enclosed by a constant R-value contour curve is chosen to represent the effective light intensity value measured by the smartphone. This $R \geq R0$ criterion, where R0 = 30 in this work, automatically defines the boundaries of the analytical region under consideration and enables the best resilience

to mechanical vibration. The effective light intensity is calculated by summing the R values of the pixels within the area enclosed by the R = 30 contour curve. An average effective light intensity value is reported for each 1 min video measurement based on the average value calculated from approximately 500 images from the video. After each smartphone measurement of the PSiM, a bare silicon sample is measured as a control sample to account for any changes in the smartphone LED intensity over time. The average effective light intensity of the sample under test is normalized with respect to the average effective light intensity of the control sample, and is denoted as the relative intensity. In future work, the control sample could be measured at the same time as the test sample by imaging a region that contains both the PSiM and an unetched region of bare silicon.

Smartphone biosensor benchmarking with APTES infiltration

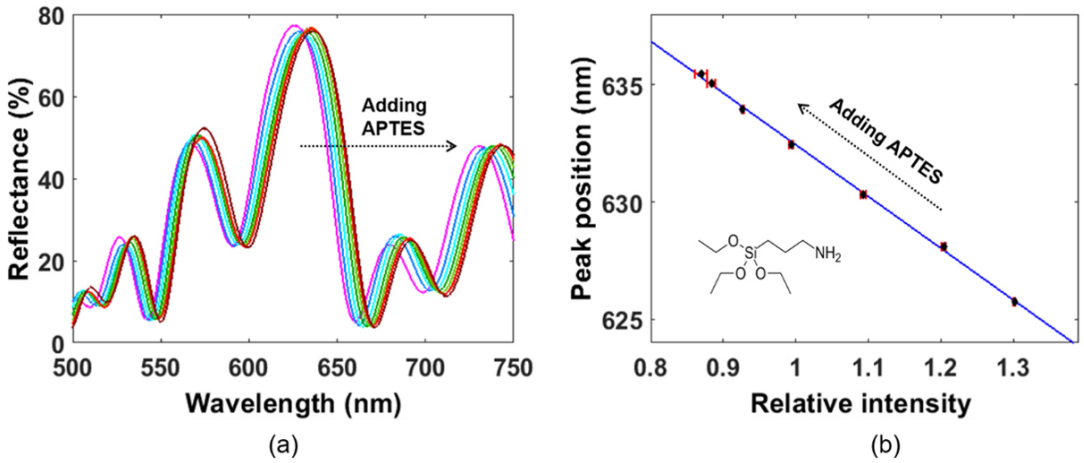

Figure 3.8: (a) Reflectance spectra of PSiM after adding 0.1% APTES solutions, as measured by a spectrometer. (b) Smartphone-spectrometer comparison curve that relates the longer wavelength peak position of the PSiM measured by the spectrometer and the relative intensity of light measured by the smartphone. The black diamonds are the experimental data points, the red bars show the $\pm 3\sigma$ value from the smartphone measurements, and the blue curve is a linear fit to the black data points. Inset shows the structural formula of APTES.

To benchmark the performance of the smartphone biosensor with a traditional spectrometer, a PSiM was exposed to 0.1% APTES in ethanol and subsequently blown dry and

measured by both the smartphone and spectrometer. As shown in Figure 3.8(a), the reflectance spectrum measured by the spectrometer redshifts after each successive exposure to the APTES solution that infiltrates the pores of the PSiM. Correspondingly, the relative intensity measured by the smartphone decreases when the spectrum redshifts due to the relative spectral positions of the bandpass filter and resonance. Figure 3.8(b) shows the correlation between the peak wavelength measured by the spectrometer (i.e., the peak on the longer wavelength side of the microcavity resonance) and the relative intensity measured by the smartphone. A linear curve is used to fit the data with R2 = 0.999. The error bars in the relative intensity measurements represent $\pm 3\sigma$, where σ is the standard deviation of the three relative intensity measurements taken for each APTES infiltration (details provided in A.1 in appendix). The root-mean-square deviation (RMSD) of the data points from the linear fit is used to estimate the accuracy of the PSiM-smartphone sensor. As detailed in A.5 in appendix, the RMSD = 0.11 nm, and we consider the equivalent accuracy of the smartphone measurements to be three times the RMSD (i.e., 0.33 nm). The Bland-Altman analysis shown in appendix Figure A.5, provides further confirmation of the agreement between the smartphone and spectrometer measurements. Therefore, based on the measurements and analysis, we suggest that the PSi-smartphone sensor system could distinguish a relative intensity change that is equivalent to a microcavity spectral shift of 0.33 nm.

Biotin—Streptavidin sensing

To evaluate the biosensing performance of the PSiM-smartphone system, a biotin-streptavidin sensing assay was carried out. For this experiment, only the smartphone is required, but spectrometer measurements were also taken to provide further insights. Figure 3.9 shows the relative intensity of light measured by the smartphone as different concentrations of streptavidin molecules were exposed to the biotinylated PSiM. As expected, the relative intensity decreases with increasing streptavidin concentration. We note that the change in

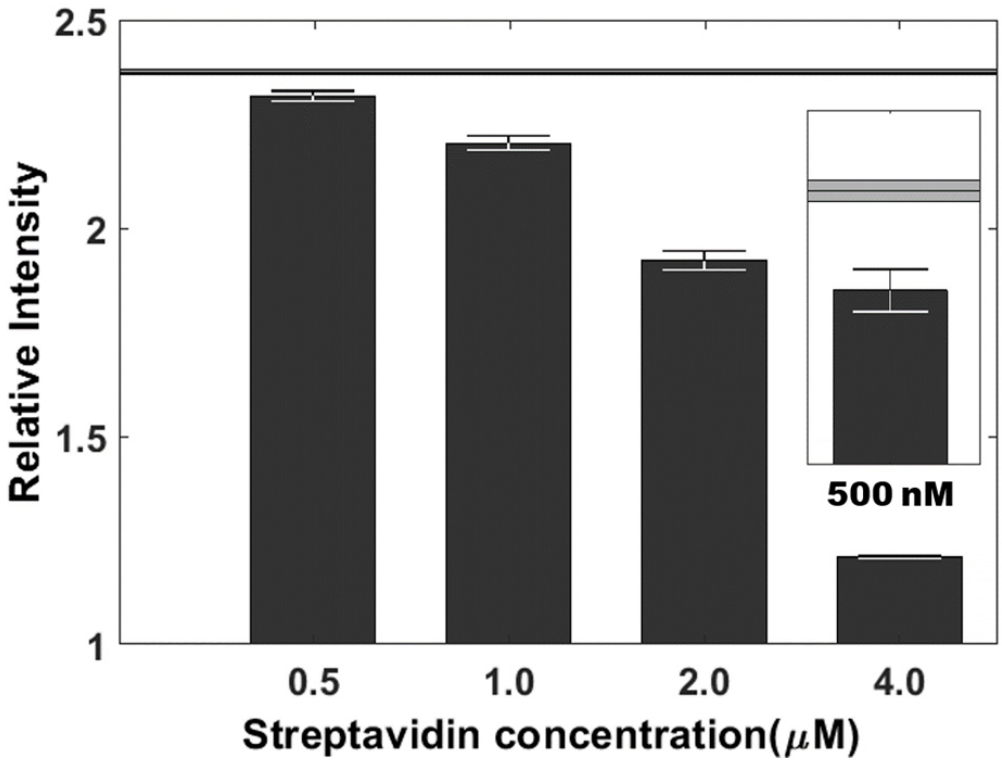

Figure 3.9: Relative intensity measured by smartphone when different concentrations of streptavidin are exposed to a biotin-functionalized PSiM. The detection limit is near 500 nM. Error bars represent $\pm 3\sigma$.

relative intensity with respect to the streptavidin concentration is not linear across the data set because the measurements span a nonlinear region of the slope of the microcavity resonance that is probed through the bandpass filter. Figure A.6 in appendix, which shows the peak wavelength shift measured by the spectrometer as a function of streptavidin concentration, does suggest that the PSiM is being measured within the linear regime of a dose-response curve. Moreover, Figure A.6 reveals that there is minor instability of the surface functionalization of the PSiM that manifests as a slight blueshift in the spectrum when the sample is exposed to a 0 nM concentration of streptavidin (i.e., no streptavidin molecules and only solvent exposed to the sample). The biotin-streptavidin assay was repeated on three additional PSiM samples to confirm the general trend of the relative intensity measured by the smartphone upon exposure to the different streptavidin concentrations

(appendix Figure A.7). In all cases, the relative light intensity measured by the smartphone when the PSiM is exposed to 500 nM streptavidin is statistically different from the initial relative light intensity value measured before exposure to any streptavidin solutions (solid line shown in Figure 3.9 and Figure A.7). Therefore, a detection limit near 500 nM for the streptavidin molecules is estimated for the PSiM-smartphone biosensor. In order to verify that streptavidin molecules are captured selectively by biotin receptor molecules attached to the PSiM, a control experiment was carried out in which sulfo-NHS-biotin blocked streptavidin molecules were exposed to an amine-PEG-biotinylated PSiM, as described in Section 2. A blueshift was measured by the spectrometer, which we again attribute to instability of the PSiM surface modification. This result suggests that biotin-streptavidin binding occurs specifically and, moreover, improvement in the robustness of the surface chemistry may allow even larger changes in relatively intensity to be measured when a given concentration of streptavidin is exposed to a biotin-functionalized PSiM.

3.4.3 Conclusions

A PSi-based smartphone biosensor is demonstrated as a new sensing platform that leverages the convenience of a smartphone and the high internal active sensing surface area of a PSi film. Structural colour changes of the PSi film that result from molecules infiltrating the pores are converted to a relative intensity value by analysing the red pixel values read out from the smartphone camera image sensor. When benchmarked against a commercial spectrometer, the PSiM smartphone system exhibits an accuracy equivalent to 0.33 nm. Specific detection of streptavidin molecules was demonstrated with an estimated detection limit of 500 nM. As the PSiM biosensor supports a variety of surface functionalizations, the PSiM smartphone system could be used as a platform for the detection of a multitude of chemical and biomolecular species including DNA, small proteins, and toxins using, for example, DNA, antibody, or aptamer probes. By addressing some of the current engi-

neering challenges and by integrating a simpler fluidic handling approach, the PSi-based smartphone biosensor has the potential for application as a POC diagnostic tool, which could be particularly useful in low-resource environments.

3.5 Possible improvements

A solid box or housing can provide the support for the sensing platform and shield for the ambient light. However, it is inconvenient to carry a box several times larger than the smartphone itself. One way to replace the box is to do the background subtraction and calibration in real time. A recent paper proposed a biosensor using the principle of lock-in amplifier, a method which has been widely used in the field of electronics and the usability of which has also been demonstrated in smartphone sensing systems.[69] We find it might be useful to include the techniques to the PSi smartphone biosensors as well. As for using multi-color channels of the smartphone cameras, Ryckman et al reported a hyperchromatic structural color-based colorimetric sensor recently, which explored the interplay between the structural color filter design and the choice of illuminant.[70] The paper demonstrated a minimum resolvable difference of 0.1nm (with naked eye as detector) under the illumination of three monochromatic lasers, which is 30 times lower than single-wavelength sensors. We note that the enhancement was not unique to the laser systems, and the combination of porous silicon filters and smartphone LED could also be used to achieve the same enhancement.

CHAPTER 4

Peptide-based biosensing

Notes to readers : Part of the chapter was adapted with permission from my previous publication:

Tengfei Cao, Rabeb Layouni, Matthew B. Coppock, Paul E. Laibinis, Sharon M. Weiss, "*Use of peptide capture agents in porous silicon biosensors*," Proc. SPIE 11258, Frontiers in Biological Detection: From Nanosensors to Systems XII, 112580L (21 February 2020); https://doi.org/10.1117/12.2552932[71]

4.1 Introduction

Biorecognition elements (bioreceptors) are at the heart of the modern biosensors. Biorecognition elements specifically recognize the analyte and separate the target molecules (signal) from the complex analyte solution through physical adsorption, chemical binding or catalysis. The most widely used receptors for biorecognition are the enzymes and antibodies, which are served as the biorecognition elements for catalytic biosensors and affinity biosensors, respectively.[72] Since the first introduction as the glucose biosensor by Clark and Lyon in 1962, enzymes-based biosensors have developed rapidly.[73] The enzyme's recognition is realized by (1) converting the analyte into a sensor-detectable product; (2) serving as the catalysis for a reaction that can be inhibited or activated by the analyte. Generally, enzymes that are capable of recognizing analytes are efficient biocatalysts, such as redox enzyme, peroxidase and urease. Despite great success, the development of enzyme-based sensors also faces several challenges. For instance, searching for a new highly efficient and active enzyme is difficult and costly.[74] Most enzymes-based biosensors suffer from poor stability, and require critical operation temperature and pH conditions. The first antibody-

based biosensor (immunobiosensor) was reported in 1970s.[75] Antibody biosensors recognize analyte through specific binding of antibody and antigen. For antibody biosensors, monoclonal antibodies (MAb) are the current golden standard. MAb has a high affinity and an excellent selectivity.[76] But the poor in-vitro adaptability, manufacturability, and stability for transportation and storage greatly restrict its applications, especially for the point of care (POC) applications.[77] To address some of these challenges, mAb alternative technologies have been developed such as DNA (RNA) aptamers,[78] single domain antibodies,[79] post-modified antibodies[80] and peptide nucleic acids (PNAs).[81] However, none of these technologies have yet fulfilled all of the necessary reagent requirements for fieldable sensors. Peptides, the short chain of amino acids and the building blocks of protein, has emerged as a promising antibody alternative for POC testing in recent years. Although, they are much smaller in size compared to the MAb, the peptides (or their derivatives) can show comparable affinity and selectivity for certain targets. Like protein antibodies, the peptides have the advantage of mature screening protocols, diverse structures and large chemical versatility. Beyond protein antibodies, the peptides have the technologies for on-demand selection and synthesis, great thermal stability, and good adaptability to various platforms through chemical modifications.[76] Besides the function as the bioreceptor, peptide sequences have also been demonstrated to show selective affinity to the semiconductor surfaces, one of the major transducer materials for biosensors.[82, 83] In this chapter, we start with the basics of the peptide, the amino acid monomers, the common preparation and selection methods, and then review the techniques and relevant works to peptide biosensing. In the main text, we will report the experiments on the peptide based biosensing being done in our lab and future plans involving the robustness and affinity of the peptide capturing agents, the diffusion and binding kinetics of associated target molecules to the peptide functionalized surface compared to nanostructured surfaces with other functionalization. We believe that understanding the nano-bio interface with peptide-functionalization in PSi can provide critical insights that could be applied to other types of nanostructured surfaces

Name	Basic Structure	Glycine	Alamine	Isoleucine	Leucine	Methionine	Valine
Abbrev.	AA	Gly / G	Ala / A	Ile / I	Leu / L	Met / M	Val / V
Structure	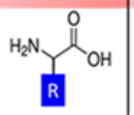	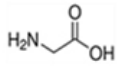	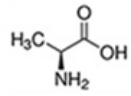	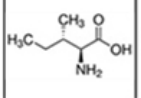	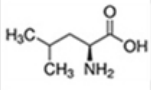	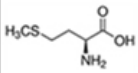	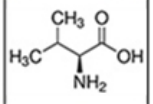
Name	Phenylalanine	Tryptophan	Tyrosine	Asparagine	Cysteine	Glutamine	Serine
Abbrev.	Phe / F	Trp / W	Tyr / Y	Asn / N	Cys / C	Gln / Q	Ser / S
Structure	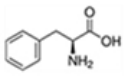	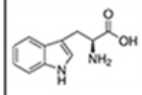	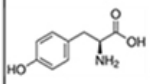	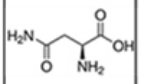	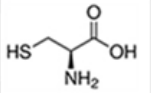	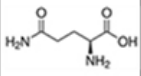	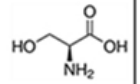
Name	Arginine	Aspartic acid	Glutamic acid	Proline	Histidine	Lysine	Threonine
Abbrev.	Arg / R	Asp / D	Glu / E	Pro / P	His / H	Lys / K	Thr / T
Structure	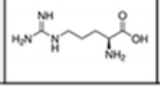	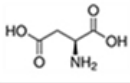	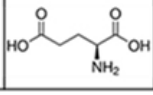	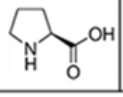	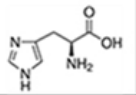	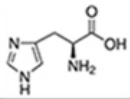	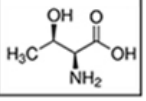

Table 4.1: The 20 kinds of naturally occurred amino acids—the names, three- letter/ one-letter abbreviations and chemical structures.

and could enable improved performance across multiple sensing technologies.

4.2 Basics of peptide

Peptide is the short chain of amino acids, which is closely related to protein. There are 20 kinds of naturally- occurring amino acids, listed in Table 4. 1. The general structure of the amino acid (AA) is the amine and the carboxylic acid groups attaching to the same carbon with a side chain (R group) and a hydrogen atom. In terms of electronic structures, Lys, Arg and His are positively charged; Asp and Glu are negatively charged; Ser, Thr, Cys, Tyr, Asn and Gln are polar; Gly, Ala, Val, Leu, Ile, Met, Phe, Trp and Pro are nonpolar. When the amine of one AA reacts with the carboxyl group of the other AA, a peptide bond is formed. The peptide bond is so stable that it has a room temperature half-life time of 350 to 600 years.[84] Connected by the peptide bond, 20 kinds of amino acids can form infinite number of peptides. Peptides are distinguished from proteins based on the number of isomers, and generally the chains that have 50 or fewer amino acids are referred to

as peptides, but the classification is not absolute. Peptides have significant applications in molecular biology.[85, 86] They allow the creation of peptide antibodies in animals without the need for purifying the protein of interest. It can act as the probe to reveal the peptide-protein interactions and it also has the potential to treat disease including cancer.

4.3 Peptide preparation

In the natural environment, peptide is synthesized in the ribosome via genetic translation, a process that ribosomes link AAs together in the order specified by messenger RNA (mRNA) molecules.[87] In the messenger RNA sequence, three nucleic acids (one codon) corresponding to one AA. 64 codons map to the 20 amino acids and the start/stop codon. The degeneracy gives the synthesis tolerance to the gene mutation. In the laboratory, the most well-known method for short chain peptides synthesis is solid-phase peptide synthesis (SPPS).[88] As for peptide selection and screening, display technologies are the most common methods, where phages and bacteria are used to produce libraries of peptides.[89, 90] Phages and bacteria, carrying the mutated genes, can generate a great diversity of peptides categories in the process.

4.3.1 Solid-phase peptide synthesis

SPPS allows the rapid assembly of a peptide chain through successive reactions of amino acid derivatives on the insoluble porous support, which consists of small, polymeric resin beads functionalized with reactive groups (such as amine or hydroxyl groups) that link to the initial peptide chain. Since the peptide remains covalently attached to the support throughout the synthesis, excessive reagents and side products can be removed by washing and filtration. Compared to the solution-phase synthesis, SPPS avoids the comparatively time-consuming isolation of the product peptide from solution after each reaction step. The procedure of the SPPS is listed as follows. (Schematic is shown in Figure 4.1)

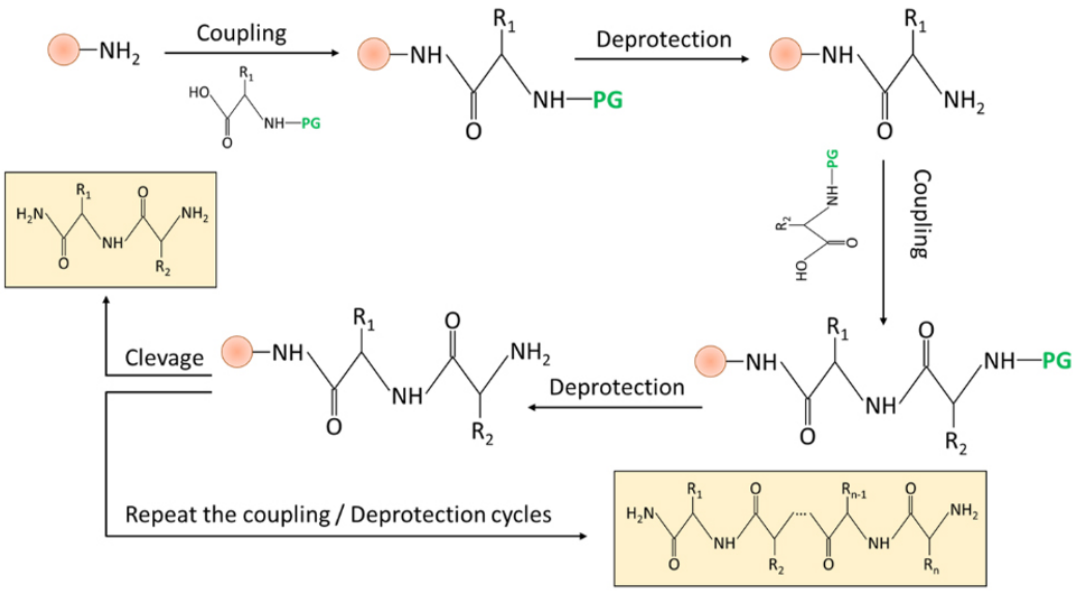

Figure 4.1: The procedure of solid phase peptide synthesis flow. The red dots are the resin beads. The green 'PG' stands for the protecting group. R_1 and R_2 are the R groups of the amino acids.

First, the -NH_2, ammine group (or -COOH, carboxy group) modified resin beads are dispersed on a solid-state porous support. N terminal protected AAs are introduced to the resin, and the peptide bonds are formed between the resin beads and the AAs after the condensation reaction. Then deprotection is applied and a new ammine termination is formed at the end of the peptides. The next step is to introduce a new AA unit and repeat the coupling and deprotection steps until all the desired AAs are integrated. Finally, the crude peptide is cleaved from the solid support while all protecting groups are removed simultaneously using a reagent strong acid, like trifluoroacetic acid or a nucleophile. The crude peptides can be further purified by using reversed-phase high performance liquid chromatography (HPLC).

4.3.2 Phage display

Though a known peptide sequence can be precisely synthesized by SPPS, a much greater

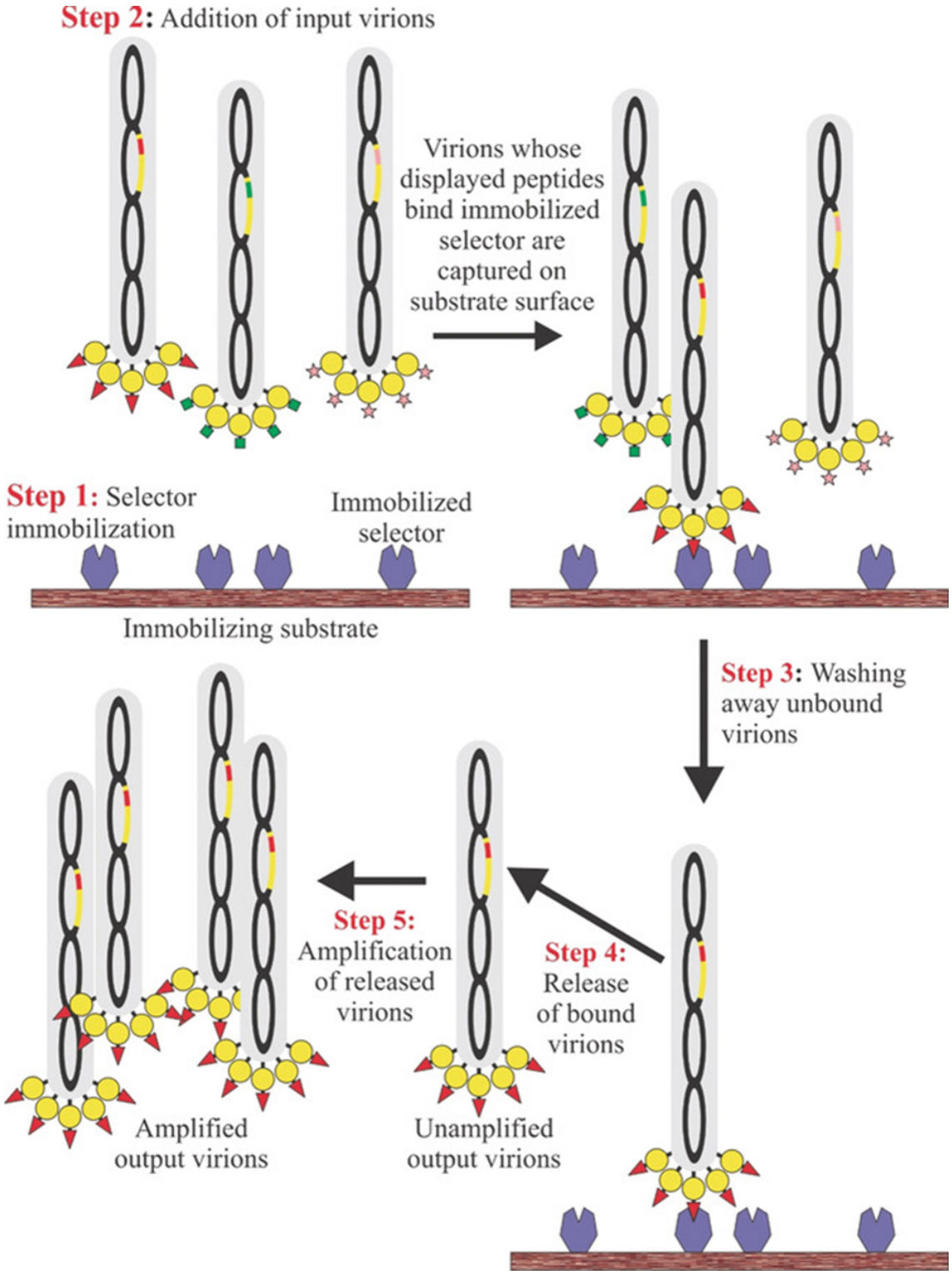

Figure 4.2: Schematic diagram of affinity selection. Steps are detailed in the text. The figure is adapted with permission from Ref [91], Copyright 2019 Wiley-VCH Verlag GmbH & Co. KGaA, Weinheim

diversity of peptides library is needed to find the peptides that binds to specific protein, small molecules or inorganic surface. The generation and multiplication process of these libraries are called a display. First reported by George Smith in 1985, Phage display is a 2018 Nobel Prize winning technology for peptide selection.[91] Phage display is a process that starts with inserting foreign DNA fragments into the DNA of a bacteriophage—a virus that infects bacteria. That gene of the foreign DNA is then expressed and displayed on the surface of the phage (coat protein).[92] Researchers can use these protein-displaying phages to screen for peptides that have high affinity to certain proteins, DNA sequences, and small organic or inorganic molecules, or even specific surfaces. Bio panning (affinity selection) with phage display peptide library is the most popular method for peptide selection. As shown in Figure 4.2, the affinity selection contains the following steps.[91]

Step 1, target molecule (also called selector) is immobilized onto a solid surface, such as polystyrene petri dish or microplate well. Step 2, many foreign genetic sequences are inserted into a bacteriophage library in the form of fusions with the bacteriophage coat protein. Alongside with other phage genes expression, these genes expressed and displayed on the surface of the viral particle. The phages whose displayed peptides bind the immobilized selector are captured. Step 3, the phages whose displayed peptides bind do not bind or have poor affinity to the selectors are washed away. Step 4, the bounded phage is eluted from the microtiter plate and (Step 5) amplified by infection of suitable bacterial hosts. The new phage constitutes an enriched mixture, containing considerably less irrelevant phages (i.e. non-binding) than were present in the initial mixture. The bind-wash-elute-amplify steps were repeated until the purification of the desired peptide reached the acceptable level. The common phages used for display include fd filamentous phage, M-13, T4, T7, and λ phage.

4.3.3 Bacteria display

Similar to phage display, bacteria and yeast display are also important technologies for

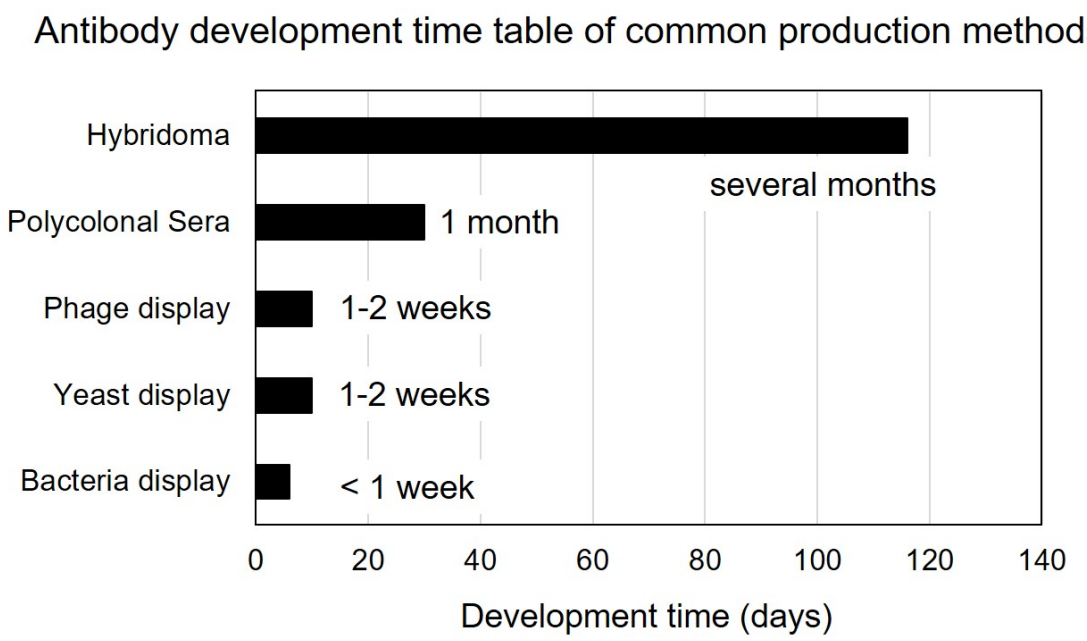

Figure 4.3: The antibody development time table of common production methods. Reproduced from Ref [93] under the terms of the Creative Commons Attribution-NonCommercial-ShareAlike-3.0 License, Copyright Dimitra N. Stratis-Cullum et al. Licensee IntechOpen.

peptides discovery. It is reported that peptides, identified and affinity selected by using bacterial display, were remarkably similar to the best affinity matured using phage display and exhibited comparable dissociation constants.[76] Fast screening of bacterial-displayed peptide libraries is enabled by using cytometry enabled optimization method, like fluorescence activated cell-sorting (FACS) and/or magnetic activated cell sorting. Comparing other antibody preparing techniques (the comparison chart is shown in Figure 4.3), bacteria display also features the shortest developing time.[93] Bacterial display thus provides a new quantitative tool for the discovery and evolutionary optimization of protein-specific peptide ligands.

4.4 Peptide as the bioreceptors

As mentioned in the introduction, the protein-based antibody-antigen assay is the current standard approach to detect the biomolecules and bio interactions for affinity biosensors. However, the environmental stability issue and the long developing period significantly boost the cost and reduce the convenience. On the other hand, peptides share the same chemical building blocks and bonding with proteins, while having much better stability and thus are an ideal substitute for protein as the biorecognition element. Over the years, peptide-based molecular biosensors have been developed for convenient and fast detection of various analytes including proteins,[94] DNA,[95] metallic ions[96] and toxins.[97] Generally, peptide binding does not generate directly observable signals, and transducers are needed to transform the binding events to measurable quantities, like color change, spectra shift, light emission, potential change or direct current, etc.[98] The most common way to achieve the transduction is to attach the peptides with signal makers, i.e. labelling. There are only a limited number of label-free peptide sensors being reported.

Fluorescent labelling is the most widely used technique for peptide-based biosensors.[99] Spectral properties of the fluorophores used for peptide labelling are highly sensitive to the surrounding environment. The mechanisms for signal transduction include fluorescent resonance energy transfer (FRET), excimers and probe-quench pair or simply structure change induced light enhancement.[100] The FRET peptide biosensors are made of a sequence of peptides used for specific binding and a light emitting donor-acceptor pair. Upon recognition, the target analyte binds to the peptides and changes the distance between the donor and acceptor, thus affecting the energy transfer from between the two. For example, Joshi et al reported a peptide Hg^{2+} ions sensor based on FRET. In the system, peptide-Hg^{2+} binding shortens the distance between tryptophan (donor) and dansyl fluorophore (acceptor) and increases the energy transfer, resulting in higher fluorescent emission intensity.[101] The FRET process could also be induced by protease cleavage of peptides as reported by Kaman

et al.[102] Excimer based biosensors are made of a sequence of specific peptides and two identical fluorophores linked to each end of the sequence. Based on the observation that flexible and dynamic short peptides become rigid when conjugated with macromolecular targets, which could segregate two pyrene moieties and inhibit excimer formation, Plaxco et al have produced the peptide beacons based biosensor directed against both anti-HIV antibodies and the retroviral transactive response (TAR) RNA hairpin[103]. The analyte binding could lead to 2-fold decreases in excimer emission and achieve nanomolar level detection limit. Compared to FRET, probe-quencher pair is usually based on static quenching where molecules form non-fluorescent complexes in the ground state but stay fluorescent at the excited state. For example, Qing et al reported a graphene oxide (GO) based fluorescent biosensor that employs the probe-quencher pair strategy[104]. In the ground state, binding of fluorescein isothiocyanate (FITC)-labeled octreotide (FOC) to GO results in significant fluorescence quenching of FITC. But upon specific binding of the anti-octreotide (AOC), FOC is released from the GO surface and recovers the fluorescence. A detection limit of the AOC can reach 2ng/mL based on the above principle.

Labelling has helped the peptide sensing achieve low detection limits and high sensitivity, but label-free biosensing is generally more favorable, considering the ease of sample preparation and nature- environment molecular interactions. With the PSi rugate filter as the transducer, Gooding et al reported a label-free peptide sensor by tracking the optical spectral shift of the PSi reflectance spectra, which could detect the protease down to 37 nM.[105] Sam et al reported a electrochemical heavy metal ion sensor based on peptides modified porous silicon surface[106]. Combining the high affinity and good stability of peptides and the easy preparation and low cost of the label-free method, more work should be done in this promising field.

4.5 Peptide for surface modification

Surface modification is the crucial step for analyte binding. A stable transducer surface is a necessary condition for the reliable signal and the subsequent success of sensing. Surface modification protects the transducer surface and provides the chemical bonds for further receptor binding. Pristine PSi is very unstable, and it dissolves slowly even in water or pH neutral buffer. A natural way to passivate the PSi surface is oxidation, which changes the Si-H and Si-Si bond to Si-O bond. The methods for oxidation include thermal oxidation, ozone plasma and chemical methods (hydrogen peroxide oxidation). Oxidized PSi shows improved resistance to aqueous corrosion. Higher degree of oxidation offers better protection, but leads to poorer optical properties and lower refractive index of the PSi. Moreover, oxidized PSi is still vulnerable to basic solutions. Another way to passivate the PSi is thermal carbonization, which adds Si-C to the PSi that can withstand the basic solutions, but the carbon lowers the intensity of the reflection and degrades the optical performance as well. After oxidation or thermal carbonization, a secondary modification is still needed to create the bonds for organic molecules. Silanization, for example, adds ammine group to the surface, but the process is either too time consuming or unstable. Based on the fact that short peptides that can specifically recognize inorganic materials, Gergely et al reported a new method to functionalize the PSi with peptide.[83] Peptides with specific affinity to the PSi surface is screened via phage display and then labelled with biotin. The peptide functionalized PSi can achieve a lowest detection limit (LOD) up to 21 times lower than the LOD obtained with the silanized devices.

4.6 Peptide attachment through click chemistry

To construct a peptide-based biosensor, the most important step of the experiment is to attach peptide-based capture agents on the PSi surface. Three methods illustrated in Figure 4.4 have been taken into consideration. (1) Incubating silane functionalized capture

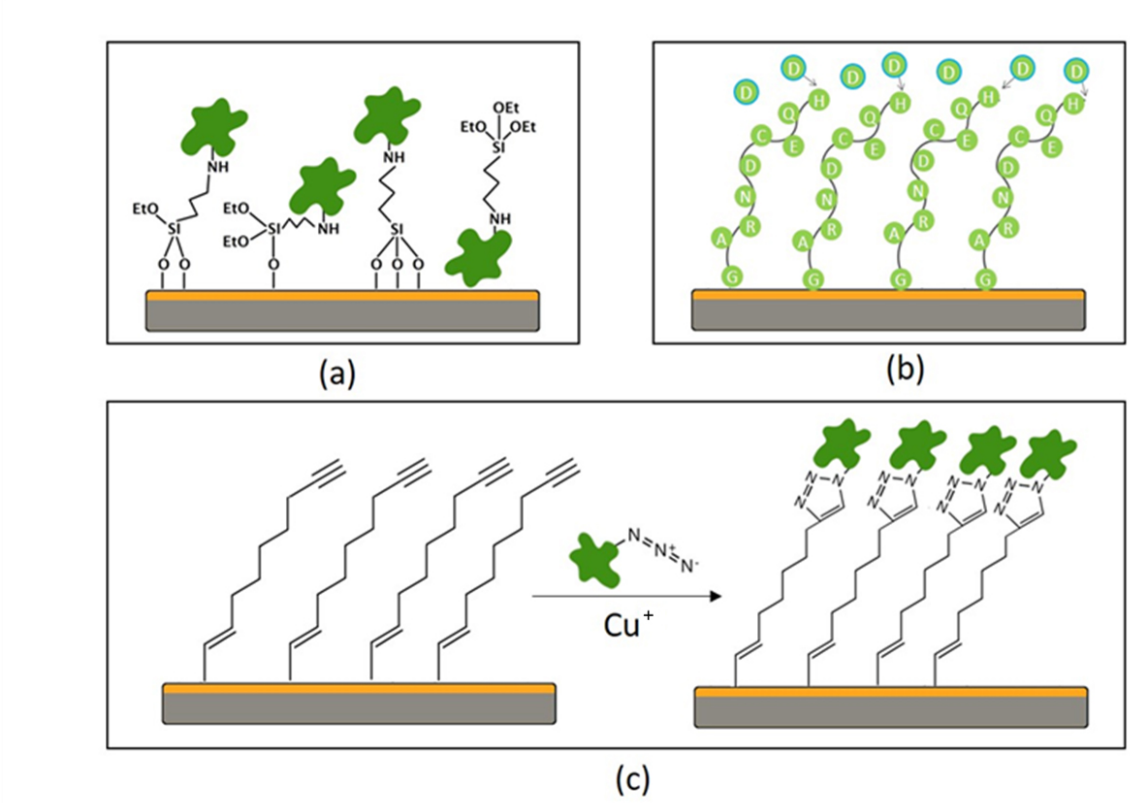

Figure 4.4: Three possible methods for binding peptides: (a) The silane functionalized peptides binding to PSi surface. (b) Direct peptide synthesis on PSi. (c) Peptide conjugation through azide-alkyne cycloaddition-based click chemistry.

molecules with silicon substrate. (2) Direct peptide synthesis on PSi. (3) Azide-alkyne cycloaddition-based click chemistry. To determine the best functionalization protocol, biotin/peptide streptavidin model is used. Silane (APTES) biotin capture protocol has been demonstrated in our group,[107] but the silane modified surface has a poor resistance to water corrosion.[108] The instability of APTES-PSi will shadow the signal of peptide-analyte binding and complicate the stability study of the peptides. Direct peptide synthesis on PSi seems promising due to good stability. However, additional efforts to sort are needed in the process which adds to complexity. So, click chemistry is utilized to attach biotin and the streptavidin binding peptide (SBP) to the PSi samples,[71] and the unique azide-alkyne reaction allows alkyne modified PSi surface to incorporate most peptide sequences without side reactions. The SBP was provided by our collaborators at Army Research Laboratory

(ARL).

4.6.1 PSi structure preparation and hydrosilylation

PSi microcavities are fabricated through anodic etching of p-type silicon wafers in a solution of 15% ethanoic HF solution (as specified earlier). **Note that HF is an extremely dangerous chemical and should always be handled with the utmost caution**. To ensure there is no narrowing of the pore opening at the top surface of the wafer,[24] an etching current density of 70 $mA{\cdot}cm^{-2}$ is applied to the wafer for 100s to serve as a sacrificial layer and it is then dissolved in 1 M NaOH solution and rinsed with ethanol and DI water. Next, the PSi microcavity is etched using a pair of alternating current densities of 80 $mA{\cdot}cm^{-2}$ (H) for 3.1 s and 60 $mA{\cdot}cm^{-2}$ (L) for 3.2 s, arranged in the order of $(HL)^7(H)^2(LH)^7$. The freshly etched PSi microcavity is then modified with a 10-carbon straight-line alkyne, 1,8-nonadiyne, through thermal hydrosilylation. Before hydrosilylation, as-purchased 1,8-nonadiyne is purified by liquid chromatography to remove the oxides. Silica powder is used as the stationary phase and hexane is used as the mobile phase. Following purification, the nonadiyne solution undergoes three freeze-pump-thaw cycles to remove oxygen. PSi sample is dipped into 2.5% HF solution for 90 s to remove native oxide before dipping into the nonadiyne solution, and then washed with DI water and ethanol, and dried with nitrogen gas. Following the cleaning process, the PSi sample is immediately placed in a Schlenk flask with the degassed 1,8-nonadiyne. The hydrosilylation reaction lasts over 3 h in an oil bath at the temperature around 155 °C. The PSi sample is removed from the flask, rinsed thoroughly with dichloromethane (DCM) and ethanol, and then dried under a nitrogen stream. FTIR spectroscopy measurements are carried out to confirm alkyne presence on the PSi surface.

4.6.2 Bioreceptor immobilization through click chemistry

Copper (I)-catalyzed Click chemistry was performed to attach the azide-modified biotin and SBP to the alkyne-modified PSi surface. Freshly prepared sodium ascorbate (20 mM in water) was added to copper (II) sulfate pentahydrate (0.40 mM in water) in a volume ratio of 1:1. The reduced copper solution was then mixed with the bioreceptor solution (azide-modified biotin 8.67 mM, in ethanol/water 1:1 or azide-modified SBP, AWRHPQGG 6 mM, in ethanol/water 1:1) in a volume ratio of 2:3. Then 25 μL solution of the mixture was drop-cast on the PSi and stored in sealed dark environment with liquid ethanol and water sprayed inside to mitigate evaporation of solvents. Different reaction times for this click reaction were evaluated at room temperature: 6, 12, 24, and 48 h. After reaction, the samples were rinsed with anhydrous ethanol and DI water, and soaked in 0.5 mM HCl for 30 min to remove residual copper in the pores. The samples were then cleaned with DI water and anhydrous ethanol, and dried under a stream of nitrogen gas. FTIR spectroscopy measurements are carried out to confirm the attachment of the bioreceptors.

4.6.3 Streptavidin sensing experiment

The functionality of SBP and biotin was evaluated through exposing the functionalized PSi samples to streptavidin molecules for various reaction times. A 20 μL of 5 μM streptavidin was drop cast onto each of three SBP-modified PSi samples and incubated for 1, 2, and 17 h, respectively, at room temperature. In addition, a 20 μL volume of 5 μM streptavidin was drop cast on a nonadiyne-modified PSi microcavity (without peptide), as a control experiment and a 20 μL volume of 5 μM streptavidin was drop cast on a biotin-modified PSi microcavity to compare the performance of the SBP with biotin; the streptavidin molecules were exposed to each of these samples for 1 h. Following the specified incubation time in streptavidin, all PSi samples were washed thoroughly with DI water, dried under a stream of nitrogen, and measured with both optical reflectance spectrometry and FTIR spectroscopy.

4.6.4 PSi microcavity characterization and functionalization confirmation

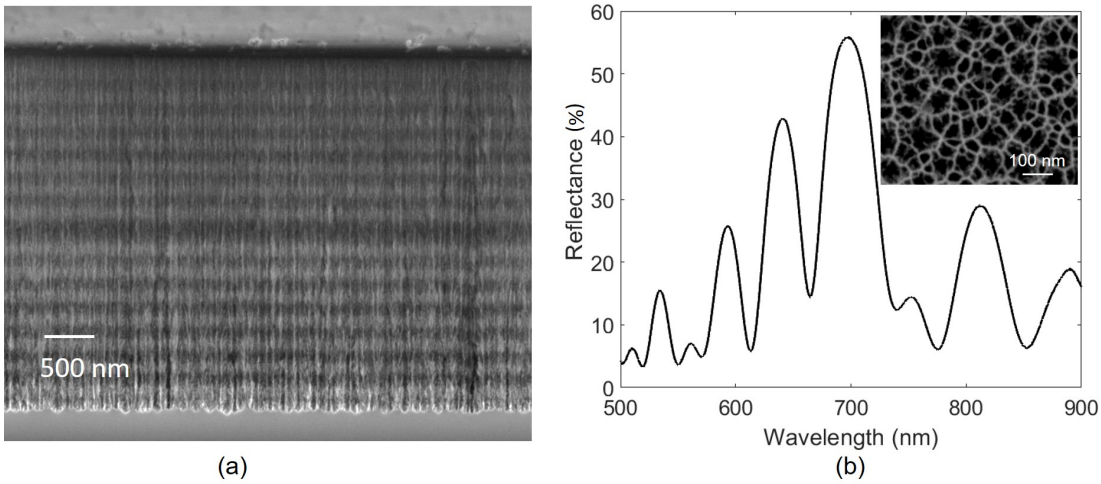

Figure 4.5: (a) Cross-sectional SEM image of porous silicon microcavity. (b) Reflectance spectrum of PSi microcavity with a resonance wavelength near 660 nm. (Inset) Top-view SEM image of PSi.

Figure 4.5 (a) shows the cross-sectional SEM image of a PSi microcavity. The top and bottom Bragg stacks consist of the alternating higher and lower porosity layers sandwiching the higher porosity thicker middle cavity layer, as can be seen in the image. The inset of Figure 4.5(b) displays the top-view of PSi sample (SEM image). Calculated from the image analysis, the PSi formed by applying higher and lower current densities during electrochemical etching have average pore diameters of around 60 nm (82% porosity) and 40 nm (75% porosity), respectively. The total thickness of the PSi microcavity is approximately 3.3 μm. Figure 4.5(b) is a typical reflectance spectrum of a PSi microcavity, and the center resonance wavelength locates near 665 nm.

The 1,8 nanodyine (ND) functionalization is confirmed by FTIR spectra as shown in Figure 4.6. The top black curve is the spectrum taken after etching. The peaks near 900 cm^{-1} and 2100 cm^{-1} indicate the Si-H bonds. The middle blue curve is taken after hydrosilylation. The tiny peak near 900 cm^{-1} and the absence of the peak near 900 cm^{-1} indicate a good alkyne coverage on top of the PSi surface. The green curve is the spectrum taken after the click chemistry. The binding of SBP is validated by decrease of the

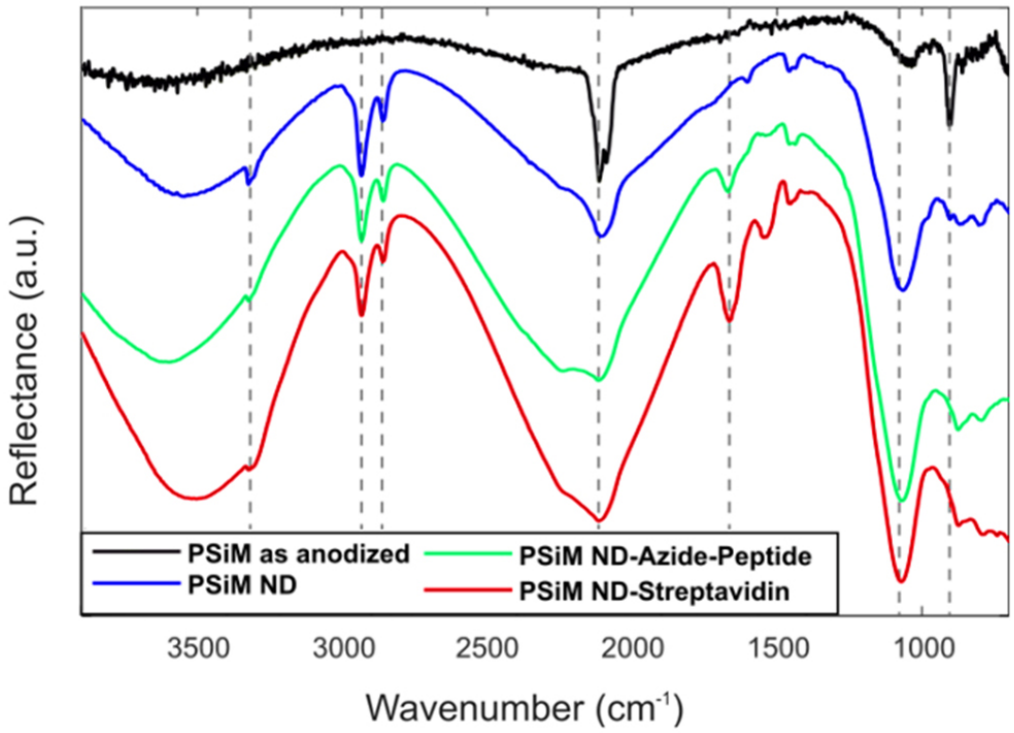

Figure 4.6: The FTIR spectra of PSi microcavity at different stages of the experiment, i.e. as-anodized, after nonadiyne modification (ND), after the click reaction with azide-functionalized streptavidin-binding peptide (ND-Azide-Peptide), and after the capture of streptavidin molecules (ND-Streptavidin). Notable bonds are indicated with the dashed lines.

peak intensity at 3300cm^{-1}, which relates to the consumption of alkyne groups during the click reaction. And the amide bands near 1650 cm^{-1} and 1540 cm^{-1} are also consistent with the peptide structure. The binding of the SBP could also be confirmed by the redshift of the reflectance spectrum as shown in Figure 4.7(a). Following a 1 h exposure of the SBP functionalized PSi microcavity to 5 μM streptavidin solution, there is an increase in the intensity of the FTIR peaks near 1650 cm^{-1}-1680 cm^{-1} and 1540 cm^{-1} (Figure 4.6), confirming the streptavidin attachment. Reflectance measurements (Figure 4.7(a)) show a microcavity resonance redshift of 12.9 nm after exposure of the functionalized PSi sample to streptavidin, which is also consistent with capture of streptavidin molecules in the PSi. We note that there is no spectral shifts after exposing a nonadiyne-modified PSi micro-

cavity (control sample, without peptide modification) to the streptavidin molecules. This supports the specificity of the SBP capture agents.

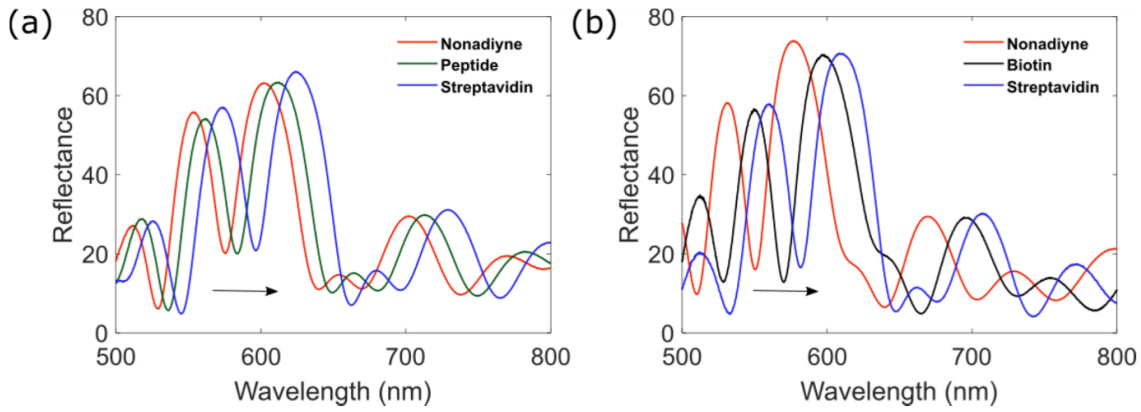

Figure 4.7: The reflectance spectra of (a) PSi microcavity after attachment of nonadiyne, streptavidin-binding peptide (24 h attachment), and streptavidin molecules (1 h attachment, 5μM) and (b) PSi microcavity after attachment of nonadiyne, biotin (24 h attachment), and streptavidin molecules (1 hour attachment, 5μM).

To compare the performance of the SBP as a capture agent for streptavidin molecules on PSi with the more commonly used biotin bioreceptor, reflectance measurements on using biotin as bioreceptor are taken after azide-terminated biotin molecules are attached to an alkyne-terminated PSi microcavity, and after streptavidin molecules are exposed to the biotin-modified PSi microcavity. Comparison of Figure 4.7(a) and (b) shows that the PSi microcavity resonance redshifts by a larger magnitude after biotin attachment (19.6 nm) than after peptide attachment (8.2 nm). This larger magnitude redshift suggests that more biotin molecules are present on the PSi surface compared to SBP. Note that biotin (MW: 244.3 gmol) is smaller than SBP (MW: 1061.2 gmol). A redshift of 11.7 nm is measured following the 1 h exposure of the biotin-functionalized PSi to streptavidin molecules. The resonance shifts measured after streptavidin capture in the biotin-functionalized and peptide-functionalized PSi microcavities do not differ significantly. This is despite the higher binding affinity of biotin, which is most likely indicative of the experiment being carried out in a dilute regime where the reaction is diffusion-limited.

4.6.5 Optimization of click reaction time and streptavidin incubation time

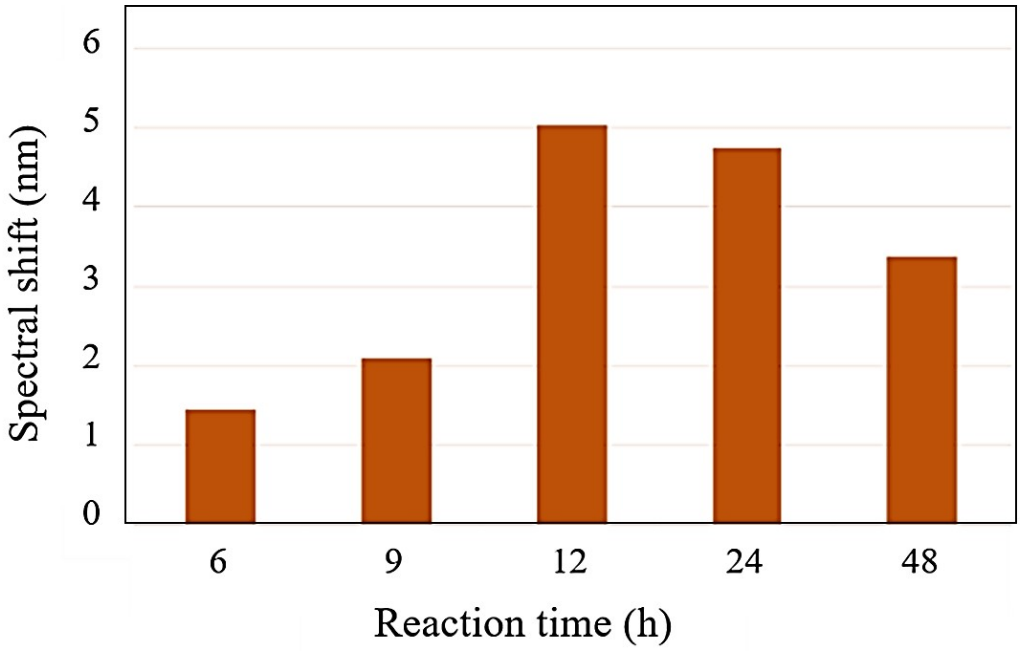

Figure 4.8: Alkyne-modified PSi microcavity resonance wavelength shifts after attaching azide-modified streptavidin-binding peptides with different click reaction times.

To optimize the reaction time for the copper-catalyzed click reaction protocol, different reaction times of the alkyne-modified PSi in the solution containing azide-modified SBP, copper (II) sulphate pentahydrate, and sodium ascorbate are evaluated at room temperature. Following each designated reaction duration (6—48 h), the post-reaction sample cleaning protocol described in Section 4.6.4 is carried out and then reflectance measurements are performed. Figure 4.8 suggests that the click reaction is completed after 12 h; the measured resonance shift is nearly the same after 12 h and 24 h, and therefore the number of peptide molecules added to the PSi surface is nearly the same during a reaction window of 12– 24 hours. For shorter reaction times, there is a notably smaller resonance shift suggesting the PSi surface is not saturated with the peptide molecules. The slight decrease in wavelength shift observed after the 48 h click reaction may be attributed to the corrosion of the PSi matrix during the extended incubation in aqueous solution.[109, 110]

To optimize the reaction time for streptavidin binding, three different incubation times

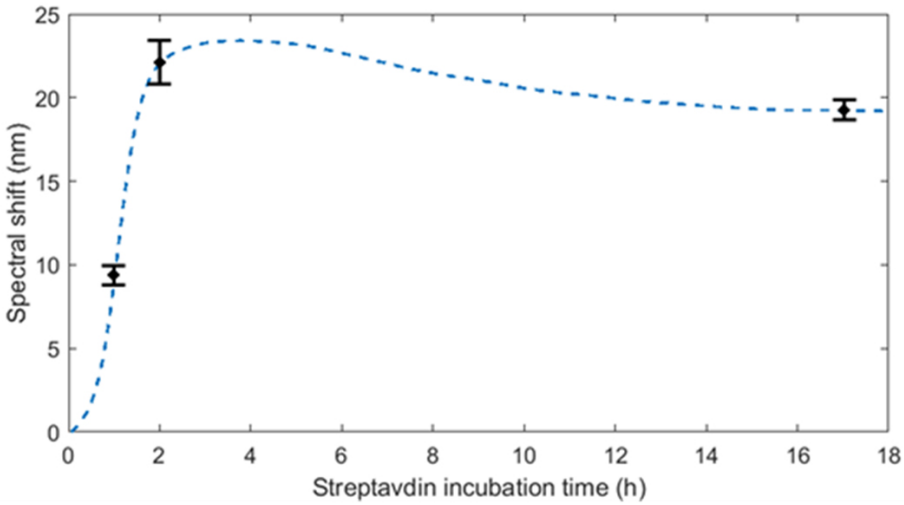

Figure 4.9: The redshifts of resonance wavelength of peptide-functionalized PSi microcavity after sample incubation in streptavidin (5 μM) for different time durations. The dashed line is shown as a visual guide.

for streptavidin molecules in peptide-modified PSi microcavities are evaluated: 1, 2, and 17 h. Figure 4.9 shows that increasing the streptavidin incubation time from 1 to 2 h more than doubles the magnitude of the resonance wavelength shift. However, no additional redshift is measured after overnight streptavidin incubation (17 h), suggesting that 2 h is a sufficient incubation duration to enable capture of the streptavidin molecules at most available binding sites. The slight decrease in resonance wavelength observed after the 17 h incubation may be due to PSi corrosion during the extended exposure to aqueous solution.[109, 110] These results for streptavidin incubation time in PSi are consistent with prior work that showed a 2 h incubation is appropriate for streptavidin capture in closed-ended PSi, while 30 min is sufficient when streptavidin molecules are exposed to the open-ended PSi membranes.[111]

4.6.6 Summary on streptavidin binding peptide attachment

In summary, the feasibility of using peptide-based capture agents as an alternative to antibodies and nucleic acid-based bioreceptors for PSi biosensors was demonstrated. Azide-

modified SBP capture agents are attached to alkyne-modified PSi microcavities via copper(I)-catalyzed azide alkyne cycloaddition (CuAAC), as verified by FTIR and optical reflectance measurements. The click reaction must proceed over a duration between 12 – 24 h to maximize coverage of the peptide capture agents in the PSi without introducing deleterious effects due to corrosion of the PSi matrix. FTIR and optical reflectance measurements also verified the successful capture of streptavidin target molecules; a 2 h streptavidin incubation time is sufficient to saturate most available binding sites. Under a given set of conditions evaluated (5 μM streptavidin in water, 1 h incubation), the SBP enabled nearly the same number of streptavidin molecules to be captured as the biotin bioreceptors. We believe the protocols developed for the attachment of azide-modified SBP capture agents in PSi is directly scalable to other azide-modified capture agents.

4.7 Chikungunya virus E2 protein detection

Chikungunya is an infection caused by the chikungunya virus (CHIKV) which is passed to humans by mosquitoes. The feature of the disease is a sudden onset of fever 2-4 days after exposure, frequently accompanied by joint pain. [112] The fever typically lasts 2-7 days, while the associated joint pains usually last weeks or months, but sometimes years. Although natural infection only occurs in tropical regions, CHIKV is of interest to global public health due its high infectivity when aerosolized, ease of large-scale production, stability under a wide range of environmental conditions, and large, cyclic epidemics. Moreover, CHIKV is an RNA virus which mutates rapidly, and the transmittance pathway may shift as a result of cumulative changes under environmental constrains.[113, 114] While severe joint pain is the most distinguishing feature of chikungunya fever, diagnosis remains difficult because the symptoms of chikungunya fever are shared by many pathogens, including dengue fever. [115] Typical CHIKV protein detection assays target IgM and IgG anti-CHIKV antibodies, however those antibodies only present 3–10 days after host

infection.[116, 117] While the PCR techniques can provide earlier diagnosis, it takes hours or a day to multiply the RNA of the virus. [118] There is an antibody assay reported, but the poor stability of antibody makes antibody biosensor production costly and unfeasible for POC test. [119] Recently, our collaborators reported a novel discovery and maturation strategy for the development of thermally stable peptide-based capture receptors.[76] Recombinant peptides against the unglycosylated E2 protein of CHIKV were developed and showed comparable performance with the E2 antibody, while maintaining high thermal stability.[120] To make the peptides available for POC diagnostics, we explored ways to incorporate CHIKV E2 binding peptides (CBP) to PSi platforms. In the following sections (and appendix B), we will report the PSi setups that have been examined.

4.7.1 Peptides on PSi chip

a) Experiment

The PSi microcavities were fabricated and functionalized following the procedures detailed in section 4.6.1. Copper (I)-catalyzed click chemistry was performed to attach the CHIKV E2 binding peptide (CBP, including the peptide sequences of WIYYI, YWHWS and IYLRY) to the ND-modified PSi surface. The procedures for the click reaction are detailed in section 4.6.2. After reaction, the samples were rinsed with DMSO, followed by anhydrous ethanol and DI water, and soaked in 0.5 mM HCl for 30 min to remove residual copper in the PSi pores. The samples were then cleaned with DI water and anhydrous ethanol, and dried under a stream of nitrogen. The functionality of CBP was evaluated through exposing the functionalized PSi sample to CHIKV E2 protein. A 20 μL solution of 1 μM E2 was drop cast onto CHIKV E2 binding peptide-modified PSi samples and incubated for 2 h, at room temperature. Following the incubation, the PSi samples were washed thoroughly with DI water, dried under a stream of nitrogen, and measured with reflectance spectrometry. Subsequently, 20 μL solution of 5 μM E2 was additionally drop cast on

the PSi sample and incubated for 2 h at room temperature. Following the incubation, the PSi samples were washed thoroughly with DI water, dried under a stream of nitrogen, and measured again.

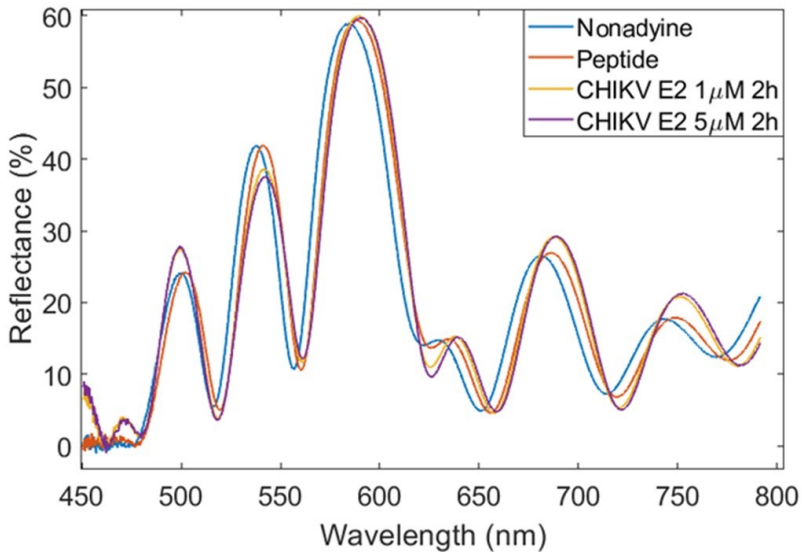

Figure 4.10: Reflectance spectra taken after nonadiyne modification, click chemistry, and E2 protein exposures.

b) Result and analysis

As shown in the Fig 4.10, after clicking the peptide IYLRY to the alkyne modified PSi surface, a redshift of 3.7 nm is shown. This indicates the successful binding of the CBP. However, after 1 μM CHIKV E2 incubation for 2h, only a small redshift of less than 0.4 nm is observed in the reflectance spectra. To examine if this is in the low concentration regime, a 5μM CHIKV E2 solution is added to the same PSi chip, another 0.4nm is shown. Then the same procedure was repeated on the PSi microcavities with different CBPs, WIYYI (4mM), YWHWS (7mM). Similar spectral shift (4-6nm) were observed after clicking the peptides with the PSi surface, but no significant spectral shifts are shown upon the CHIKV E2 incubation.

After examining the CHIKV E2 incubation process, we noticed the CBP modified PSi surface displayed a strong hydrophobicity with a water contact angle around 112 °, which

effectively prevent the water penetration and E2 protein diffusion. To reduce the surface tension, methanol and tween 20 solution were added to the CHIKV E2 solution separately. It turns out high concentration of methanol could denature the E2 protein, while low concentration methanol is not enough to reduce the surface tension. For another experiment, 0.1% tween 20 was added to the E2 solution and 0.1% tween 20 and equal amount of water (equals to volume of E2 solution) were used as the control. After 2h incubation and wash with abundant water, a spectral redshift of 20 nm was observed for both samples. It indicates the nonspecific binding of the tween 20 (MW$\sim$1228 Da) has either blocked the interaction of the CBP and E2 protein, or shadowed the spectral shift from CBP and E2 protein.

To overcome the hydrophobicity challenge, incubation of the E2 protein was performed in a pressure-controlled chamber.

4.7.2 Vacuum method

a) Experiment

The PSi microcavities were fabricated and functionalized following the procedures detailed in section 4.6.1. Once the peptide presence on PSi was demonstrated, we tested it with E2 protein for CHIKV infection detection. CBP YWHWS was attached to nonadiyne modified porous silicon microcavity samples through copper-catalyzed click chemistry as detailed in section 4.7.1a. After that, one sample was put into the bottom of a 25 mL filtering flask sealed with a rubber stopper. The setup was pumped into vacuum (air pressure $<$10 torr). A 50 μL solution of 1 μM of E2 in water was carefully dropped cast on top of the PSi microcavity surface using a syringe with a 6-inch-long needle. The vacuum was released slowly till it reached the atmosphere pressure. And the sample was then incubated for 2h. Another sample was treated with the similar procedure but incubated in a solution of 50 μL solution of 1 μM chicken albumin solution instead as a control experiment.

b) Result and analysis

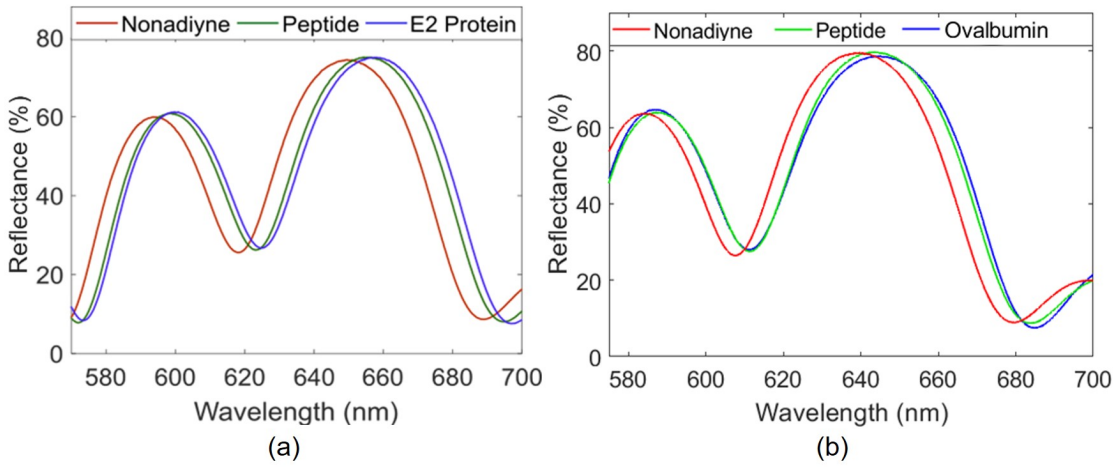

Figure 4.11: (a) Reflectance spectra taken after nonadiyne modification, click chemistry, and E2 protein exposure. (b) Reflectance spectra taken after nonadiyne modification, click chemistry, and chicken ovalbumin protein exposure.

Reflectance spectra in Figure 4.11(a) show a red shift following the peptide attachment by 5 nm. For the sample exposed to E2, the reflectance spectrum redshifts by 1.6 nm. This indicates the successful capture of the target by the peptides on the PSiM surface. On the other hand, as shown in figure 4.11(b), the reflectance spectra for sample exposed to chicken albumin showed no shift, which suggests that no chicken albumin is attached to the surface and the CBP-E2 binding is specific. Though the vacuum condition gets the water solution penetrating through the hydrophobic barrier, the process is not ideal for POC application. Therefore, several different approaches were investigated to enable E2 detection using a more straightforward and scalable approach, including flow cells and PSi membranes, dual functionalization, and azide surface modification. Unfortunately, none of these approaches, which are detailed in Appendix B, proved to be more effective than the vacuum infiltration approach. Ongoing studies continue to investigate alternative solutions.

4.8 Summary

The attachment and activity of peptide-based capture agents were demonstrated on a PSi platform. A copper-catalyzed click chemistry protocol for attaching azide-modified peptides was first developed on alkyne-modified PSi using a well-characterized SBP. This approach was then applied to attach peptide capture agents for the detection of the CHIKV E2 surface protein. Specific detection of the E2 protein was demonstrated using a vacuum-assisted infiltration process to overcome the highly hydrophobic nature of the PSi surface after peptide functionalization. Ongoing studies are investigating alternative strategies for detecting E2 in a more straightforward manner, including the use of a less hydrophobic azide-modified surface to attach alkyne-modified peptide-based capture agents.

CHAPTER 5

Machine learning and biosensing

5.1 Introduction

Machine learning (ML) is a fast developing discipline which uses statistical approaches to build or train models from data without the need to set up explicit mathematical equations or physical formulas.[121] Driven by today's vast data volume and widely available powerful data processing capability, ML related techniques have boomed at an unprecedented pace and have drawn the attention of researchers from almost all scientific fields, including not only computer sciences, but also health sciences, life sciences, material sciences, environmental sciences, psychology, finance and insurance.[122] Machine learning techniques can reveal hidden structures in big data and have the potential to replace or enrich analytical methods in many fields of scientific research. One such area is sensing and biosensing, which has become ubiquitous in modern systems in our society, and state-of-the-art technologies lead to massive amounts of data of various natures. Take photonic biosensors for example, the data obtained during sensing might be a spectrum (1D), a series of time dependent spectra (2D), a series of time dependent spectral maps (3D) or even hyperspectral videos. Moreover, dealing with biological systems or even in vivo experiments adds additional challenges owing to the variability of biological samples. In this case, precise analytical methods are too complicated to model the data, and ML become a necessity. In recent years, a number of ML methods have been employed in the field of biosensing; typical data analysis covers both exploratory techniques such as principal component analysis (PCA) and cluster analysis for discrimination, as well as supervised techniques such as linear discriminant analysis (LDA), decision trees, random forests, partial least squares discriminant analysis (PLSDA) and support vector machines (SVM) for

classification. [123, 124]

As discussed in previous chapters, peptides have the potential to replace protein antibodies as a future bioreceptor with lower cost and better stability. However, developing peptides still requires a considerable amount of effort and the stability of long-time storage is yet under scrutiny. Moreover, transducer surface modification, a necessary step prior to bioreceptor binding, takes additional time and requires strict reaction condition control. For instance, the hydrosilylation of freshly etched PSi takes $>$ 12 hours, and oxygen free environment is mandatory throughout the reaction; [125] 10-undecenoic acid modified PSi surface needs thoroughly ethanol rinse before drying in order to avoid PSi cracking; [126] and APTES silanization reaction depends heavily on the environment moisture. [127] As a result, a biosensor without receptor would be of great convenience, low cost and good storage stability. There are also occasions where no specifically binding receptor is available or the analyte is not known a priori.

The current solution for the receptor-free sensing is broadband optical spectroscopy, which uses broadband optical source to probe the analytes near the surface of the transducer. The output spectra contain multiple features, which need to be deconvolved with known analytes in the environment in order to ascertain the concentrations.[22] Because of the complexity of the environment, those spectra have inherently great variation and uncertainty. Therefore, it is challenging for spectroscopic biosensor to achieve high specificity and sensitivity, or even accurate recognition. The underlying physics of the spectroscopic methods include Raman scattering, Fourier transform infrared spectroscopy, X-ray photon spectroscopy etc., which differentiate the molecules by monitoring the intrinsic property of chemical bond vibrations, rotations or atomic level energy transitions. These spectroscopic methods have been proven to be effective when dealing with simple small molecules that have few signature groups, but the similarity (the chance of two kinds of biomolecules share the same groups) and the complexity of the spectra increase as the molecular weight

of biomolecules increases. On the other hand, the difference of molecular size, the charge mass ratio and the diffusivity of biomolecules when passing through media become more prominent with increasing of molecular weight. We propose a method that can differentiate biomolecules by tracking their interactions with predesigned PSi structures of various physicochemical properties. When a solution of biomolecules flows through the porous material, the molecules can be adsorbed onto the pore surface or trapped into the pores, which leads to change in the optical reflectance signal (Figure 5.1 (a), (b)). The adsorption and trapping of biomolecules are governed by their properties (size, isoelectric point etc.), the PSi structures (pore sizes and layer thicknesses, surface modifications, etc.) and the physicochemical condition of the solution (pH, flow rate, salt concentration). For given PSi array and solution condition, the optical reflectance signals reflect the properties of the biomolecules, and therefore have the potential to serve as the signatures of the biomolecules for identification purpose. As shown in the Fig. 6 of Ref [111] [Zhao et al, Nanoscale Res. Lett 395 (2016)], different biomolecules displayed different diffusion characteristics under the same flow conditions, and the same biomolecules behaved differently in different flow conditions if their sizes were comparable to those of the pores. By varying the structures of the PSi array and the solution conditions, the optimal combinations for separating biomolecules could be found—leading to the most unique optical signals when interacting with different biomolecules. To extract the molecules' signatures, machine learning methods can be employed. In the following sections, two possible schemes for biomolecule diffusion monitoring will be discussed and prospective machine learning methods will be laid out.

5.2 The flow cell scheme

As detailed in Chapter 1, porous silicon is an ideal material for biosensing and has been intensively studied in the past decades for its extremely large internal specific surface area,

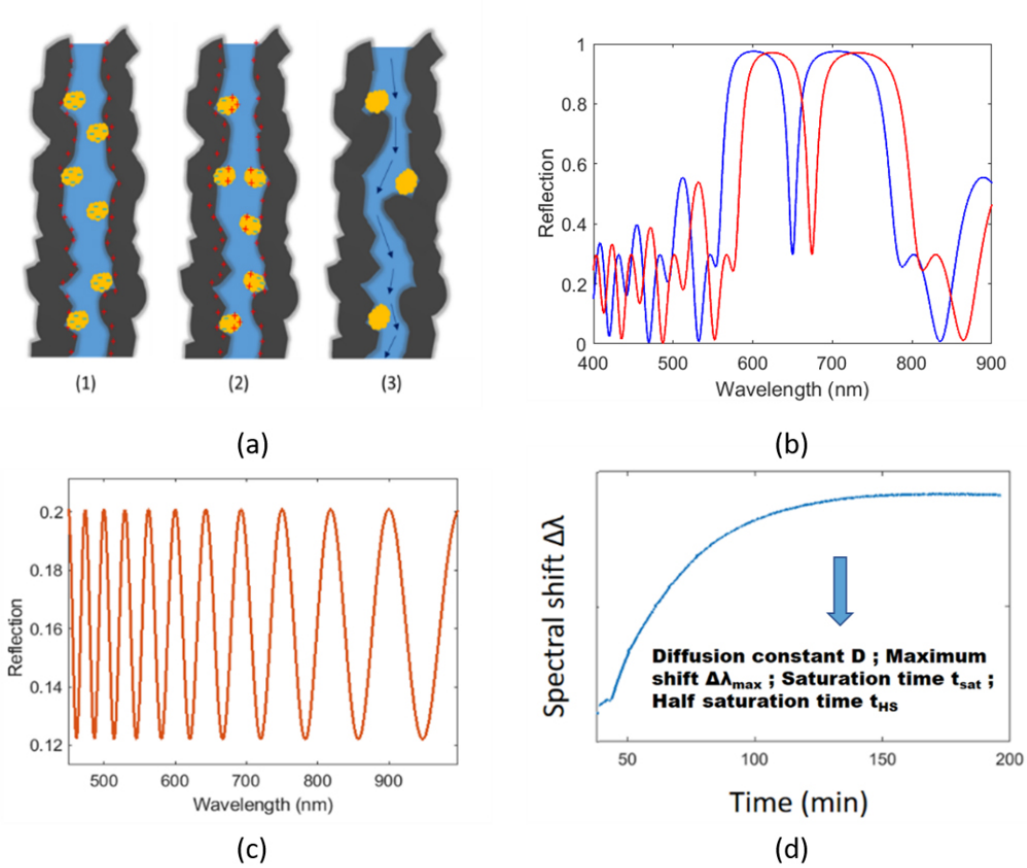

Figure 5.1: (a) Biomolecules, passing through a single layer of PSi, are trapped by (1) Coulomb force, (2) Van der Waals force, or (3) pore branches. (b) The reflectance spectrum of a PSi microcavity. (c) The reflectance spectrum of a single layer of PSi. (d) The response of a PSi structure, obtained by tracking the spectral shift over time.

tunable optical properties and low fabrication cost. However, the application of PSi as biosensors to detect large biomolecules with slow diffusivity is challenged by an associated long response time due to hindered analyte diffusion in the low porosity PSi structures. Multiple flow cell studies have been carried out both on open-ended and close end PSi structures, and found that open-ended flow-through cell is more efficient for mass transportation. [68, 111] Most of the studies on biomolecule transportation are restricted to the saturation time estimation, maximum adsorption and assay stability. In fact, the transportation dynamics provide valuable information to differentiate between different molecule species, enabling classification or recognition by carefully comparing the diffusion kinetics. Based

on that, we designed a double layer structure that could be potentially used to differentiate biomolecules.

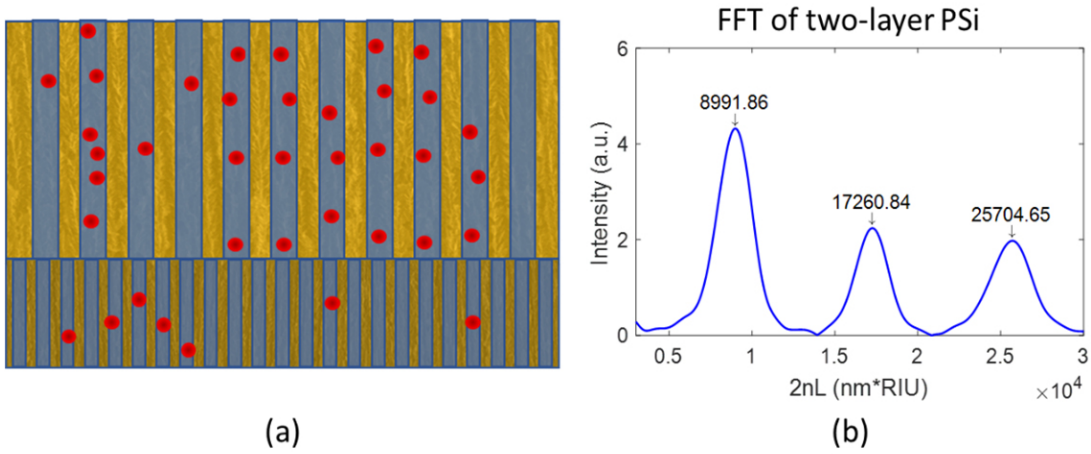

Figure 5.2: (a) Biomolecules diffused into a two-layer PSi. (b) The FFT of a two-layer PSi reflectance spectrum.

As mentioned in chapter 1, the single layer of PSi has a reflectance spectrum of a sinusoidal curve in the wavenumber space. When transformed by the FFT, the dominant peak indicates the EOT of the layer (peak position equals twice of EOT). By monitoring the EOT over time, the biomolecules' diffusion behaviors could be tracked. Figure 5.1 (d) displays the sensorgram of the biomolecules' diffusion, from which the maximum adsorption and the saturation time can be readily extracted. By simple derivation, the half saturation time and the adsorption rate at half saturation could be calculated. To increase the number of features that could enable more effective pattern recognition, we considered a two-layer PSi structure as shown in Figure 5.2(a): the additional layer of different pore size will provide more insight on the size of the biomolecules. We anticipate the smaller pores will have more effect on large molecules, as it is clear small pores will block the biomolecules that are larger than the pores. Even the biomolecules that are small enough to avoid being blocked, a smaller pore will still confine the biomolecules into a closer distance to the pore walls and change Coulomb force-based adsorption as well as the van der Waals interaction. The resulting changes in adsorption characteristics will manifest as changes

in the reflectance signals. In the two-layer design, the reflectance spectrum contains three major frequencies and displays three distinct peaks in optical path length space.(As shown in Figure 5.2(b)) Ideally, the $2n_1 L_1$and $2n_2 L_2$ are independent indicators of the molecular adsorption in layer 1 and 2. By applying a FFT to the spectrum, $2n_1 L_1$and $2n_2 L_2$ can be separated. To avoid the possible overlaps between two peaks, we set $n_2 L_2 = 2n_1 L_1$, so that the FFT peaks could have the largest separation for fixed $2n_1 L_1 + 2n_2 L_2$. By tracking the two peaks over time, two independent sensorgrams could be drawn, and both the maximum adsorption and the saturation time can be obtained for each layer, and these features will be used in further analysis. The methods for analysis will be detailed in section 5.4.

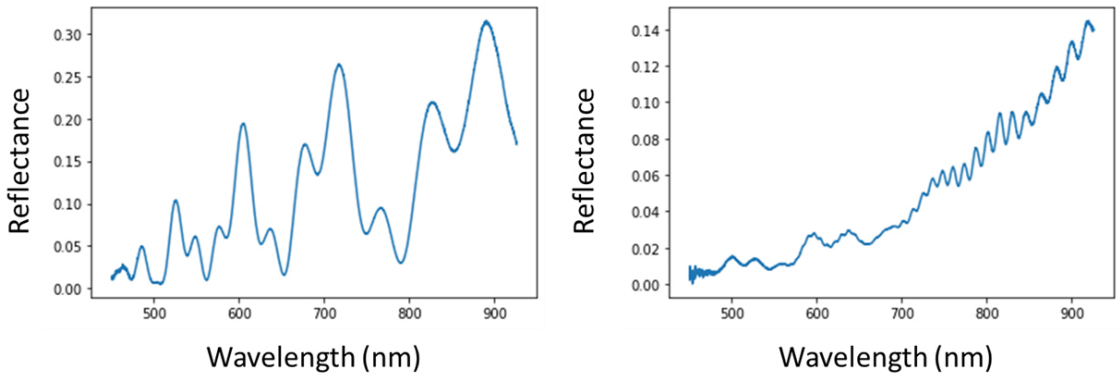

Figure 5.3: Reflectance spectrum of (a) a two-layer porous silicon structure on substrate in air (n=1.00); (b) a two-layer porous silicon flow through cell in water (n=1.33).

Figure 5.3 (a) and (b) show the experimental reflectance spectra of a two-layer PSi structure in air and a two-layer PSi flow-through cell in water. To explore the cause of dramatic signal reduction, transfer matrix method-based simulation was used. The result is displayed in Figure 5.4 (b), where the flow-over signal amplitude is about 4 time stronger than the flow-through signal. Therefore, the above two-single layers design may work well for flow-over scheme, where the substrate of the silicon has a high refractive index contrast to the sensing layer leading to high reflection and better signal to noise ratio. However, when flow-through scheme is used, the silicon substrate is replaced with water, a material has similar index to PSi. The signal extraction becomes a challenge. To solve that, rugate

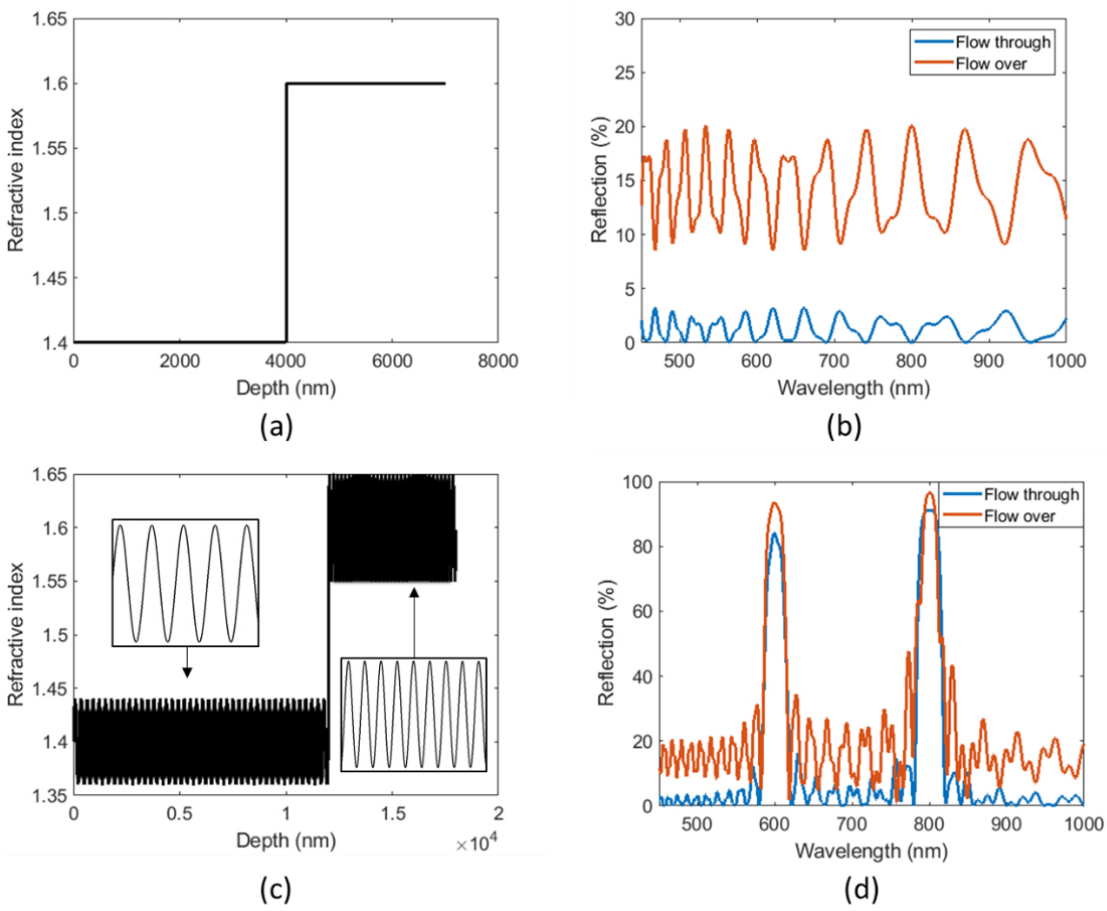

Figure 5.4: The comparison of two-single layers vs two-rugate filters. Top: (a) The refractive index profile and (b) simulated reflectance spectra of a two-layer optical structure in flow-through and flow-over settings. Bottom: (c) The refractive index profile and (d) simulated reflectance spectra of a two-rugate filter structure in flow-through and flow-over settings.

filter is used to replace the single layer in the later design. Unlike the single layer, the reflectance spectra of rugate filter show little dependence on the refractive index of the substrate (as shown in Figure5.4 (c),(d)). Two-rugate filters design exhibits more than 20 times improvement in signal to noise ratio when flow through scheme is used. Though the pore size varies inside the rugate filter, the change is relatively small and the diffusion physics of the rugate filter approximates the single layer.

5.3 Sensor arrays

Other than stacking the two single layers (or Rugate filters) together to form vertical two-layer structure, assembling different sensing units into arrays offers an alternative way of getting higher dimensional data for pattern recognition-based sensing. Several papers have been reported using sensor arrays for recognizing chemicals or proteins. As this approach resembles the working mechanism of the mammalian olfactory system, such sensors are also referred to as optoelectronic nose.[128] For example, by using a 4×4 sensing array filled with different catalysts and dyes, Lin et al. reported a sensor that can differentiate Triacetone triperoxide (TATP), an acute explosive, from H_2O_2, acetone and bleach.[129] By using five different kinds of gold nanoparticles decorated green fluorescent protein sensing array, Rotello et al. reported a sensor that can identify five different kinds of proteins and even provide information on the protein concentrations.[130] However, we note the works reported earlier all use proteins or complicated assays as a sensing mechanism. To fulfill the objective of bioreceptors-free sensing, we propose a sensor array with PSi regions of different properties, aiming to use distinctive diffusion patterns to replace the patterns exhibited during chemical reactions.

The working principle is illustrated in Figure 5.5, assuming the biomolecule is smaller than the pore diameters of PSi. When the biomolecules diffuse into the four different media, four different diffusion characteristic curves are exhibited in Figure 5.5(b). After incubation for time t_0, the sensor array was taken out of the solution and the spectral shifts of the four PSi region are measured as $\Delta\lambda_1$, $\Delta\lambda_2$, $\Delta\lambda_3$, and $\Delta\lambda_4$, respectively. For a given t_0, X = [$\Delta\lambda_1$, $\Delta\lambda_2$, $\Delta\lambda_3$, $\Delta\lambda_4$] could be used as a characteristic vector to represent the biomolecules of a certain species at a certain concentration. The characteristic vectors are then collected and analyzed by machine learning methods, which will be discussed in the next section.

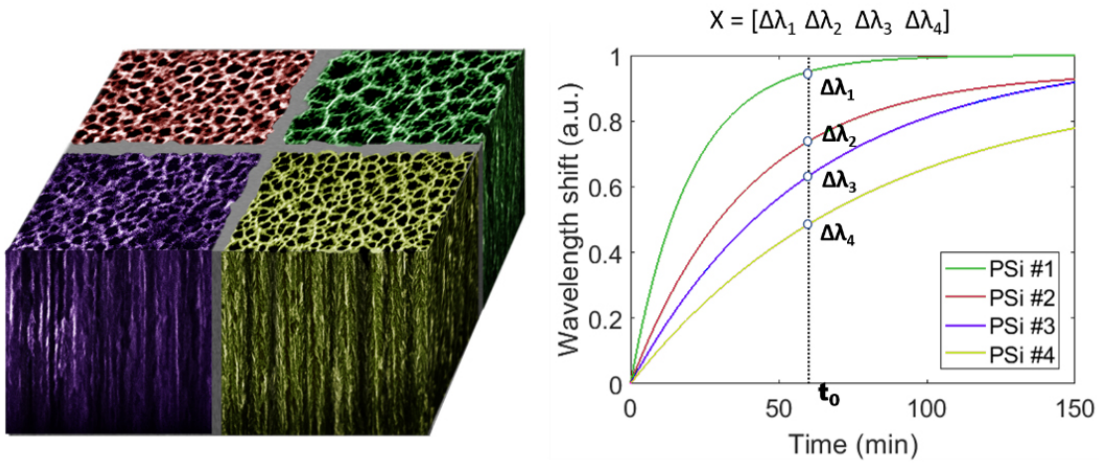

Figure 5.5: (a) The schematic illustration of a sensor array consisting of four different PSi regions with different pore sizes. (b) The conceptual saturation curves of a specific biomolecule diffusing into four different PSi regions. Assume the experiment stops at t_0, and the spectral shifts of the four regions are $\Delta\lambda_1$, $\Delta\lambda_2$, $\Delta\lambda_3$, and $\Delta\lambda_4$, respectively.

5.4 Machine learning methods

Machine learning has been widely used to process high dimensional data for classification and regression. The most common methods include principal component analysis (PCA) for unsupervised learning, autoencoders for semi-supervised learning, and k-nearest neighbor, linear discriminant analysis (LDA), Partial Least Squares Discriminant Analysis (PLSDA) and support vector machine (SVM) for supervised learning. In the following sections, we will introduce the prospective machine learning methods that could be used for biomolecule recognition.

5.4.1 Principal component analysis

Principal component analysis is probably the oldest and the most well-known method in the domain of machine learning. The main idea of the PCA is to reduce the dimensionality of a data set with a large number of interrelated variables, while retaining as much variation as

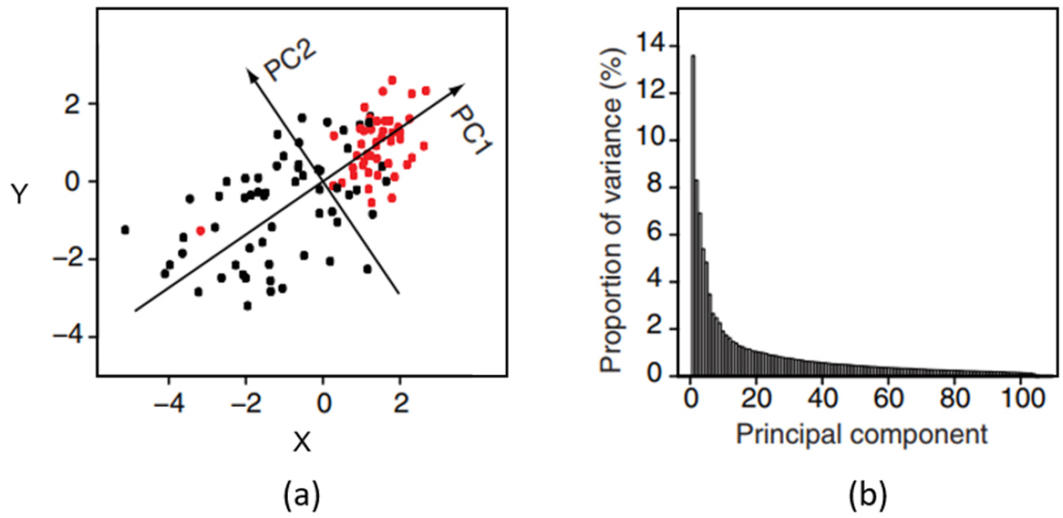

Figure 5.6: (a) An example of principal component analysis applied on gene expression data set. (b) The variance of the principal components when PCA is applied to all 8,534 genes with expression levels for all samples. Adapted with permission from Ref [131], Copyright 1969, Nature Publishing Group.

possible. [131] This reduction is achieved by constructing a series of orthogonal directions (bases) which maximize variance, and projecting the data onto the directions representing the largest variations (shown in Figure 5.6) Those newly constructed vectors are called the principal components, and the first few elements of the vectors retain most of the variation present in all of the original variables. PCA reveals the internal correlation of a data set by showing how the data in the set varies: a dimension of large variance indicates that samples vary significantly across this dimension, while a dimension of small variance indicates the samples are less distinguishable across this dimension. Often, classification among the first few principle components is enough to account for the variation of the whole dataset. The percentage of the variance represented by each dimension is also relevant. Typically, a number of dimensions are kept that capture a high proportion of the total variance across all dimensions (usually 95%).

Because the PCA concentrates the variations to the first few principle components, the plot of the data projected onto the first few principle components data are generally more

intuitive given their reduced dimensionality. For example, in Lin's paper *Colorimetric sensor array for detection of triacetone triperoxide vapor*, the PCA processed data is much clearer than the high dimensional RGB color array.[129]

5.4.2 K-nearest-neighbor method

KNN method is one of the simple and most fundamental classification methods and should be one of the first choices for a classification study when there is little or no prior knowledge about the distribution of the data. KNN is a non-parametric learning algorithm, which does not train any model, but simply uses a database, in which the data points are separated into several classes to predict the category of a new sample point.

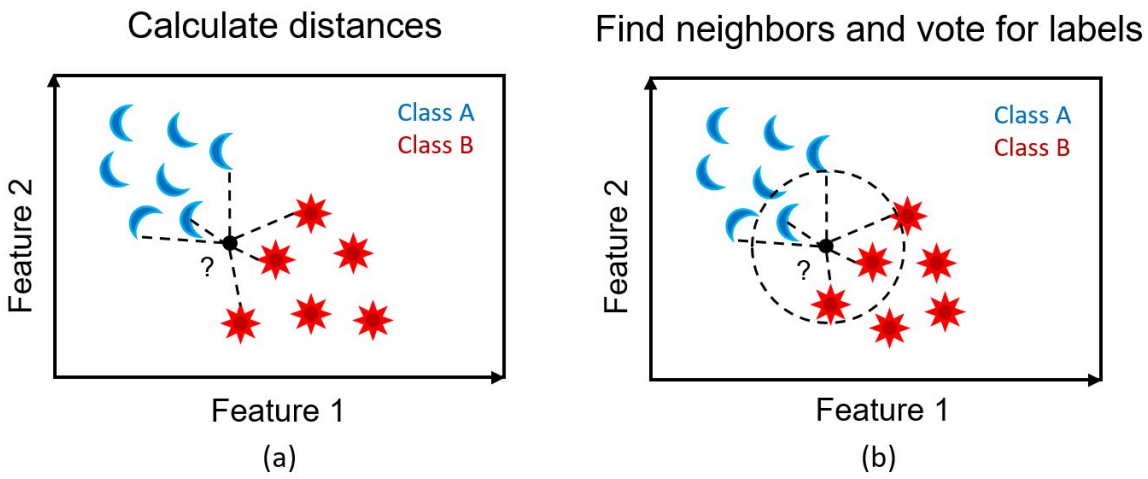

Figure 5.7: The procedure of performing KNN on classification. (a) Calculating the distance. (b) Finding nearest neighbors and voting for labels. The figures were generated based on Ref [132].

In KNN, the training examples are vectors in a multidimensional feature space, each with a class label. The training phase of the algorithm consists only of storing the feature vectors and class labels of the training samples and the output for the classification which is the class membership. The membership of the new sample point is generally decided by

a “popular vote”. The general steps for KNN are shown in Figure 5.7, which include calculating distance, finding nearest neighbors and voting for labels. For continuous variables, a common distance metric to use is Euclidean distance, whereas for discrete variables, metrics like Hamming distance can be used. The number of neighbors –K is a hyper-parameter decided while model building. No optimal K has been found that suits all kinds of datasets: a smaller K will have low bias but high variance, which is more susceptible to noise; while a larger K results in a smoother decision boundary which means lower variance but higher bias, and larger K also increases computationally complexity.

KNN works better with low dimension feature space, as an increase in dimensionality may lead to overfitting. To avoid overfitting, the sample population needs to grow exponentially. This problem is known as the Curse of Dimensionality. To address this issue, PCA could be used to preprocess the data and reduce dimensionality before KNN is applied.[132]

5.4.3 Linear discriminant analysis

LDA works like PCA, both methods reducing the dimensionality by constructing a new set of orthogonal dimensions consisting of linear combinations of the original space, but instead of finding the maximum variation, LDA tries to separate the known group as clearly as possible for the purpose of classification, which involves maximizing the inter-class difference and minimizing the intra-class variation.[133] Figure 5.8 is a schematic illustration of the LDA method. Due to this optimization, LDA generally shows better capability of differentiating the analyte among different classes than PCA. Compared to other methods, LDA has clear analytical expressions and the only tunable parameter is the threshold of selection, which make the model easy to justify.

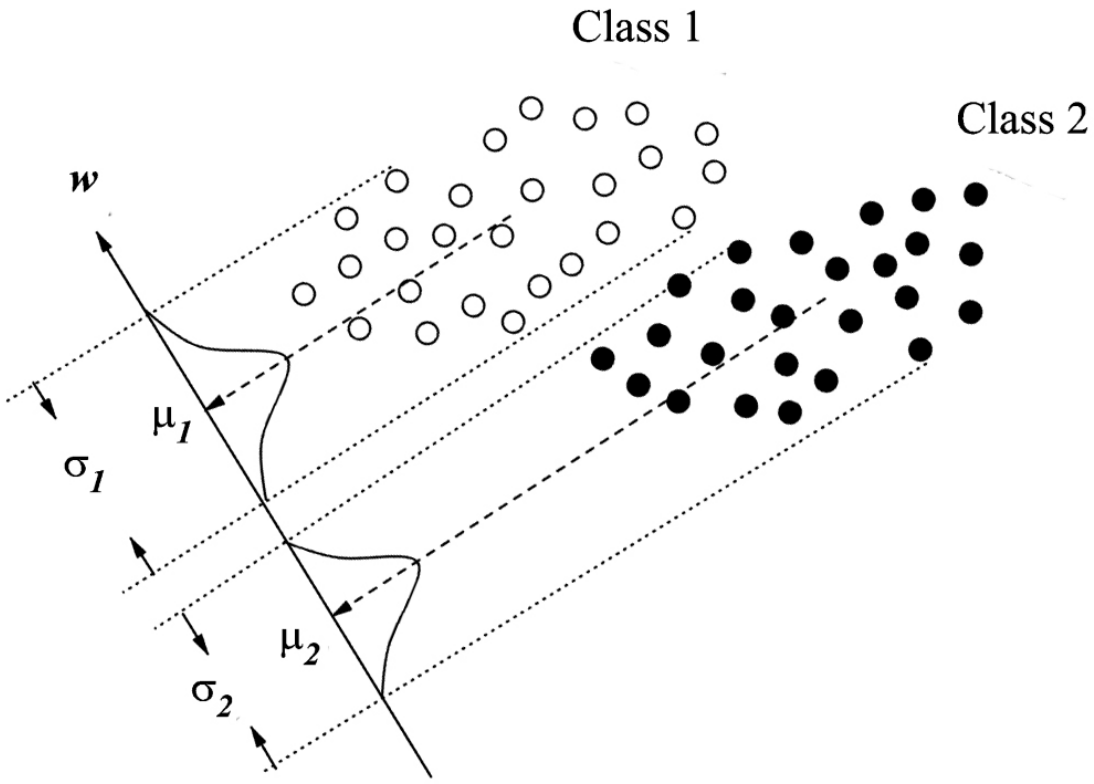

Figure 5.8: Illustrations of LDA for two classes. One searches for a direction $\mathbf{w}$ such that both the inter-class difference, here the between the class means projected onto this direction (μ_1 and μ_2) is large, and the intra-class variation (σ_1 and σ_2) is small. Reprinted, with permission, from Ref [133].Copyright 2009, IEEE

5.4.4 Support vector machines

SVM is an optimization-based discriminative classification method, which separate different classes by finding hyperplanes that maximize margins between them. The points near the decision boundaries are called support vectors, which are valued more than the points far from boundaries. Consequently, the classifier is called support vector machines. For SVM, the raw data are usually first transformed by the kernel functions, which maps the inputs into a high-dimensional feature space. Based on the choice of kernel, SVM can perform both linear and nonlinear classifications.

Besides the kernel function, there are two important tuning factors for SVM—the reg-

ularization parameter (C parameter) and the Gamma parameter. The C parameter balances the tolerance of misclassification and the size of margins. For a larger C value, the optimization will choose a smaller-margin hyperplane if that hyperplane gets more training points classified correctly. On the contrary, a smaller C value optimizer tends to find a larger margin separating hyperplane, but at the price of misclassifying more points. The Gamma parameter controls the influence of the training dataset. High gamma value weighs support vectors and the points near the boundaries more, while low gamma value can reach the data points that are far away from the boundaries.

Compared to other methods, SVM is highly stable and does not require a large sample population. Because only support vectors are important, a lot of points are actually ignored in the calculation. However, the drawback is that SVM does not have analytical solutions, therefore the kernel functions, C and Gamma parameters need to be carefully selected and well justified.

5.4.5 Autoencoders

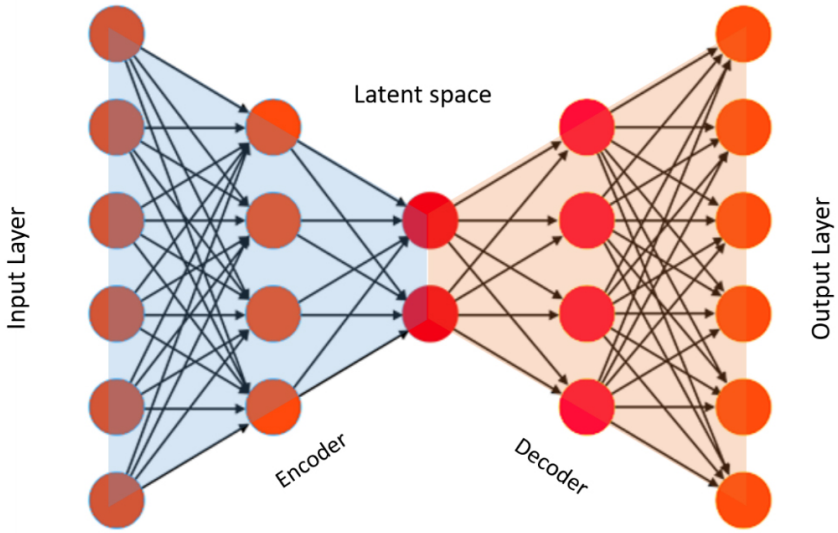

Figure 5.9: The schematic of an autoencoder, made up of an encoder and a decoder.

Autoencoders are simple neural architectures, which employ the special artificial neu-

ral network (ANN) structure for the task of data compression, noise reduction and feature extraction. The autoencoders are structured to have the input and output layer of the same format, with the training goal to minimize the discrepancy between the two, while maintaining an intermediate layer of low dimension.[134] As shown in Figure 5.9, an autoencoder is generally made up of two parts –an encoder that compresses the high dimensional input data into a low dimensional representation and a decoder that reconstructs the original input from the low dimensional data extracted by the encoder. Once the ANN is properly trained, the encoder part becomes a powerful automatic feature extractor, and the output layer of the encoder is called latent space, which contains the features extracted. Autoencoders are closely related to PCA: if the activation function used within the autoencoder is linear within each layer, the latent variables present in the latent space directly correspond to the principal components from PCA. Generally, the activation function used in autoencoders are non-linear, commonly used examples are Rectified Linear Unit (ReLU) and sigmoid.

Like PCA, autoencoders can be used to preprocess the training data and reduce the complexity of the later learning steps. Because the autoencoders are trained to predict their own inputs, it is often referred to as semi-supervised learning. However, the training goal can be modified and included supervised targets, which makes the system very versatile.

5.5 Experiments

5.5.1 The sensor array schemes

The above sections have covered the two diffusion-based sensing constructions and the possible machine learning methods to be used for data analysis. Due to the relatively simple fabrication process and short data collection time, the sensor array scheme will be pursued first.

The sensor arrays has been fabricated with masking and wet etching, and photos of

the results are shown in the Fig 5.10. The whole wafer was first deposited with the S1813 photoresist (PR) before wet etching. Only the area to be etched (one of the four squares) are exposed to the UV light and the PR of that region was removed with the RF 319 developer. Then a single current (70mA$\cdot$ cm^{-2}) is applied across the entire wafer in a 15% HF solution (50% HF and Ethanol, v:v=3:7) to etch a PSi single layer. After etch, the PR was removed via acetone rinse and the wafer was cleaned in DI water and IPA thoroughly. The above process was repeated 3 more times with different current densities (50mA$\cdot$ cm^{-2}, 60mA$\cdot$ cm^{-2} and 80mA$\cdot$ cm^{-2}) applied. After removing the final PR, the wafer was incubated in acetone overnight to prevent the possible pore blocking. The as-fabricated devices were cut into small units and oxidized in 500 °C in air for 5 min.

For the process of protein infiltration, the fabricated devices were exposed to two kinds of protein, chicken ovalbumin (COA) and bovine serum albumin (BSA) of various concentrations (0.25mg$\cdot$ mL^{-1}, 0.5mg$\cdot$ mL^{-1}, 1mg$\cdot$ mL^{-1} and 2mg$\cdot$ mL^{-1}) at pH = 4 for 2h. The data were collected using an Ocean Optics spectrometer to measure optical reflectance, and then processed using PCA in the standard python machine learning library—Scikit-learn.[135] The experimental results after PCA analysis are exhibited in Figure 5.11. The PCA results demonstrated the clear separation of the trend lines for the different concentrations of the two proteins. This preliminary experiment suggests that it is feasible to distinguish two proteins with different molecular weight and similar isoelectric point (BSA, MW = 66.5 kDa, pI = 4.8 and chicken ovalbumin, MW = 45 kDa, pI = 4.5) by exposing the proteins to PSi films with different pore diameters. This result matches the expectations since the diffusion properties of proteins depend in part on the size relationship between the protein and the PSi pore diameter.

No conclusions can be drawn related to the degree to which the proteins can be quantified based on this work other than to note that there is a general monotonic trend that is observed in the data with changing concentration. Multiple repeat experiments correspond-

ing to the conditions for each data point would have to be taken to establish the level of variation between identical experiments, which could then be compared to the separation between data points corresponding to different concentrations.

As we noticed that PSi pieces inside the solution was not portable or scalable, flow-over cells were employed. An ethanol and water (v:v=1:1) mixture was pumped through first to wet the channel, followed by buffer solution to saturate the PSi channel and stabilize the baseline of the signal. Finally, the analyte solutions was pumped through at a rate of 1μL·min^{-1}. The exemplary results are displayed in Fig 5.12 and more repeats are summarized in Table 5.1. From the results, we could conclude that the different analytes of different concentrations show relatively stable diffusion patterns, which lays the foundation for later molecular classification.

Analyte type	Pore size	Repeat 1 (nm)	Repeat 2 (nm)	Percentage difference
COA 1.0 g/L	Large	7.9	7	12.9%
COA 1.0 g/L	Large	7.3	7.3	0.0%
COA 0.5 g/L	Large	4.1	5.3	22.6%
COA 1.0 g/L	Small	1.2	1.3	7.7%
BSA 1.0 g/L	Large	1.9	1.8	5.6%

Table 5.1: More repeats of the flow-cell experiments with different combinations of analytes, concentrations and PSi pore sizes. The values are the spectral shifts (in nanometers) at 2-hour time point. Large pores are etched with a current density of 70 mA· cm^{-2}, and smaller pores are etched with a current density of 50 mA· cm^{-2}.

5.5.2 Fabrication of double rugate filter PSi structure for future experiments

As detailed in section 5.2, the vertical two-rugate filters will have better signal to noise ratio compared to simple PSi double layer when being measured in solution. A double-rugate filters PSi structure was fabricated in 15% HF using the etching recipe shown in the

Step	Current density ($mA \cdot cm^{-2}$)	Time (s)	Current density ($mA \cdot cm^{-2}$)	Time (s)	Number of repeats
1	80	4.45	60	5	40
2	70	50.0	0	0	1
3	30	4.21	45	4	60
4	70	250	0	0	1

Table 5.2: The etching recipe for fabricating a double-rugate filters PSi structure using 15% HF.

table 5.2. A sacrificial layer was added as it will be necessary for future application of the double rugate filter PSi structure in flow-through membranes.[24] Figure 5.13 shows (a) a cross sectional SEM image of the double-rugate filter PSi structure, (b) and its reflectance spectrum. The experiments using this structure will be carried out later, leveraging its clear physical advantages and strong flowing dynamics, which we predict will lead to a better classification precision.

5.6 Conclusion

In summary, we introduced the motivation of developing a bioreceptors-free biosensing system and outlined the potential working principles. Two mechanisms to achieve biorecognition were proposed: one using a sensor array and the other utilizing a multilayer PSi stack. A variety of machine learning methods that could be used for sensor data analysis were discussed, and the preliminary results using a sensor array to differentiate two proteins were shown. Finally, the experiments to identify the links between the sensor responses and biomolecule-PSi nanostructure interactions using a multi-variable system were proposed.

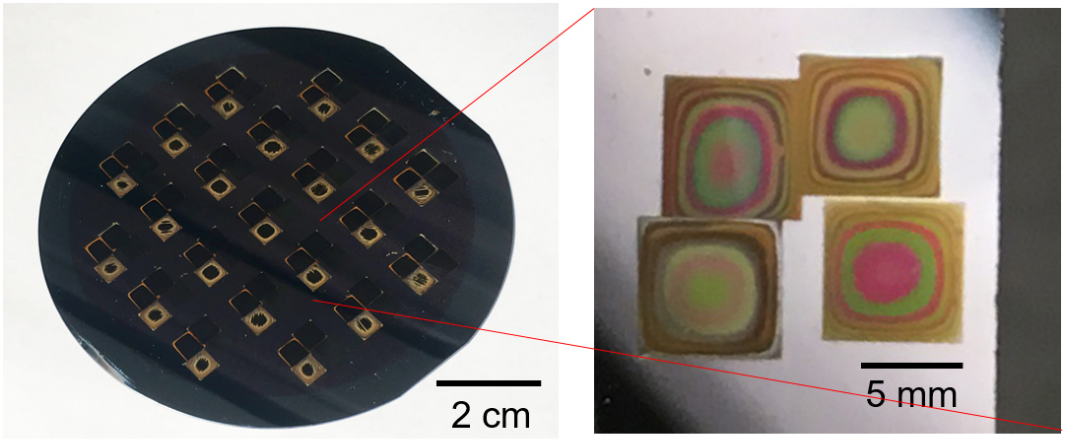

Figure 5.10: (a) The image of the fabricated PSi sensor arrays on a 4-inch wafer. (b) The single unit of the PSi sensor array consisting of four PSi regions with different pore sizes.

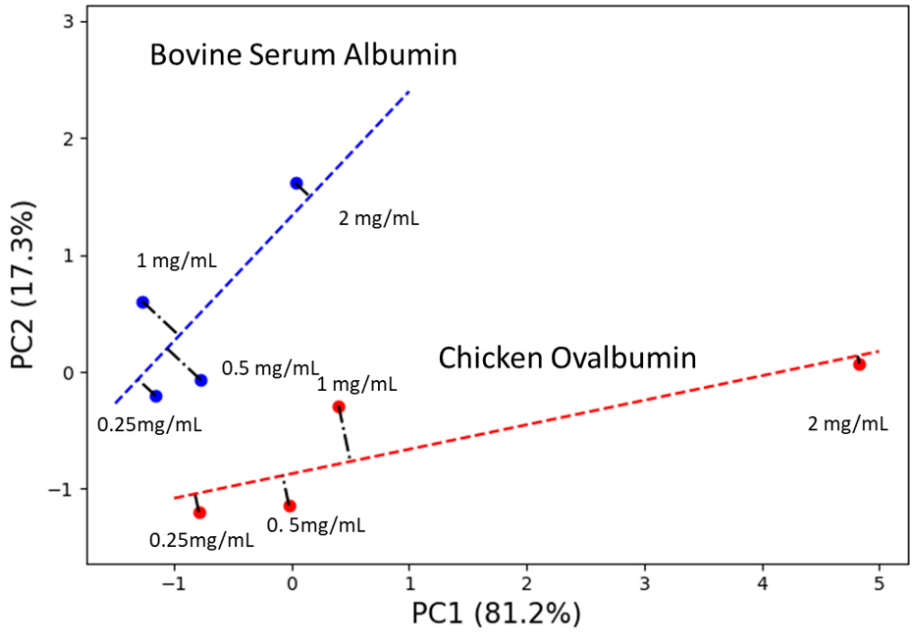

Figure 5.11: Application of principal component analysis to distinguish and quantify four different concentrations of BSA and chicken ovalbumin (COA). The different protein solutions (pH = 4) were each exposed to PSi films with four different average pore diameters, and the reflectance of the PSi films was measured before and after 2-hour protein infiltration.

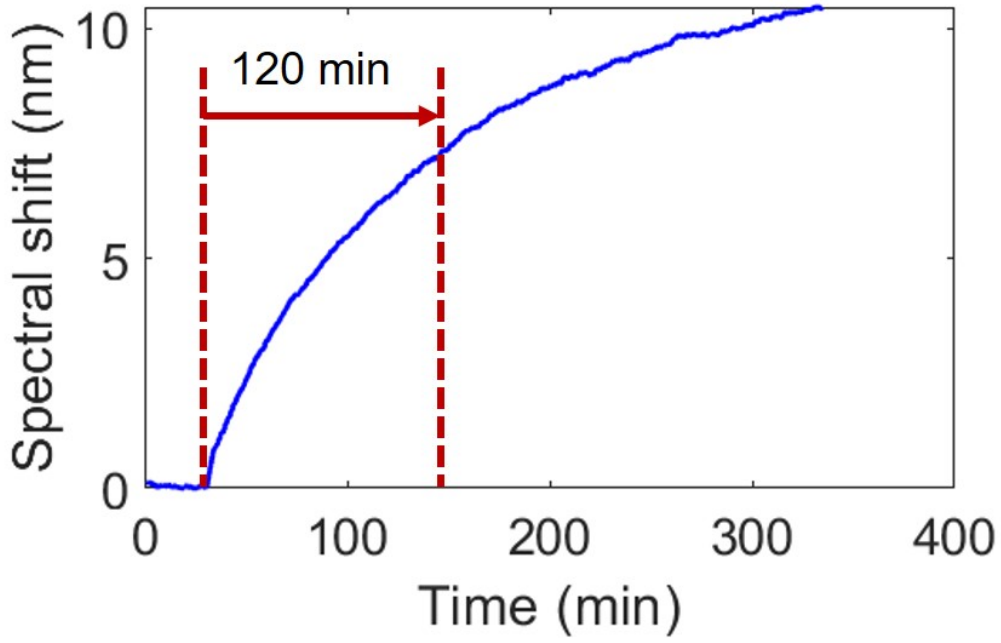

Figure 5.12: The exemplary results of a flow cell experiment. Two dashed lines are separated by a time interval of 2h.

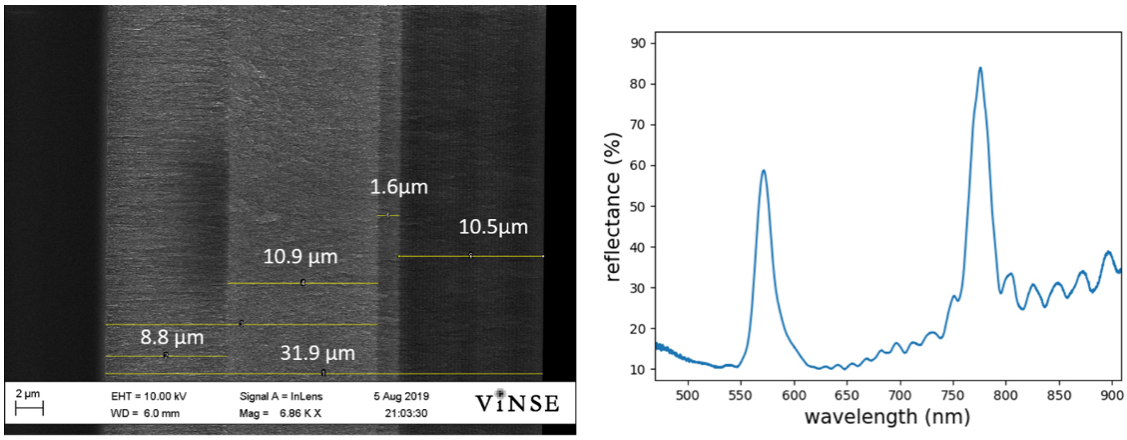

(a) (b)

Figure 5.13: (a) A cross sectional SEM image of the double-rugate filter PSi structure, and (b) its reflectance spectrum.

CHAPTER 6

Conclusions and future research opportunities

6.1 Summary

In summary, three aspects of the PSi POC biosensors have been explored. By combining PSi with smartphone, peptides and machine learning respectively, I demonstrated a cost-effective portable biosensor, explored several different ways to incorporate peptides to a porous silicon matrix, and built the concept of a bioreceptor-free biorecognition system.

Chapter 1 served as an introduction to the concepts, ideas and devices of optical biosensing and point of care diagnosis. PSi, which is the material this thesis focuses on, and the common devices fabricated out of PSi were also introduced, which served as a backbone for developing all of the applications and devices covered in the following chapters of the dissertation.

Chapter 2 detailed the working principles and operating procedures of (1) SEM, which was used for the PSi pore size, porosity, and layer thickness determinations; (2) reflectance spectrometer, which was a common tool for optical signal acquisition.

Chapter 3 presented a smartphone based PSi biosensor that combined the advantages of both the smartphone and PSi, achieving a low cost system whilst retaining decent performance metrics. The sensor links PSi structural color changes to biomolecule attachment, and monitors the change through smartphone camera. It is a promising platform for real-world POC applications.

Chapter 4 examined various methods to include peptides, a robust alternative to protein bioreceptors, to the PSi matrix to achieve biosensing in harsh conditions. A successful

approach was developed, namely using ND modification to achieve the necessary alkyne termination on the PSi surface to enable azide-modified peptide capture agents to be attached through click chemistry. This approach was demonstrated to add SBP to PSi for the successful capture of streptavidin molecules at a sensitivity similar to that when biotin molecules are used to capture streptavidin. The same functionalization approach was used to click azide-functionalized peptide capture agents to a alkyne-modified PSi for the detection of the CHIKV E2 surface protein. Due to the hydrophobicity of the surface, infiltration of E2 was carried out in a pressure-controlled chamber. Measurements demonstrated successful capture of E2 using this approach while control experiments with a non-target protein showed no signal change. Ongoing efforts are investigating alternative approaches to reduce the hydrophobicity of the surface.

Chapter 5 delved into the conceptual development of a bioreceptor-free biorecognition system. The chapter first introduced the motivation why bioreceptors-free systems are attractive and outlined the potential working principles of such a system. Two schemes were proposed, one being a sensor array, the other using the multilayer PSi stack, and a collection of machine learning methods that could be potentially useful for analysis were introduced. Next, preliminary results using a sensor array to differentiate two proteins were shown, and the experiment based on a multi-variable system was planned.

6.2 Future Research Opportunities

Chapter 3, 4, 5 addressed the POC biosensing from different perspectives. It would be interesting to combine the technologies together, for example, with a smartphone biosensor using peptides as the bioreceptor or a biorecognition element-free system using smartphone as the detector. The ubiquitous nature of the smartphone and the robust nature of the peptide (or biorecognition element-free system) will make the POC sensor accessible to people around the world in all kinds of settings.

Appendix A

Notes to readers : The appendix was reproduced with permission from my previous publication:

A smartphone biosensor based on analysing structural colour of porous silicon. Analyst, 144 (13): 3942–3948, 2019.[51]

A.1 Smartphone measurement procedures

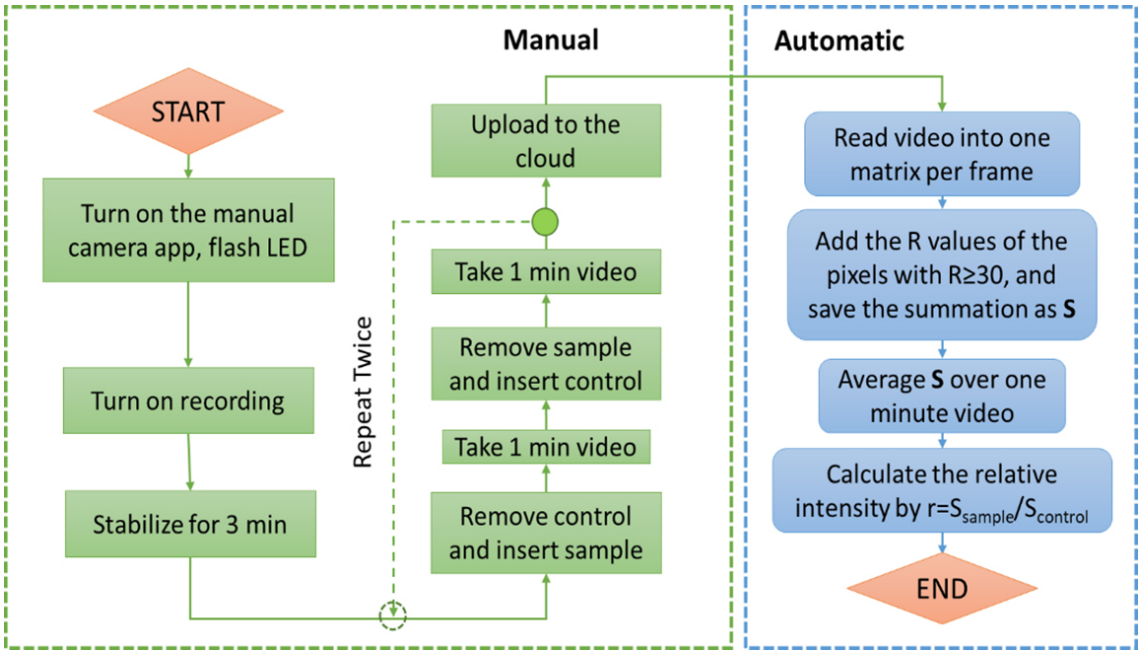

Figure A.1: Test procedure of the smartphone biosensor. The left side is done manually and the right side could be fully automated.

Figure A.1 provides an overview of the procedures used for the smartphone measurements. First, the control sample, a bare piece of silicon, is placed inside the 3D printed box in the designated position below the smartphone camera. The smartphone manual camera app is then turned on, the LED flash is set to 100%, and the settings for the camera focus, zoom, ISO, speed, exposure value, and white balance are adjusted to ensure that the image is not saturated. These settings are then fixed throughout the measurements. A video is then initiated with the control sample under the camera and recording continues for about 3 minutes until the light source is stabilized and the intensity fluctuations are significantly

reduced. Next, the control sample is removed and the PSiM sample is inserted into the platform, and a short video of approximately 1 min duration is taken. Then the PSiM sample is removed, the control sample is placed back into the 3D printed box, and a short video of approximately 1 min duration is taken to be used for normalizing the intensity data from the PSiM sample. The PSiM and control samples are iteratively measured a total of three times to evaluate the stability and repeatability of the system.

In order to obtain and process the data from the smartphone, the videos are uploaded to a computer and read by a MATLAB code that turns each video into a series of RGB images (24 frames per second). Each frame comprises three matrices containing R, G, and B intensity values, respectively, for all the pixel locations. The R values of pixels with R $\geq$ 30 are summed together as S for each frame of the video with the exception of a few frames at the beginning and end of the video. Then, an average S value for each video (Ssample and Scontrol for the PSiM and control sample, respectively) is determined by calculating the average S value for approximately 500 frames whose S value falls within the 30th-70th percentile of all values within the 1-minute video. The relative intensity measured by the smartphone is calculated by taking the ratio of Ssample and Scontrol, as given in Eq A.1. The standard deviation σ is calculated based on consideration of the three independent measurements of Ssample and Scontrol taken for each PSiM preparation condition (e.g., each APTES exposure or each streptavidin concentration), as given in Eq A.2.

relative intensity:

$$r = \frac{S_{sample}}{S_{control}} \tag{Eq A.1}$$

standard deviation:

$$\sigma = \sqrt{\frac{1}{3}\sum_{n=1}^{3}(r_i - \bar{r})^2} \tag{Eq A.2}$$

where

$$\bar{r} = \frac{1}{3}(r_1 + r_2 + r_3)$$

A.2 Bulk refractive index spectral sensitivity of PSiM

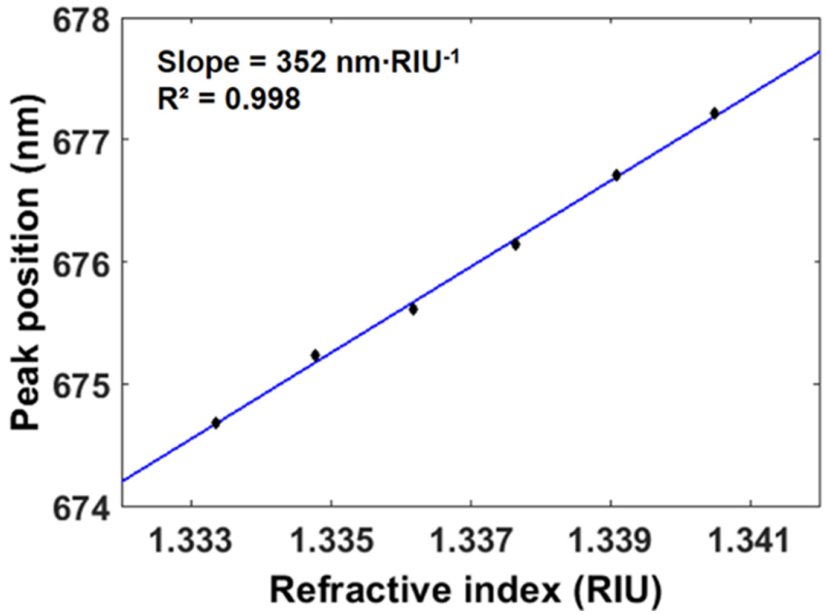

Figure A.2: Shifts of PSiM reflectance (measured at peak wavelength on long wavelength side of resonance) after adding different concentrations of glucose solution, as measured by a spectrometer. A linear fit is shown (blue line).

Figure A.2 shows a linear relationship between the spectral shifts of the PSiM measured by the spectrometer after adding different concentrations of glucose solution (0 – 50 g·L^{-1}). The refractive indices of the glucose solutions with different concentrations are determined based on data reported in [136].A linear fit to the data suggests that the RIU sensitivity of the PSiM is approximately 350 nm·RIU^{-1}.

A.3 Smartphone image and data processing

A.4 Stability of the PSiM-smartphone biosensor system

In order to assess the stability and reproducibility of the PSiM-smartphone biosensor sys-

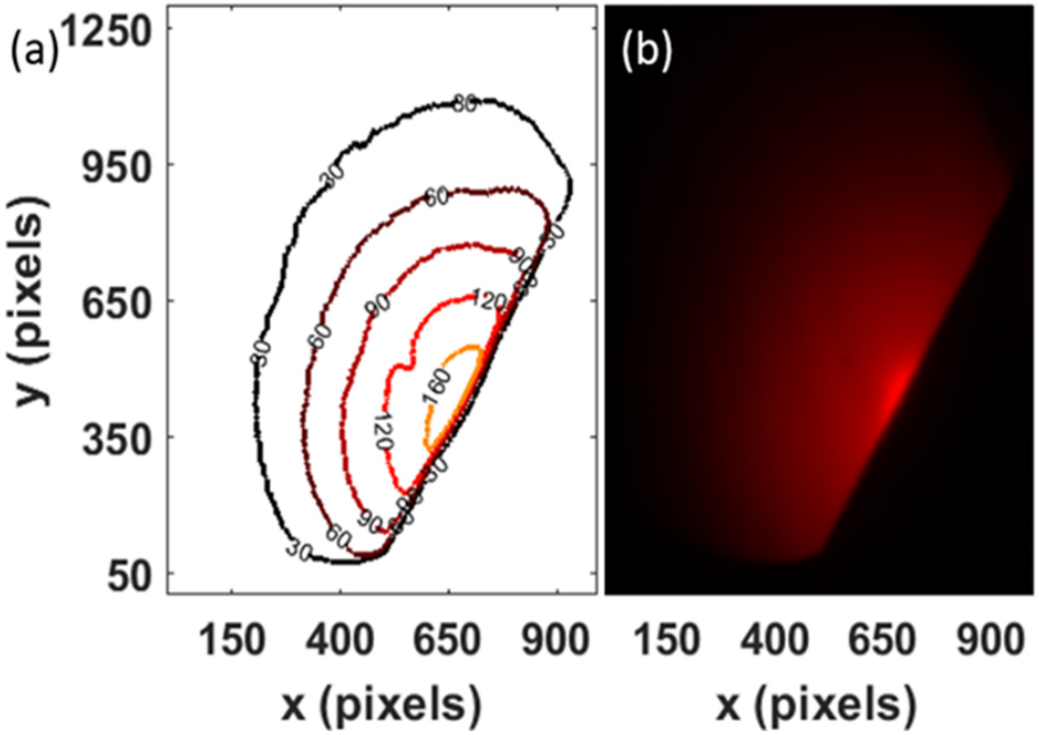

Figure A.3: (a) R value contour map of a PSiM sample extracted from one frame of a video recorded by the smartphone sensing platform. (b) Image of PSiM sample (i.e., video frame) corresponding to the R value contour map shown in (a). The sharp interface between the red and black regions of the image that leads to a strong gradient in the contour map is due to the presence of the black tape that blocks a portion of the emitted light from the smartphone LED.

tem, three repeat measurements were taken for each experimental condition of the PSiM. Each measurement comprised a 1 min video of the PSiM followed by a 1 min video of the control sample. The PSiM and control samples were removed and then reinserted into the 3D printed box holding the smartphone between each set of measurements. Figure S4 shows the S value as a function of time during each of the three videos for the PSiM ("measure") and control bare silicon ("control") samples. We note that the time duration for removing and reinserting the samples is very short compared to the time duration for which the sample is measured. Good stability and reproducibility is demonstrated as the samples are taken in and out of the box. The percent intensity changes between measure 1 and measure 2, measure 2 and measure 3, and measure 3 and measure 1 are all less than

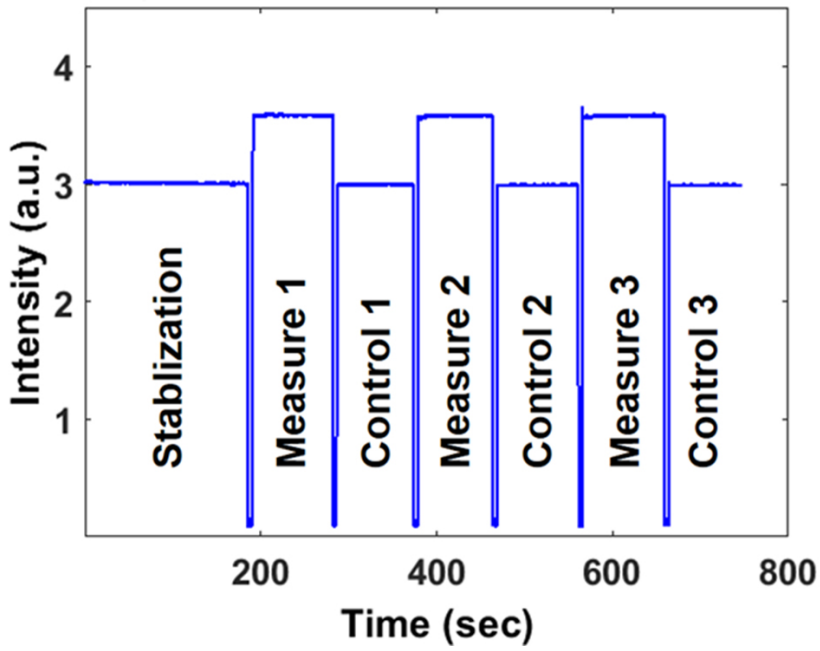

Figure A.4: Smartphone measured intensity as a function of time for three independent measurements of a PSiM and control bare silicon sample. Good stability of the system is demonstrated when samples are removed and subsequently reinserted into the 3D printed box holding the smartphone.

0.1%.

A.5 Root mean square deviation and Bland-Altman analysis

Root-mean-square deviation:

$$\sigma = \sqrt{\frac{1}{n}\sum_{n=1}^{n}(\lambda_i - \hat{\lambda})^2} \qquad \text{(Eq A.3)}$$

In Eq A.3, λ is the peak wavelength of the PSiM on the long wavelength side of the resonance as calculated from the linear fit in Fig 3.9(b), and λ_i is the peak wavelength measured by the spectrometer. Three independent measurements are taken after each APTES exposure to the PSiM, and 21 total values (i.e., n =21) are considered in the calculation.A Bland-Altman plot was generated by transforming the relative intensities measured by the

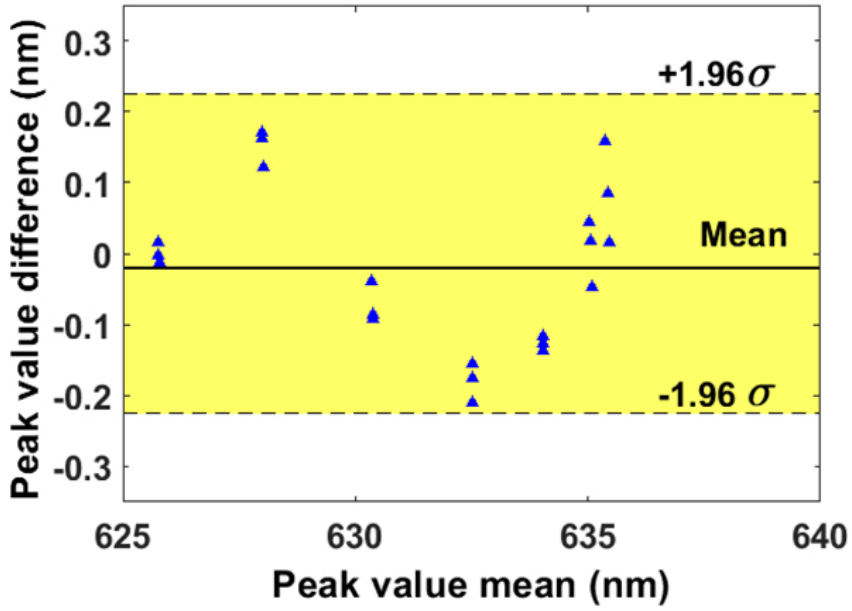

Figure A.5: Bland-Altman plot of smartphone and spectrometer measurements of PSiM exposed to APTES (data shown in Figure 3.9). The dotted lines enclosing the yellow region represent the 95% confidence interval for the peak value difference.

smartphone to peak wavelengths using the linear fit in Fig 3.9 (b), and then these values are compared to the peak wavelengths measured by the spectrometer.

A.6 Spectrometer measurements of streptavidin attachment

A.7 Streptavidin sensing with separate PSiM samples

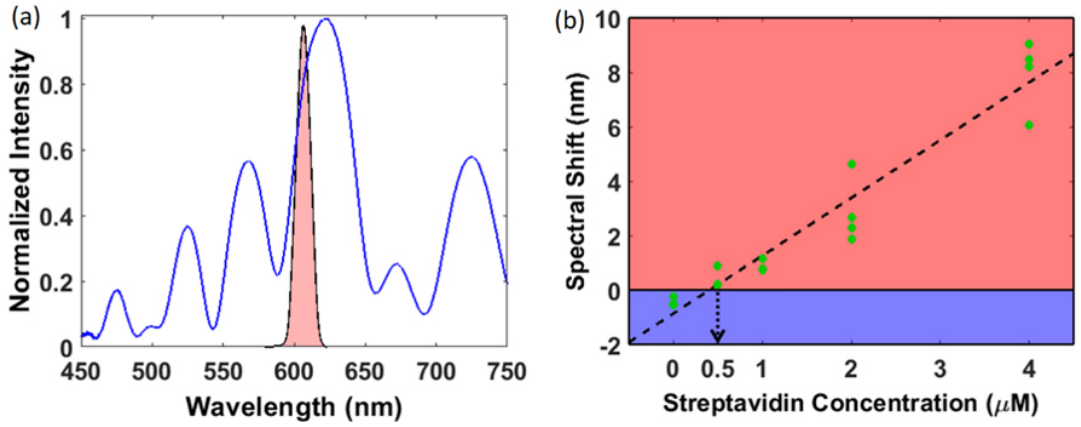

Figure A.6: (a) Spectrometer measurement of the reflectance spectrum of the PSiM before adding streptavidin (blue curve) and the smartphone light transmitted through filter (red shaded area). Note that the relative position of the reflectance spectrum and bandpass of the filter may be slightly different for the smartphone measurement. (b) Spectral shift of PSiM after adding different concentrations of streptavidin molecules, as measured by a spectrometer with reference to the reflectance peak on the long wavelength side of the microcavity resonance. With a concentration of 0 μM (i.e., no streptavidin molecules and only solvent exposed to the sample), there is a slight blueshift of the spectrum, suggesting minor instability of the PSiM surface functionalization during the experiment. The data suggest a linear relationship between the PSiM response and streptavidin concentration exposed to the PSiM in the reported concentration range.

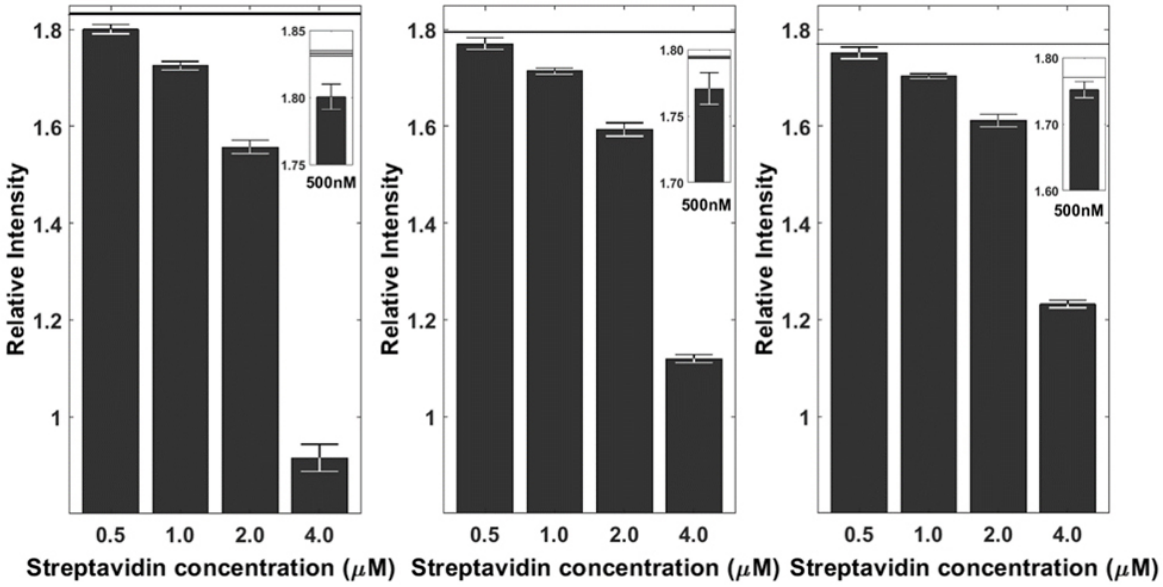

Figure A.7: Streptavidin sensing experiment carried out on three separate PSiM samples. The measurements show the same trend in the relative intensity changes for different concentrations of streptavidin solutions exposed to the different samples. Error bars represent $\pm$ 3σ for the three smartphone relative intensity measurements taken after each PSiM is exposed to a given concentration of streptavidin molecules. Differences in the measured relative intensity values between the different PSiM samples is explained by the different initial microcavity resonance positions with respect to the bandpass of the filter used in the smartphone sensing system. The thickness of the solid line at the top of each graph represents the 3σ value of the relative intensity of the PSiM measured before streptavidin infiltration. For all three PSiM samples, a streptavidin concentration of 500 nM can be clearly distinguished (insets).

Appendix B

B.1 Flow cell experiment

B.1.1 Experiment

To facilitate the mass transportation, flow-through membrane has been reported in our group.[111] The process reported needs oxidation of PSi to prevent the corrosion from the basic photoresist developer solution. However, hydrosilylation require Si-H terminated PSi surface. We tried to remove the oxidation layer from the PSi membrane using 2.5% HF, but the stress generated during the solvent evaporation shattered the film. Here, we used a different process for PSi membrane preparation and surface modification. It is worth noting that the ND modification and the peptides are stable enough to withstand the corrosion of HF, so we lifted off the functionalized PSi film and transferred it to the silicon with openings, and then attach the PDMS flow channel to the Si piece. The detailed procedures are listed as following.

The silicon pieces with 1mm×1mm square holes were rinsed in NaOH (1 M), cleaned with water, and dried under nitrogen stream. Then oxidized in the 800 °C oven for 30 min; and treated with oxygen plasma for 20 sec together with PDMS microchannel. The PDMS microchannels were then glued to the silicon pieces with the help of liquid PDMS and incubated in 120 °C oven for 4 h. A representative example is shown in Figure B.1 a(1).

The PSi microcavities were fabricated and functionalized following the procedures detailed in section 4.6.1. The functionalized silicon wafer was cut into pieces of 1.8 × 1.8 cm squares. Copper(I)-catalyzed click reaction is then performed to attach the CBP to the ND-modified PSi squares. The procedures for the click reaction are detailed in section 4.6.2. After click reaction, the samples were rinsed with DMSO, followed by anhydrous ethanol and DI water, and soaked in 0.5 mM HCl for 30 min to remove residual copper in the pores. The samples were then cleaned with DI water and anhydrous ethanol, and dried

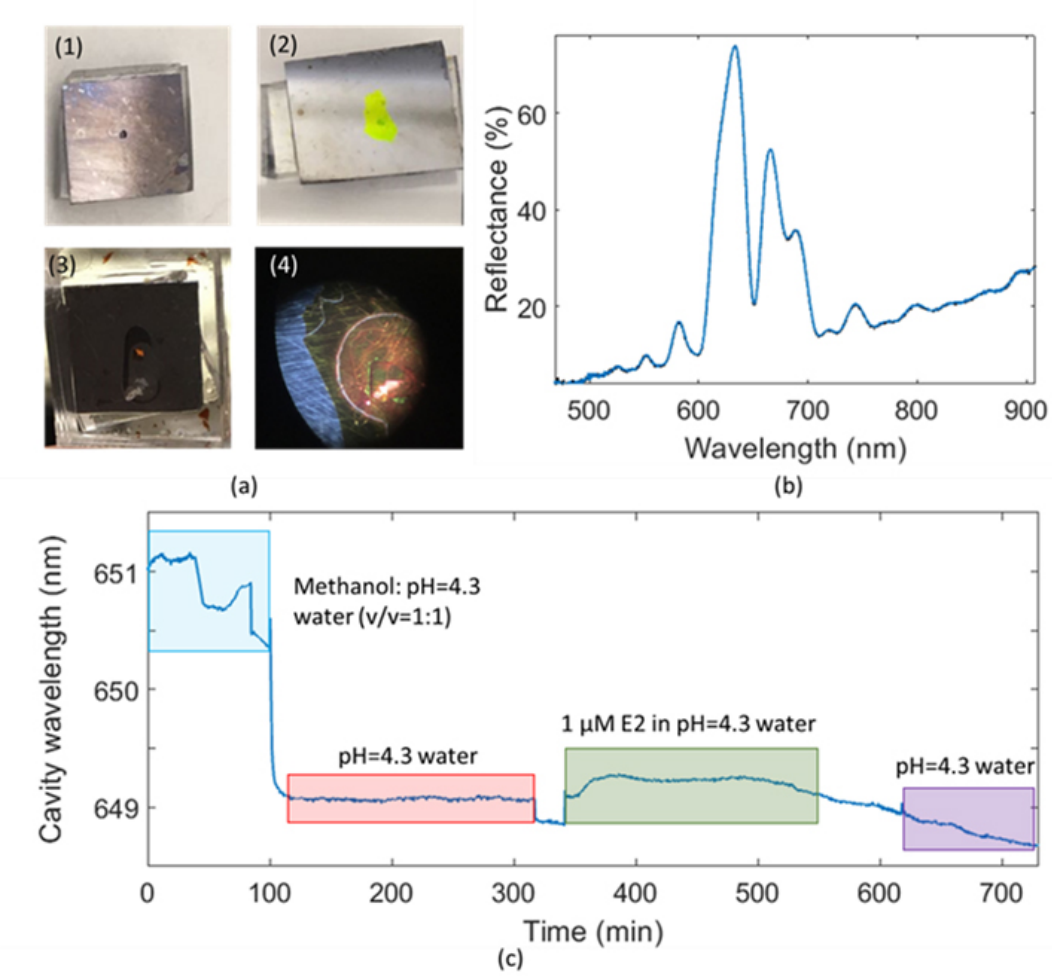

Figure B.1: (a) (1). The silicon with open holes and PDMS in the back. (2). PSi film transferred on top of the silicon chip with holes. (3). The back-view of the flow through membrane cell. (4). The microscope image of the PSi membrane. (15×) (b) A typical reflectance spectrum obtained during the solution pumping through the flow cell. (c) The spectral shift vs time plot during the flow-through experiment.

under a stream of nitrogen. FTIR spectroscopy measurements are carried out to confirm the attachment of the CBP.

After the peptide binding, the PSi square was attached to the etching cell. 15% ethanolic HF solution was added to the etching cell. (**HF is an extremely dangerous chemical and should always be handled with the utmost caution.**) A current density of 300 $mA{\cdot}cm^{-2}$ was applied for 10 s, followed by 150 $mA{\cdot}cm^{-2}$, 2 s for 5 times. After cleaning the HF

waste, the detached film was transferred to a beaker filled with clean water. The silicon pieces with holes and PDMS backside were used to pick the functionalized PSi up and dry in air. A typical device at this step was shown in Fig B.1 a(2). The half-cell was then treated with O_2 plasma (with the PSi film covered), and attached to the top PDMS flow channel with the help of liquid PDMS. (The backside-view image is shown in Figure B.1 a(3)).

We noted only one side of the PSi membrane has surface functionalization, so the flow through experiment was run in a weak acidic condition (pH = 4.3) to prevent PSi corrosion. A solution of ethanol and water of 1:1 volume ratio was first pumped through the flow-through channel at a rate of 1μL/min to wet the membrane and check for leakage. Followed by a solution of pH = 4.3 solution flushing through the channel (1μL/min) to get the system to base line. When the system was fully stabilized, 1 μM CHIKV E2 protein was pumped through the flow cell at a rate of 1μL/min for 60 min, then slowed down to 0.5μL/min for the purpose of saving analytes. After the E2 injection, a solution of pH= 4.3 solution was injected to the flow cell (at the rate of 1μL/min) to wash off the unbounded molecules.

B.1.2 Result and analysis

Fig B.1(b) shows a typical spectrum during the flow cell experiment. The cavity position (center dip of the spectrum) was used to monitor the flow through process. As shown in Figure B.1 (c), after the water injection, the spectra underwent a blueshift and gradually stabilized. (Because ethanol has a higher refractive index than water) When 1 μM of E2 was pumped into the flow cell, a gradual redshifting was observed in the sensorgram. When the system reached equilibrium, a total redshift of 0.2nm was observed. After that, a gradual blueshifting is observed, and the baseline drifting may be attributed to the PSi corrosion. (E2 binding may change the local charge distribution of the PSi)

Though the E2 binding is observed in the flow cell experiment, the success (samples kept intact during the process) rate is low. During the flow cell fabrication, the stress control of film played an important role. Figure B.1 a(4) shows the microscope image of a flow through membrane, which shattered when the top PDMS was attached.

B.2 PSi surface dual functionalization

To get water passing through the hydrophobic ND modified PSi, a hydrophilic undecanoic acid modified layer was added underneath. As discussed in 1.3.2(b), the PSi double-layer structures could give distinguishable signals from both layers through FFT. The detailed sample preparation steps are listed as follows.

A PSi single layer was fabricated through anodic etching of p-type silicon wafers in a solution of 15% ethanoic HF solution (as specified earlier). To ensure there is no narrowing of the pore opening at the top surface of wafer, an etching current density of 70 $mA \cdot cm^{-2}$ is applied to the wafer for 100 s serve as a sacrificial layer and it is then dissolved in 1 M NaOH and rinsed with ethanol and DI water. Next, the PSi single layer is etched using a current density of 80 $mA \cdot cm^{-2}$ (H) for 100 sec. The freshly etched PSi single layer is then modified with 1,8-nonadiyne, through thermal hydrosilylation. The detailed steps are stated in in section 4.6.1. After ND modification, the PSi was cut into pieces of 1.8 $\times$ 1.8 cm squares, then attached to the etching cell. 15% ethanolic HF solution was added to the etching cell. A current density of 60 $mA \cdot cm^{-2}$ is applied for 50 sec. A second hydrosilylation with UA was performed to create a flow with a hydrophobicity gradient. The procedures for UA hydrosilylation are detailed in section 3.4.1. After the functionalization, the CBP was clicked to PSi sample similar to the procedure detailed in 4.6.2. The as-etched PSi piece was then cleaned with ethanol and water and dry under

the nitrogen stream. The samples were then exposed to 1 μM of E2 in water for 2h, but the contact angle was still around 100 ° demonstrated the strong hydrophobicity of the PSi surface and no significant spectral shifts are observed.

B.3 Surface modification with hydrosilylation

Another approach to overcoming the challenges of the hydrophobic nature of the alkyne-modified PSi surface is to create a more hydrophilic surface. Unlike the alkyne modified surface, azide terminated surface exhibited slightly better hydrophilicity with a contact angle of 75 ° with water, compared the 115 ° water contact angle with ND surface. Thus, alkyne terminated peptides clicking with azide terminated PSi was carried out. Before the reaction, the stability of the azide terminated PSi were examined by incubating the samples in water.

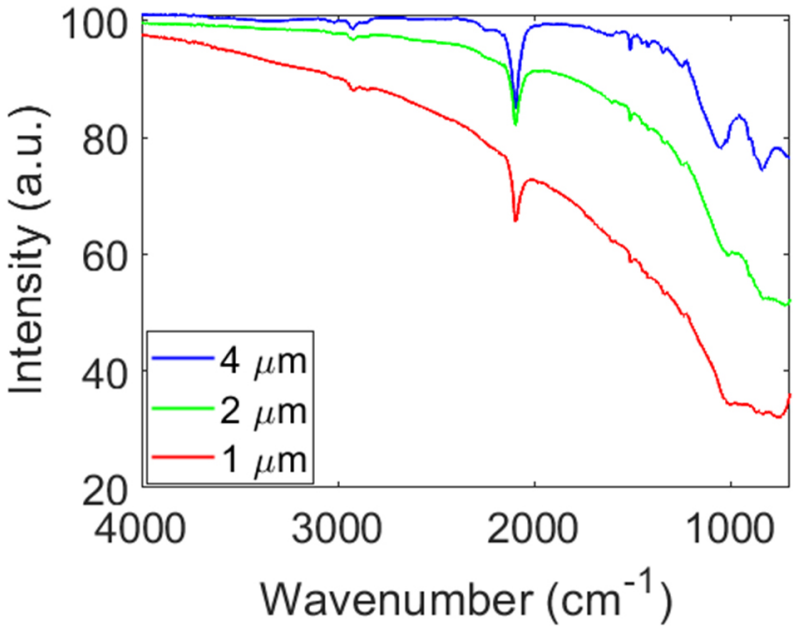

Figure B.2: The FTIR spectra of the PSi Sample of 4 μm, 2 μm, 1 μm after hydrosilylation reaction.

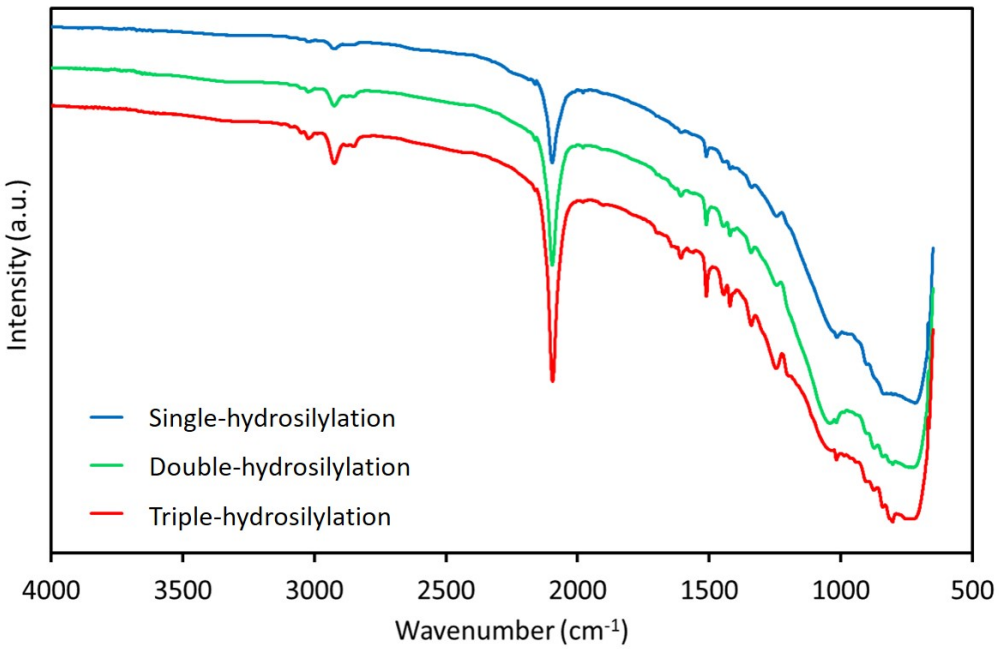

Figure B.3: The FTIR Spectra of 2 μm-thick PSi samples modified by single, double and triple rounds of hydrosilylation.

The azide modified surface was prepared by hydrosilylation reaction. The FTIR were taken after the reactions, as shown in Figure B.2. All three curves show sharp dip around 2100 cm^{-1} indicating the presence of azide. Because different layer thickness will form different fringe pattern in the spectrum, it's hard to get the FTIR spectral curves calibrated. To get a better azide coverage, multiple reactions were also explored. Figure B.3 exhibits the FTIR Spectra of 2 μm-thick PSi samples modified by single, double and triple rounds of reactions. It clearly shows multiple rounds of hydrosilylation increase the azide coverage. 4 μm -thick and 1 μm -thick sample displayed the same trend.

After azide modification, the PSi samples are incubated in DI water 2h each time for 2-3 times. Figure B.4 recorded the refractive index changes of the PSi for the first two 2h incubations. As shown in the chart, thinner PSi samples and multiple exposures provide the PSi sample with a better protection. However, the improvement start to shrink as we compare 1 μm-thick PSi with double and triple rounds of hydrosilylation, or 1 μm-thick and 3

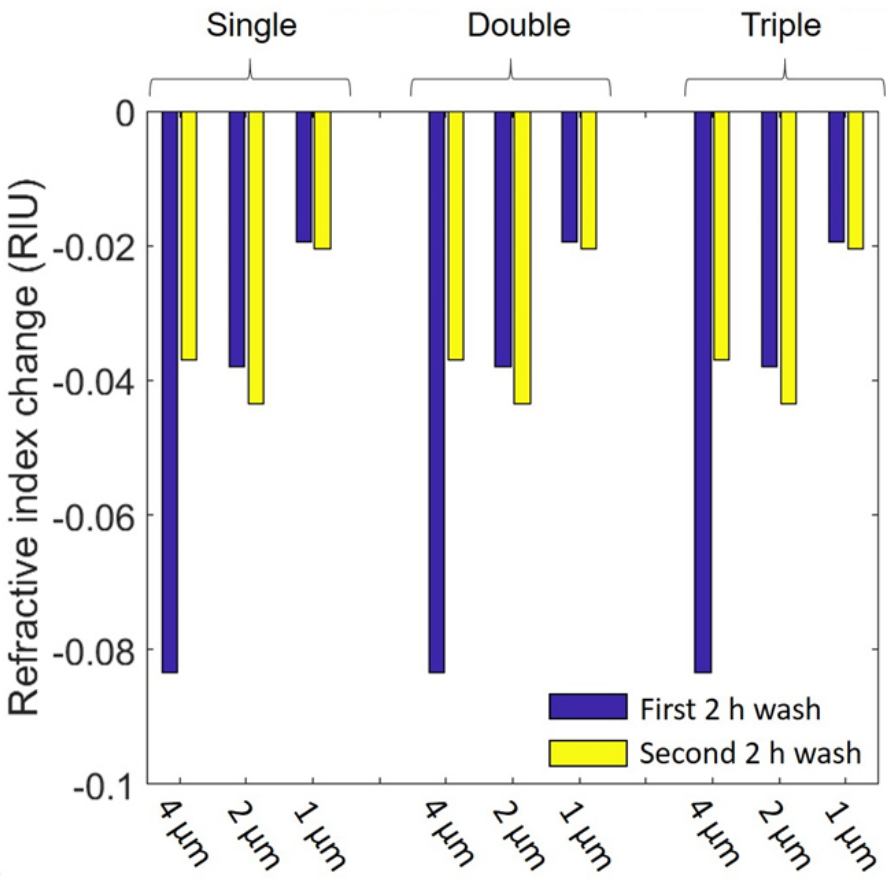

Figure B.4: Refractive index changes of azide modified 4 μm, 2 μm, 1 μm PSi samples, after first 2h and second 2h DI water rinse.

μm-thick PSi samples with both triple- hydrosilylation. Therefore, the material loss cannot be completely prevented with decreasing PSi thickness or increasing number of hydrosilylation. We attributed this "intrinsic" loss to the unavoidable oxidation occurred during the hydrosilylation process. Though still facing stability issues, we performed a preliminary test on 1 μM azide terminated samples for CHIKV E2 protein sensing. Considering the potential pores shrinking caused by the azide terminated compound attachment, KOH were used to enlarge the pores. Freshly etched PSi were rinsed in 1.5 mM ethanoic KOH (Ethanol: DI water =5:1 v/v) for 5min, immediately followed by a thorough cleaning before hydrosilylation. The sensing results are shown in Figure B.5. Comparatively, the sample with enlarged pores showed a large shift of 3.9 nm when exposing peptide modified surface

to 2 μM E2, which may indicate more E2 protein capture. The shift is larger than 1.7 nm - the one obtained from vacuum infiltration method. However, to confirm the result, more repeats and control experiments are needed.

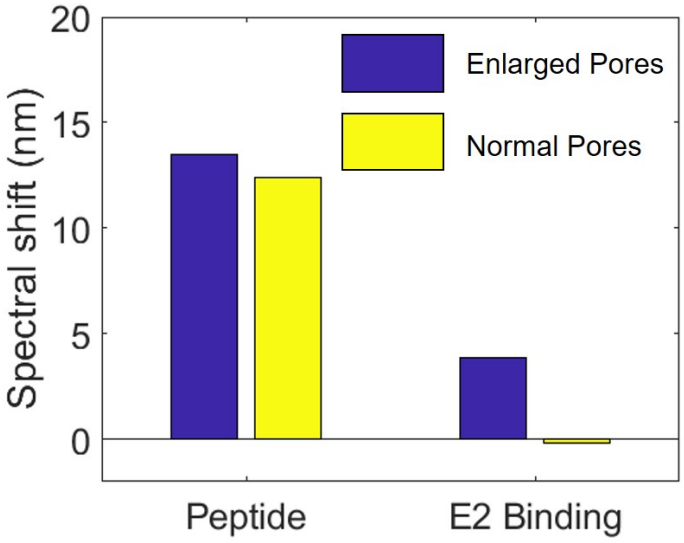

Figure B.5: The results of CHIKV E2 protein sensing using 1 μm-thick PSi sample with KOH enlarged pores (purple) and normal pores (yellow).

References

[1] Markets and markets. Biosensors market by type (sensor patch and embedded de-vice), product (wearable and nonwearable), technology (electrochemical and opti-cal), application (poc, home diagnostics, research lab, food & beverages), and geog-raphy - global forecast to 2024, 2019.

[2] Pavel Damborský, Juraj Švitel, and Jaroslav Katrlík. Optical biosensors. *Essays in biochemistry*, 60(1):91–100, 2016.

[3] Amir Syahir, Kenji Usui, Kin-ya Tomizaki, Kotaro Kajikawa, and Hisakazu Mihara. Label and label-free detection techniques for protein microarrays. *Microarrays*, 4(2):228–244, 2015.

[4] Pongali Raghavendra and Thammineni Pullaiah. *Advances in Cell and Molecular Diagnostics*. Academic Press, 2018.

[5] Benjamin Caballero, Luiz C Trugo, and Paul M Finglas. *Encyclopedia of food sciences and nutrition*. Academic, 2003.

[6] John M Walker. *The ELISA guidebook*, volume 516, pages 1–421. Springer, 2009.

[7] Yuan Gao, Yingzhu Zhou, and Rona Chandrawati. Metal and metal oxide nanoparticles to enhance the performance of enzyme-linked immunosorbent assay (elisa). *ACS Applied Nano Materials*, 3(1):1–21, 2019.

[8] jiřı Homola, Sinclair S Yee, and Günter Gauglitz. Surface plasmon resonance sensors. *Sensors and Actuators B: Chemical*, 54(1-2):3–15, 1999.

[9] Xuyen D Hoa, AG Kirk, and M Tabrizian. Towards integrated and sensitive surface plasmon resonance biosensors: a review of recent progress. *Biosensors and bioelectronics*, 23(2):151–160, 2007.

[10] Takuo Akimoto, Satoshi Sasaki, Kazunori Ikebukuro, and Isao Karube. Effect of incident angle of light on sensitivity and detection limit for layers of antibody with surface plasmon resonance spectroscopy. *Biosensors and Bioelectronics*, 15(7-8):355–362, 2000.

[11] Zongfu Yu and Shanhui Fan. Extraordinarily high spectral sensitivity in refractive index sensors using multiple optical modes. *Optics express*, 19(11):10029–10040, 2011.

[12] PP Markowicz, WC Law, A Baev, PN Prasad, S Patskovsky, and AV Kabashin. Phase-sensitive time-modulated surface plasmon resonance polarimetry for wide dynamic range biosensing. *Optics express*, 15(4):1745–1754, 2007.

[13] AV Kabashin, P Evans, S Pastkovsky, W Hendren, GA Wurtz, R Atkinson, R Pollard, VA Podolskiy, and AV Zayats. Plasmonic nanorod metamaterials for biosensing. *Nature materials*, 8(11):867–871, 2009.

[14] Paras N Prasad. *Introduction to biophotonics*. John Wiley & Sons, 2004.

[15] Zhenxin Wang and Lina Ma. Gold nanoparticle probes. *Coordination Chemistry Reviews*, 253(11-12):1607–1618, 2009.

[16] Kuan-I Chen, Bor-Ran Li, and Yit-Tsong Chen. Silicon nanowire field-effect transistor-based biosensors for biomedical diagnosis and cellular recording investigation. *Nano today*, 6(2):131–154, 2011.

[17] Anran Gao, Na Lu, Yuchen Wang, Pengfei Dai, Tie Li, Xiuli Gao, Yuelin Wang, and Chunhai Fan. Enhanced sensing of nucleic acids with silicon nanowire field effect transistor biosensors. *Nano letters*, 12(10):5262–5268, 2012.

[18] Xuan PA Gao, Gengfeng Zheng, and Charles M Lieber. Subthreshold regime has the optimal sensitivity for nanowire fet biosensors. *Nano letters*, 10(2):547–552, 2010.

[19] SM Sherif, MY Elsayed, LA Shahada, and MA Swillam. Vertical silicon nanowire-based racetrack resonator optical sensor. *Applied Physics A*, 125(11):769, 2019.

[20] Damiano Verardo, Frida W Lindberg, Nicklas Anttu, Cassandra S Niman, Mercy Lard, Aleksandra P Dabkowska, Tommy Nylander, Alf Månsson, Christelle N Prinz, and Heiner Linke. Nanowires for biosensing: lightguiding of fluorescence as a function of diameter and wavelength. *Nano letters*, 18(8):4796–4802, 2018.

[21] Adam Bolotsky, Derrick Butler, Chengye Dong, Katy Gerace, Nicholas R Glavin, Christopher Muratore, Joshua A Robinson, and Aida Ebrahimi. Two-dimensional materials in biosensing and healthcare: from in vitro diagnostics to optogenetics and beyond. *ACS nano*, 13(9):9781–9810, 2019.

[22] Sofia Arshavsky-Graham, Naama Massad-Ivanir, Ester Segal, and Sharon Weiss. Porous silicon-based photonic biosensors: Current status and emerging applications. *Analytical Chemistry*, 91(1):441–467, 2019.

[23] Victor S-Y Lin, Kianoush Motesharei, Keiki-Pua S Dancil, Michael J Sailor, and M Reza Ghadiri. A porous silicon-based optical interferometric biosensor. *Science*, 278(5339):840–843, 1997.

[24] Stefano Mariani, Laura Pino, Lucanos M Strambini, Lorena Tedeschi, and Giuseppe Barillaro. 10,000-fold improvement in protein detection using nanostructured porous silicon interferometric aptasensors. *ACS sensors*, 1(12):1471–1479, 2016.

[25] Lab tests online website. Point-of-care testing : What is point-of-care testing?, Dec 30, 2015.

[26] Adam J Singer, Joshua Ardise, Janet Gulla, and Julie Cangro. Point-of-care testing reduces length of stay in emergency department chest pain patients. *Annals of emergency medicine*, 45(6):587–591, 2005.

[27] Victoria Hardy, William Alto, Gina A Keppel, Laura-Mae Baldwin, and Matthew Thompson. Which point-of-care tests would be most beneficial to add to clinical practice?: Findings from a survey of 3 family medicine clinics in the united states. *Point of care*, 16(4):168, 2017.

[28] Sherine F Cheung, Samantha KL Cheng, and Daniel T Kamei. Paper-based systems for point-of-care biosensing. *Journal of laboratory automation*, 20(4):316–333, 2015.

[29] Ruihua Tang, Hui Yang, Jane Ru Choi, Yan Gong, Jie Hu, Shangsheng Feng, Belinda Pingguan-Murphy, Qibing Mei, and Feng Xu. Improved sensitivity of lateral flow assay using paper-based sample concentration technique. *Talanta*, 152:269–276, 2016.

[30] D. N. Breslauer, R. N. Maamari, N. A. Switz, W. A. Lam, and D. A. Fletcher. Mobile phone based clinical microscopy for global health applications. *Plos One*, 4(7), 2009.

[31] D. Tseng, O. Mudanyali, C. Oztoprak, S. O. Isikman, I. Sencan, O. Yaglidere, and A. Ozcan. Lensfree microscopy on a cellphone. *Lab on a Chip*, 10(14):1787–1792, 2010.

[32] D. Gallegos, K. D. Long, H. J. Yu, P. P. Clark, Y. X. Lin, S. George, P. Nath, and B. T. Cunningham. Label-free biodetection using a smartphone. *Lab on a Chip*, 13(11):2124–2132, 2013.

[33] C. J. Zhang, G. Cheng, P. Edwards, M. D. Zhou, S. Y. Zheng, and Z. W. Liu. G-fresnel smartphone spectrometer. *Lab on a Chip*, 16(2):246–250, 2016.

[34] H. J. Yu, Y. F. Tan, and B. T. Cunningham. Smartphone fluorescence spectroscopy. *Analytical Chemistry*, 86(17):8805–8813, 2014.

[35] Y. Liu, Q. Liu, S. M. Chen, F. Cheng, H. Q. Wang, and W. Peng. Surface plasmon resonance biosensor based on smart phone platforms. *Scientific Reports*, 5, 2015.

[36] P. Preechaburana, M. C. Gonzalez, A. Suska, and D. Filippini. Surface plasmon resonance chemical sensing on cell phones. *Angewandte Chemie-International Edition*, 51(46):11585–11588, 2012.

[37] B. Berg, B. Cortazar, D. Tseng, H. Ozkan, S. Feng, Q. S. Wei, R. Y. L. Chan, J. Burbano, Q. Farooqui, M. Lewinski, D. Di Carlo, O. B. Garner, and A. Ozcan. Cellphone-based hand-held microplate reader for point-of-care testing of enzyme-linked immunosorbent assays. *Acs Nano*, 9(8):7857–7866, 2015.

[38] A Uhlir Jr. Electrolytic shaping of germanium and silicon. *Bell System Technical Journal*, 35(2):333–347, 1956.

[39] Leigh T Canham. Silicon quantum wire array fabrication by electrochemical and chemical dissolution of wafers. *Applied physics letters*, 57(10):1046–1048, 1990.

[40] G Bomchil, A Halimaoui, and R Herino. Porous silicon: the material and its applications to soi technologies. *Microelectronic Engineering*, 8(3-4):293–310, 1988.

[41] C. Pacholski, M. Sartor, M. J. Sailor, F. Cunin, and G. M. Miskelly. Biosensing using porous silicon double-layer interferometers: Reflective interferometric fourier transform spectroscopy. *Journal of the American Chemical Society*, 127(33):11636–11645, 2005.

[42] Yang Jiao and Sharon M Weiss. Design parameters and sensitivity analysis of polymer-cladded porous silicon waveguides for small molecule detection. *Biosensors and Bioelectronics*, 25(6):1535–1538, 2010.

[43] Guoguang Rong, Ali Najmaie, John E Sipe, and Sharon M Weiss. Nanoscale porous silicon waveguide for label-free dna sensing. *Biosensors and Bioelectronics*, 23(10):1572–1576, 2008.

[44] Eduardo Lorenzo, Claudio J Oton, Néstor E Capuj, Mher Ghulinyan, Daniel Navarro-Urrios, Zeno Gaburro, and Lorenzo Pavesi. Porous silicon-based rugate filters. *Applied optics*, 44(26):5415–5421, 2005.

[45] Han-Jung Kim, Young-You Kim, and Ki-Won Lee. Multiparametric sensor based on dbr porous silicon for detection of ethanol gas. *Current Applied Physics*, 10(1):181–183, 2010.

[46] Huimin Ouyang, Christopher C Striemer, and Philippe M Fauchet. Quantitative analysis of the sensitivity of porous silicon optical biosensors. *Applied Physics Letters*, 88(16):163108, 2006.

[47] E Krioukov, Jan Greve, and Cornelis Otto. Performance of integrated optical microcavities for refractive index and fluorescence sensing. *Sensors and Actuators B: Chemical*, 90(1-3):58–67, 2003.

[48] Carl Zeiss Microscopy GmbH. Zeiss product brochure new geminisem family, 2009.

[49] Brendan J Griffin. A comparison of conventional everhart-thornley style and in-lens secondary electron detectors—a further variable in scanning electron microscopy. *Scanning*, 33(3):162–173, 2011.

[50] Tengfei Cao, Yiliang Zhao, and Sharon M. Weiss. *A smartphone compatible colorimetric biosensing system based on porous silicon*, volume 10077 of *SPIE BiOS*. SPIE, 2017.

[51] Tengfei Cao, Yiliang Zhao, Crystal A Nattoo, Rabeb Layouni, and Sharon M Weiss. A smartphone biosensor based on analysing structural colour of porous silicon. *Analyst*, 144(13):3942–3948, 2019.

[52] Vladimir Gubala, Leanne F Harris, Antonio J Ricco, Ming X Tan, and David E Williams. Point of care diagnostics: status and future. *Analytical chemistry*, 84(2):487–515, 2012.

[53] Dennis Fitzpatrick. *Implantable electronic medical devices*. Elsevier, 2014.

[54] Xiayu Xu, Altug Akay, Huilin Wei, ShuQi Wang, Belinda Pingguan-Murphy, Björn-Erik Erlandsson, XiuJun Li, WonGu Lee, Jie Hu, and Lin Wang. Advances in smartphone-based point-of-care diagnostics. *Proceedings of the IEEE*, 103(2):236–247, 2015.

[55] V. M. Winnie, S. Romaric, M. W. Pauline, and B. Samuel. Building on progress: Infrastructure development still a major challenge in africa, 2016.

[56] H. Y. Zhu, S. Mavandadi, A. F. Coskun, O. Yaglidere, and A. Ozcan. Optofluidic fluorescent imaging cytometry on a cell phone. *Analytical Chemistry*, 83(17):6641–6647, 2011.

[57] Q. S. Wei, H. F. Qi, W. Luo, D. Tseng, S. J. Ki, Z. Wan, Z. Gorocs, L. A. Bentolila, T. T. Wu, R. Sun, and A. Ozcan. Fluorescent imaging of single nanoparticles and viruses on a smart phone. *Acs Nano*, 7(10):9147–9155, 2013.

[58] J. Frean. Microscopic images transmitted by mobile cameraphone. *Transactions of the Royal Society of Tropical Medicine and Hygiene*, 101(10):1053–1054, 2007.

[59] M. Zimic, J. Coronel, R. H. Gilman, C. G. Luna, W. H. Curioso, and D. A. J. Moore. Can the power of mobile phones be used to improve tuberculosis diagnosis in developing countries? *Transactions of the Royal Society of Tropical Medicine and Hygiene*, 103(6):638–640, 2009.

[60] K. D. Long, E. V. Woodburn, H. M. Le, U. K. Shah, S. S. Lumetta, and B. T. Cunningham. Multimode smartphone biosensing: the transmission, reflection, and intensity spectral (tri)-analyzer. *Lab on a Chip*, 17(19):3246–3257, 2017.

[61] B. Y. Chang. Smartphone-based chemistry instrumentation: Digitization of colorimetric measurements. *Bulletin of the Korean Chemical Society*, 33(2):549–552, 2012.

[62] V. Oncescu, D. O'Dell, and D. Erickson. Smartphone based health accessory for colorimetric detection of biomarkers in sweat and saliva. *Lab on a Chip*, 13(16):3232–3238, 2013.

[63] V. Oncescu, M. Mancuso, and D. Erickson. Cholesterol testing on a smartphone. *Lab on a Chip*, 14(4):759–763, 2014.

[64] S. Lee, V. Oncescu, M. Mancuso, S. Mehta, and D. Erickson. A smartphone platform for the quantification of vitamin d levels. *Lab on a Chip*, 14(8):1437–1442, 2014.

[65] Z. D. Lu, D. O'Dell, B. Srinivasan, E. Rey, R. S. Wang, S. Vemulapati, S. Mehta, and D. Erickson. Rapid diagnostic testing platform for iron and vitamin a deficiency. *Proceedings of the National Academy of Sciences of the United States of America*, 114(51):13513–13518, 2017.

[66] M. Zangheri, L. Cevenini, L. Anfossi, C. Baggiani, P. Simoni, F. Di Nardo, and A. Roda. A simple and compact smartphone accessory for quantitative chemiluminescence-based lateral flow immunoassay for salivary cortisol detection. *Biosensors & Bioelectronics*, 64:63–68, 2015.

[67] D. M. Zhang and Q. J. Liu. Biosensors and bioelectronics on smartphone for portable biochemical detection. *Biosensors & Bioelectronics*, 75:273–284, 2016.

[68] Yiliang Zhao, Girija Gaur, Scott T. Retterer, Paul E. Laibinis, and Sharon M. Weiss. Flow-through porous silicon membranes for real-time label-free biosensing. *Analytical Chemistry*, 88(22):10940–10948, 2016.

[69] T. H. Wu, C. C. Chang, J. Vaillant, A. Bruyant, and C. W. Lin. Dna biosensor combining single-wavelength colorimetry and a digital lock-in amplifier within a smartphone. *Lab on a Chip*, 16(23):4527–4533, 2016.

[70] Tahmid H Talukdar, Bria McCoy, Sarah K Timmins, Taufiquar Khan, and Judson D Ryckman. Hyperchromatic structural color for perceptually enhanced sensing by the naked eye. *Proceedings of the National Academy of Sciences*, 117(48):30107–30117, 2020.

[71] Tengfei Cao, Rabeb Layouni, Matthew Coppock, Paul Laibinis, and Sharon Weiss. *Use of peptide capture agents in porous silicon biosensors*, volume 11258 of *SPIE BiOS*. SPIE, 2020.

[72] Ingrid Bazin, Scherrine A Tria, Akhtar Hayat, and Jean-Louis Marty. New biorecognition molecules in biosensors for the detection of toxins. *Biosensors and Bioelectronics*, 87:285–298, 2017.

[73] Leland C Clark Jr and Champ Lyons. Electrode systems for continuous monitoring in cardiovascular surgery. *Annals of the New York Academy of sciences*, 102(1):29–45, 1962.

[74] Haoran Liu, Jun Ge, Eugene Ma, and Lei Yang. *Advanced biomaterials for biosensor and theranostics*, pages 213–255. Elsevier, 2019.

[75] Jiri Janata. Immunoelectrode. *Journal of the American Chemical Society*, 97(10):2914–2916, 1975.

[76] Matthew B. Coppock, Candice R. Warner, Brandi Dorsey, Joshua A. Orlicki, Deborah A. Sarkes, Bert T. Lai, Suresh M. Pitram, Rosemary D. Rohde, Jacquie Malette, Jeré A. Wilson, Paul Kearney, Kenneth C. Fang, Scott M. Law, Sherri L. Candelario, Blake Farrow, Amethist S. Finch, Heather D. Agnew, James R. Heath, and Dimitra N. Stratis-Cullum. Protein catalyzed capture agents with tailored performance for in vitro and in vivo applications. *Peptide Science*, 108(2):e22934, 2017.

[77] Matthew B. Coppock, Deborah A. Sarkes, Margaret M. Hurley, and Dimitra N. Stratis-Cullum. *Peptide-based antibody alternatives for biological sensing in austere environments*, volume 10081 of *SPIE BiOS*. SPIE, 2017.

[78] Shiping Song, Lihua Wang, Jiang Li, Chunhai Fan, and Jianlong Zhao. Aptamer-based biosensors. *TrAC Trends in Analytical Chemistry*, 27(2):108–117, 2008.

[79] Janusz Wesolowski, Vanina Alzogaray, Jan Reyelt, Mandy Unger, Karla Juarez, Mariela Urrutia, Ana Cauerhff, Welbeck Danquah, Björn Rissiek, and Felix Scheuplein. Single domain antibodies: promising experimental and therapeutic tools in infection and immunity. *Medical microbiology and immunology*, 198(3):157–174, 2009.

[80] Peter J. Hudson and Christelle Souriau. Engineered antibodies. *Nature Medicine*, 9:129, 2003.

[81] Joseph Wang. Dna biosensors based on peptide nucleic acid (pna) recognition layers. a review1this paper was a finalist for the biosensors & bioelectronics award for the most original contribution to the congress.1. *Biosensors and Bioelectronics*, 13(7):757–762, 1998.

[82] Michael Bachmann, Karsten Goede, Annette G Beck-Sickinger, Marius Grundmann, Anders Irbäck, and Wolfhard Janke. Microscopic mechanism of specific peptide adhesion to semiconductor substrates. *Angewandte Chemie International Edition*, 49(49):9530–9533, 2010.

[83] Elias Estephan, Marie-Belle Saab, Vivechana Agarwal, Frédéric J. G. Cuisinier, Christian Larroque, and Csilla Gergely. Peptides for the biofunctionalization of silicon for use in optical sensing with porous silicon microcavities. *Advanced Functional Materials*, 21(11):2003–2011, 2011.

[84] Anna Radzicka and Richard Wolfenden. Rates of uncatalyzed peptide bond hydrolysis in neutral solution and the transition state affinities of proteases. *Journal of the American Chemical Society*, 118(26):6105–6109, 1996.

[85] Roberto De La Rica and Hiroshi Matsui. Applications of peptide and protein-based materials in bionanotechnology. *Chemical Society Reviews*, 39(9):3499–3509, 2010.

[86] Seulki Lee, Jin Xie, and Xiaoyuan Chen. Peptide-based probes for targeted molecular imaging. *Biochemistry*, 49(7):1364–1376, 2010.

[87] Francis Crick. Central dogma of molecular biology. *Nature*, 227(5258):561–563, 1970.

[88] Muriel Amblard, Jean-Alain Fehrentz, Jean Martinez, and Gilles Subra. Methods and protocols of modern solid phase peptide synthesis. *Molecular biotechnology*, 33(3):239–254, 2006.

[89] Patrik Samuelson, Elin Gunneriusson, Per-Åke Nygren, and Stefan Ståhl. Display of proteins on bacteria. *Journal of biotechnology*, 96(2):129–154, 2002.

[90] Sachdev S Sidhu, Henry B Lowman, Brian C Cunningham, and James A Wells. *Phage display for selection of novel binding peptides*, volume 328, pages 333–IN5. Elsevier, 2000.

[91] George P Smith. Phage display: Simple evolution in a petri dish (nobel lecture). *Angewandte Chemie International Edition*, 58(41):14428–14437, 2019.

[92] George P Smith and Valery A Petrenko. Phage display. *Chemical reviews*, 97(2):391–410, 1997.

[93] Dimitra N Stratis-Cullum, Joshua M Kogot, Deborah A Sarkes, Irene Val-Addo, and Paul M Pellegrino. *Bacterial display peptides for use in biosensing applications*, pages 629–642. IntechOpen, 2011.

[94] Ruibao Li, Huiming Huang, Liangzhu Huang, Zhenyu Lin, Longhua Guo, Bin Qiu, and Guonan Chen. Electrochemical biosensor for epidermal growth factor receptor detection with peptide ligand. *Electrochimica Acta*, 109:233–237, 2013.

[95] Junchen Wu, Ying Zou, Chunyan Li, Wilhelm Sicking, Ivo Piantanida, Tao Yi, and Carsten Schmuck. A molecular peptide beacon for the ratiometric sensing of nucleic acids. *Journal of the American Chemical Society*, 134(4):1958–1961, 2012.

[96] Edith Chow and J Justin Gooding. Peptide modified electrodes as electrochemical metal ion sensors. *Electroanalysis: An International Journal Devoted to Fundamental and Practical Aspects of Electroanalysis*, 18(15):1437–1448, 2006.

[97] Gianfranco Giraudi, Laura Anfossi, Claudio Baggiani, Cristina Giovannoli, and Cinzia Tozzi. Solid-phase extraction of ochratoxin a from wine based on a binding hexapeptide prepared by combinatorial synthesis. *Journal of Chromatography A*, 1175(2):174–180, 2007.

[98] Qingtao Liu, Jinfeng Wang, and Ben J Boyd. Peptide-based biosensors. *Talanta*, 136:114–127, 2015.

[99] Silvia Pavan and Federico Berti. Short peptides as biosensor transducers. *Analytical and bioanalytical chemistry*, 402(10):3055–3070, 2012.

[100] Linlin Ma, Fan Yang, and Jie Zheng. Application of fluorescence resonance energy transfer in protein studies. *Journal of molecular structure*, 1077:87–100, 2014.

[101] B. P. Joshi, J. Park, W. I. Lee, and K. H. Lee. Ratiometric and turn-on monitoring for heavy and transition metal ions in aqueous solution with a fluorescent peptide sensor. *Talanta*, 78(3):903–909, 2009.

[102] W. E. Kaman, A. G. Hulst, P. T. W. van Alphen, S. Roffel, M. J. van der Schans, T. Merkel, A. van Belkum, and F. J. Bikker. Peptide-based fluorescence resonance energy transfer protease substrates for the detection and diagnosis of bacillus species. *Analytical Chemistry*, 83(7):2511–2517, 2011.

[103] K. J. Oh, K. J. Cash, and K. W. Plaxco. Excimer-based peptide beacons: A convenient experimental approach for monitoring polypeptide-protein and polypeptide-oligonucleotide interactions. *Journal of the American Chemical Society*, 128(43):14018–14019, 2006.

[104] B. Y. Feng, L. J. Guo, L. H. Wang, F. Li, J. X. Lu, J. M. Gao, C. H. Fan, and Q. Huang. A graphene oxide-based fluorescent biosensor for the analysis of peptide-receptor interactions and imaging in somatostatin receptor subtype 2 overexpressed tumor cells. *Analytical Chemistry*, 85(16):7732–7737, 2013.

[105] K. A. Kilian, T. Boecking, K. Gaus, M. Gal, and J. J. Gooding. Peptide-modified optical filters for detecting protease activity. *Acs Nano*, 1(4):355–361, 2007.

[106] S. S. Sam, Jnjn Chazalviel, Acac Gouget-Laemmel, F. F. Ozanam, A. A. Etcheberry, and N. E. N. Gabouze. Peptide immobilisation on porous silicon surface for metal ions detection. *Nanoscale Research Letters*, 6, 2011.

[107] G. A. Rodriguez, S. R. Hu, and S. M. Weiss. Porous silicon ring resonator for compact, high sensitivity biosensing applications. *Optics Express*, 23(6):7111–7119, 2015.

[108] Mojun Zhu, Maria Z. Lerum, and Wei Chen. How to prepare reproducible, homogeneous, and hydrolytically stable aminosilane-derived layers on silica. *Langmuir : the ACS journal of surfaces and colloids*, 28(1):416–423, 2012.

[109] Rabeb Layouni, Moinul Haque Choudhury, Paul E Laibinis, and Sharon M Weiss. Thermally carbonized porous silicon for robust label-free dna optical sensing. *ACS Applied Bio Materials*, 2019.

[110] Beniamino Sciacca, Sara D Alvarez, Francesco Geobaldo, and Michael J Sailor. Bioconjugate functionalization of thermally carbonized porous silicon using a radical coupling reaction. *Dalton Transactions*, 39(45):10847–10853, 2010.

[111] Yiliang Zhao, Girija Gaur, Raymond L. Mernaugh, Paul E. Laibinis, and Sharon M. Weiss. Comparative kinetic analysis of closed-ended and open-ended porous sensors. *Nanoscale Research Letters*, 11(1):395, 2016.

[112] WHO-Media-centre. Chikungunya fact sheet, 2020.

[113] Bryan C Mounce, Teresa Cesaro, Lea Vlajnić, Anna Vidiņa, Thomas Vallet, James Weger-Lucarelli, Gabriella Passoni, Kenneth A Stapleford, Jean-Pierre Levraud, and Marco Vignuzzi. Chikungunya virus overcomes polyamine depletion by mutation of nsp1 and the opal stop codon to confer enhanced replication and fitness. *Journal of virology*, 91(15), 2017.

[114] Olivier Schwartz and Matthew L Albert. Biology and pathogenesis of chikungunya virus. *Nature Reviews Microbiology*, 8(7):491–500, 2010.

[115] Monaíse MO Silva, Laura B Tauro, Mariana Kikuti, Rosângela O Anjos, Viviane C Santos, Thaiza SF Gonçalves, Igor AD Paploski, Patrícia SS Moreira, Leile CJ Nascimento, Gúbio S Campos, et al. Concomitant transmission of dengue, chikungunya, and zika viruses in brazil: clinical and epidemiological findings from surveillance for acute febrile illness. *Clinical Infectious Diseases*, 69(8):1353–1359, 2019.

[116] Wenxi An, Ningning Ge, Yilin Cao, Jin Sun, and Xia Jin. Recent progress on chikungunya virus research. *Virologica Sinica*, 32(6):441–453, 2017.

[117] Mathieu Dubrulle, Laurence Mousson, Sara Moutailler, Marie Vazeille, and Anna-Bella Failloux. Chikungunya virus and aedes mosquitoes: saliva is infectious as soon as two days after oral infection. *PloS one*, 4(6):e5895, 2009.

[118] MM Parida, SR Santhosh, PK Dash, and PV Lakshmana Rao. Rapid and real-time assays for detection and quantification of chikungunya virus. *Future Medicine*, pages 179–192, 2008.

[119] Ankitha George, MS Amrutha, Priyanshu Srivastava, Sujatha Sunil, VVR Sai, and Ramanathan Srinivasan. Development of a u-bent plastic optical fiber biosensor with plasmonic labels for the detection of chikungunya non-structural protein 3. *Analyst*, 146(1):244–252, 2021.

[120] Matthew B. Coppock, Margaret Hurley, Curtis Jones, Daniela Erickson, and Dimitra N. Stratis-Cullum. A novel discovery, maturation, and assay integration approach for the development of ruggedized multi-valent capture receptors exemplified against the chikungunya virus e2 protein. *Sensing and Bio-Sensing Research*, 22:100248, 2019.

[121] Christof Angermueller, Tanel Pärnamaa, Leopold Parts, and Oliver Stegle. Deep learning for computational biology. *Molecular Systems Biology*, 12(7):878, 2016.

[122] Carlo Barth and Christiane Becker. Machine learning classification for field distributions of photonic modes. *Communications Physics*, 1(1):58, 2018.

[123] Santiago Marco and Agustín Gutierrez-Galvez. Signal and data processing for machine olfaction and chemical sensing: A review. *IEEE Sensors Journal*, 12(11):3189–3214, 2012.

[124] Martina Sattlecker, Conrad Bessant, Jennifer Smith, and Nick Stone. Investigation of support vector machines and raman spectroscopy for lymph node diagnostics. *Analyst*, 135(5):895–901, 2010.

[125] Simone Ciampi, Till Böcking, Kristopher A Kilian, Michael James, Jason B Harper, and J Justin Gooding. Functionalization of acetylene-terminated monolayers on si (100) surfaces: a click chemistry approach. *Langmuir*, 23(18):9320–9329, 2007.

[126] L. Tay, N. L. Rowell, D. Poitras, J. W. Fraser, D. J. Lockwood, and R. Boukherroub. Bovine serum albumin adsorption on passivated porous silicon layers. *Canadian Journal of Chemistry*, 82(10):1545–1553, 2004.

[127] Mojun Zhu, Maria Z. Lerum, and Wei Chen. How to prepare reproducible, homogeneous, and hydrolytically stable aminosilane-derived layers on silica. *Langmuir*, 28(1):416–423, 2012.

[128] Zheng Li, Jon R. Askim, and Kenneth S. Suslick. The optoelectronic nose: Colorimetric and fluorometric sensor arrays. *Chemical Reviews*, 119(1):231–292, 2019.

[129] Hengwei Lin and Kenneth S. Suslick. A colorimetric sensor array for detection of triacetone triperoxide vapor. *Journal of the American Chemical Society*, 132(44):15519–15521, 2010.

[130] Mrinmoy De, Subinoy Rana, Handan Akpinar, Oscar R. Miranda, Rochelle R. Arvizo, Uwe H. F. Bunz, and Vincent M. Rotello. Sensing of proteins in human serum using conjugates of nanoparticles and green fluorescent protein. *Nature Chemistry*, 1:461, 2009.

[131] Markus Ringnér. What is principal component analysis? *Nature biotechnology*, 26(3):303–304, 2008.

[132] Avinash Navlani. Knn classification using scikit-learn, 2018.

[133] T. V. Bandos, L. Bruzzone, and G. Camps-Valls. Classification of hyperspectral images with regularized linear discriminant analysis. *IEEE Transactions on Geoscience and Remote Sensing*, 47(3):862–873, 2009.

[134] Richard Socher, Jeffrey Pennington, Eric H Huang, Andrew Y Ng, and Christopher D Manning. Semi-supervised recursive autoencoders for predicting sentiment distributions. In *Proceedings of the conference on empirical methods in natural language processing*, pages 151–161. Association for Computational Linguistics, 2011.

[135] Fabian Pedregosa, Gaël Varoquaux, Alexandre Gramfort, Vincent Michel, Bertrand Thirion, Olivier Grisel, Mathieu Blondel, Peter Prettenhofer, Ron Weiss, and Vincent Dubourg. Scikit-learn: Machine learning in python. *Journal of machine learning research*, 12(Oct):2825–2830, 2011.

[136] H. Sobral and M. Pena-Gomar. Determination of the refractive index of glucose-ethanol-water mixtures using spectroscopic refractometry near the critical angle. *Applied Optics*, 54(28):8453–8458, 2015.